Syntheses, Structures, and Applications of Inorganic Materials Functionalized by Fluorine

Hiroki Yamamoto

2021

Table of Contents

Chapter 1

General Introduction

1.1 Characters of fluorine and fluoride materials

The phrase ”Fluorine, a small atom with a big ego” was a theme of a symposium in Division of Fluorine Chemistry of American Chemical Society in 2000. As is described by this theme, fluorine has strong and distinct properties compared to other elements. The three representative characteristics of fluorine are small radius, low polarizability, and the highest electronegativity, and such uniqueness provides various attractive properties to fluorine-containing materials. Table 1-1 shows selected properties of fluorine together with hydrogen, oxygen, and other halogens. Its radius is the second largest next to hydrogen’s, and polarizability of anions and its electronegativity are the lowest and largest, respectively, among the elements in this table. It is interesting that the absolute value of the electron affinity of fluorine is smaller than that of chlorine whereas its electronegativity is the highest, which is explained by the strong repulsive forces between electrons due to its small size [1].

1.2 Production flow and application of fluorine-containing materials

The abundance of fluorine in the earth crust is 0.03 %, which is the 17th largest out of all elements and is as large as that of sulfur and nitrogen [2]. The natural resources containing fluorine are fluorite (CaF_2), fluoroapatite ($CaF_2 \cdot 3Ca_3(PO_4)_2$) contained in phosphate rock, and sodium cryolite (Na_3AlF_6). For the industrial production, fluorite is first reacted with sulfuric acid to obtain hydrogen fluoride (HF) and HF is used for producing various fluorine-containing compounds. Figure 1-1 shows the production flow and application of fluorine-containing materials. The chemical equation to form HF from fluorite is shown in the following:

$$CaF_2 + H_2SO_4 \rightarrow CaSO_4 + 2HF\uparrow \tag{1-1}$$

Hydrogen fluoride is a colorless and toxic gas at room temperature with a melting point of −83.36 °C and a boiling point of −19.51 °C. Due to its low vapor pressure around 1.2 atm at room temperature, it can be handled as a liquid and solvent for reactions. As liquidus HF has a high relative permittivity (83.6 at 0 °C), which is comparative to that of H_2O (87.9 at 0 °C), it is a good solvent to dissolve various solutes with wide handling temperatures.

Elemental fluorine (F_2) is also an important substance in inorganic, organic, and polymer fluorine chemistry. It is a light-yellow gas at room temperature with a melting point of −220 °C and a boiling point of −188 °C. Elemental fluorine has significantly high reactivities, which derives from the low dissociation energy of F_2. As is shown in Table 1-1, dissociation energy of diatomic molecule of halogen increases with decreasing the size of halogen atom ($I_2 < Br_2 < Cl_2$) due to larger overlapping of orbitals of two atoms to result in increasing the bond strength. However, that of F_2 is smaller than that of Cl_2 in spite of its smaller size, which deviates from the trend above, because of the repulsive forces among lone pairs. Elemental fluorine was first succeeded in isolation by Henri Moissan in 1886 by electrolysis of HF containing KF [3, 4]. Fluorine chemistry was developed rapidly after his brilliant achievements, and he won the Novel Prize for Chemistry in 1906. The current production method of F_2 mostly follows his method based on electrolysis of HF in KF–2HF molten salts at 90 °C, where the roles of KF are to improve the ionic conductivity and decrease vapor pressures of HF [5]. On the other hand, chemical synthesis of F_2 is also reported by the reaction between K_2MnF_6 and SbF_5 in 1986 [6], and the presence of F_2 in nature has been found in a radioactive fluorite containing uranium called antozonite [7].

As is shown in Figure 1-1, various fluorine-containing materials produced from HF have been utilized in the wide fields. For instance, fluoropolymers such as polytetrafluoroethylene (PTFE) and tetrafluoroethylene–perfluoroalkylvinylether copolymer (PFA) are used for coating of cookware and optical fiber cables, and containers with high thermal and chemical stabilities. In fluoroorganic chemistry, fluorine-containing medicines have long-lasting effects owing to strong C–F bonds and the small radius, and the improvement of relative lipophilicity by introducing fluorine to anesthetics realizes the prompt appearance and late disappearance of the effects [8, 9]. On the other hands, inorganic fluorides also play important roles in a variety of fields. Insulation in the power plant is conducted by SF_6, and UF_6 is utilized to enrich U^{235} against U^{238} for nuclear energy applications. Functionalized inorganic fluoride materials contribute to various material sciences such as electrochemical storage.

1.3 Carbon materials involved with fluorine

Out of various inorganic fluoride materials (e.g. FeF_3, $LiNiPO_4F$, and Li_3VF_6 for cathode materials for lithium-ion batteries, and $PbSnF_4$ and $Ba_{1-x}La_xF_{2+x}$ for fluoride-ion conductors [10-13]), carbon materials are extensively used and studied in view of wide applications due to many excellent advantages such as their low cost, high mechanical strength, high surface areas, high electrochemical and chemical stabilities. Carbon atoms make sp, sp^2, and sp^3 hybridized orbitals with four valence electrons, and the differences in bonding, crystallinity, and morphology bring the diversity of carbon materials such as amorphous carbon (e.g. carbon black, activated carbon, carbon fiber, hard carbon, and soft carbon), crystalline carbon (e.g. graphite, diamond), and nano carbon (e.g. fullerene, carbon nanotube, and graphene) [14-17]. Although fluorination of carbon materials is extensively investigated [18-24], the following sections describe the research backgrounds involving fluorinated carbon materials related to this thesis.

1.3.1 Fluorinated graphite

Poly(carbon monofluoride) ($(CF)_n$) is the most well-known fluorinated graphite and commercialized as a cathode material for lithium primary battery with a theoretical capacity of 865 mAh g^{-1} [25-27]. Lithium/graphite fluoride primary batteries have an operating voltage of 3.0 V and strong points in the performance at high temperature and reliability on the long-term use, and are used as power sources for utility meters and memory backup of computers. In addition to its use as a cathode material, it is also used as a solid lubricant which is not influenced by usage environments unlike graphite and MoS_2 [28]. Its hydrophobicity is also outstanding, and the contact angle of $(CF)_n$ against water is 143°, which is larger than 109° of that of PTFE [29, 30]. In addition to $(CF)_n$, poly(dicarbon monofluoride) ($(C_2F)_n$) and C_xF with C=C double bonds left in the carbon skeleton are also known as fluorinated graphite formed in different synthetic conditions (see Figure 1-2) [26, 31, 32].

While the C–F bonds in these fluorinated graphite materials are essentially covalent, another graphite compound with covalent bonds with other elements is graphite oxide. Graphite oxide has various oxygen-containing functional groups covalently bound to the graphite skeleton [33, 34]. Syntheses of fluorinated carbon materials by fluorinating graphite oxide have been also investigated with various fluorinating agents such as HF and IF_5 [35-43]. This synthetic route has advantages such as low-temperature reaction and no use of F_2, and is also applicable to synthesis of fluorinated graphene by fluorinating graphene oxide.

1.3.2 Fluorocomplex-anion graphite intercalation compounds

Although fluorinated graphites and graphite oxides have C–F and C–O covalent bonds, respectively, graphite intercalation compounds (GICs) accommodate ionic species by ionizing graphene layers [44-46]. In some definitions, fluorinated graphites and graphite oxides are classified to covalent GICs, but GICs mean the ionic GICs in this thesis. The GICs are formed by the intercalation of chemical species into graphite galleries by expanding graphene layers weakly bound to each other by the van der Waals force. The GICs have an interesting characteristic structure called the staging structure, where intercalates are periodically present between graphene layers; the staging structure with intercalates every *n* graphene layers is called stage-*n* (see Figure 1-3). Carbon atoms in GICs maintain the sp^2-hybridization whereas those in fluorinated graphite ($(CF)_n$ and $(C_2F)_n$) and graphite oxide are sp^3-hybridized. Various fluorocomplex anions such as BF_4^-, VF_6^-, and WF_6^- can be intercalated (GICs intercalated by MF_y^{z-} is denoted as MF_y-GICs in this thesis), and the formation enthalpies of fluorocomplex-anion-GICs largely depend on the F^- affinity of the parent fluoride [47]. A pF^- scale can be referred to as an indicator of F^- affinity of the parent fluoride as shown in Table 1-2 and below [48]:

$$pF^- = F^- \text{ affinity (kcal mol}^{-1}\text{) / 10} \qquad (1\text{-}2)$$

Here, F^- affinity is provided for a gaseous single molecule in vacuum and solvation and lattice energies are not considered, but they have to be taken into account for solid fluorides such as AlF_3. As shown in Table 1-2, SbF_5 and AsF_5 have quite high pF^- (large F^- affinity), and SbF_6- and AsF_6-GICs had attracted great attentions as light and high-conductive materials comparable to copper in 1970s deriving from their quite strong F^- affinity [49-52].

1.3.3 Fluorination of carbon materials for electrochemistry

Carbon materials play important roles in electrochemistry owing to their advantages such as low cost, high electrical conductivity, large surface area, and chemical robustness [53-

57]. Representative electrochemical applications of carbon materials are graphite as a negative electrode material in lithium-ion batteries, carbon black as a conductive material for electrodes, activated carbon as an electrode material for electric double layer capacitor.

Surface fluorination of graphite with F_2 or plasma CF_4 to form C–F bonds on the defects suppresses the decomposition of organic electrolytes and improves the initial coulombic efficiency. [58-62]. The electrochemical performance of activated carbon is also improved by surface fluorination for a cathode material of electric double layer capacitors. Here, change of surface morphology and increase in capacitance by fluorination are reported, and improvement of oxidation resistance is also expected due to the lowered HOMO energy level with introduction of the C–F bonds [19, 20, 63, 64]. On the other hand, introduction of too much amount of fluorine atoms sometimes causes decrease in electrical conductivity and increase in hydrophobicity to lower the performance of electrochemical devices made of carbon materials such as graphite, activated carbon, and carbon nanotube [65-67], and thus optimization of the fluorination degree and methods is important.

1.4 Fluorine-containing anions for ionic liquids

Ionic liquids (ILs) are liquids composed of only ionic species without neutral species near room temperature (< 100 °C, depending on definitions). Various kinds of cations and anions have been incorporated to form ILs: imidazolium, pyrrolidinium, pyridinium, piperidinium, tetraalkylammonium, trialkylsulfonium, and tetraalkylphosphonium for cations (Figure 1-4) and halide, bis(fluorosulfonyl)amide (FSA^-), (fluorosulfonyl)(trifluorosulfonyl)amide (FTA^-), bis(trifluoromethylsulfonyl)amide ($TFSA^-$), triflate (TfO^-), tetrafluoroborate (BF_4^-), hexafluorophosphate (PF_6^-), nitrate (NO_3^-), thiocyanate (SCN^-), dicyanamide ($N(CN)_2^-$), and tricyanomethanide ($C(CN)_3^-$)) for anions (Figure 1-5) [68-72]. Fluorine-containing anions are apparently major choices in ILs, which results from its strong electron withdrawing property or appropriate charge delocalization over the entire anion. Ionic liquids have a variety of unique properties such as negligible volatility and inflammability, high thermal and electrochemical stability, and high polarity and catalytic properties, providing them with possible applications as electrolytes of batteries, fuel cells, capacitors, electrodepositions, dye-sensitized solar cells, and reaction media for organic syntheses and extractions [73-82]. In general, salts have higher melting points than neutral molecules due to the high electrostatic interactions between cations and anions (e.g. melting point of 801 °C for NaCl). However, introduction of various ion designs such as bulkiness, asymmetry, and charge delocalization can achieve low melting points of ILs [83]. Using bulky ions lowers electron density on the surfaces of ions and weakens the electrostatic interactions. Asymmetry of ions hinders the high crystal packing and reduces the melting points. Charge delocalization prevents strong local electrostatic interactions.

Ionic liquid electrolytes are expected as promising candidates to overcome the safety concerns of lithium-ion batteries, replacing flammable and volatile organic electrolytes [84-86]. In addition to benefits in safety, IL electrolytes have high ionic conductivity and wide electrochemical windows, enabling their applications to high energy density secondary batteries using various shuttle ions [72, 76, 87-93]. High cycleability and rate capabilities are reported owing to formation of stable solid electrolyte interface (SEI) on the electrode which works as a passivation layer to enable facile ion diffusion and precludes the decomposition of the electrolytes [94-100].

1.5 Aims of this study

As is described above, fluorine is an alluring atom both scientifically and industrially and have important roles in a wide variety of fields. In this study, inorganic chemistry involved with fluorine is investigated such as discovery of new fluorine-containing materials, development of new fluorination methods, and structural characterization and electrochemical applications of fluorine-containing materials.

In Chapter 2, detailed information on equipment, materials, procedures and conditions in this thesis are provided. In Chapter 3, syntheses and structures of new fluorosilicate-graphite intercalation compounds (SiF_y-GICs) as new GICs are discussed, mainly targeting the intercalation of a doubly charged anion. In Chapter 4, deoxofluorination of graphite oxide with sulfur tetrafluoride (SF_4) is investigated as a new synthesis method of a fluorinated graphite material. Details on reactions as well as properties and structures of the resulting products are discussed. In Chapter 5, activated carbon is deoxofluorinated with SF_4 and the application of the resulting fluorinated activated carbon as an electrode material for electric double layer capacitor is explored. In Chapter 6, potassium single cation ionic liquid (K-SCIL) electrolyte as a new type of an electrolyte for potassium-ion batteries (PIBs) are developed. The Binary system of K-SCIL is investigated from two different fluorine-containing anion salts of K[FSA] and K[FTA]. Their physicochemical, thermal, and electrochemical properties and application for PIBs are discussed. In Chapter 7, K-SCIL electrolytes are extended to the ternary system of K[FSA], K[FTA], and K[TfO] to achieve a lower operating temperature than that for the binary system. Their physicochemical, thermal, and electrochemical properties and application for PIBs are investigated. Chapter 8 summarizes the entire thesis and describes prospects for future works.

Table 1-1 Properties of hydrogen, oxygen, and halogen atoms [1].

	H	O	F	Cl	Br	I
Atomic radius (pm)	53	74	64	99	114	135
Van der Walls radius (pm)	120	145	135	186	195	215
Polarizability of anion (10^{-24} cm^3)	137 (OH^-)	140	133	181	196	220
Electronegativity	2.1	3.5	4.0	3.0	2.8	2.5
Ionization energy (kJ mol^{-1})	1312	1313	1680	1255	1142	1007
Electron affinity (kJ mol^{-1})	−72.7	−141.0	−328.1	−348.5	−324.5	−295.1
Dissociation energy[a] (kJ mol^{-1})	436.0	498.4	158.8	242.6	192.8	151.1

[a] Dissociation energy of simple substances.

Table 1-2 A scale of pF$^-$ for various inorganic fluoride [48].

Compound	pF$^{-\,a}$	Compound	pF$^{-\,a}$
SbF_5	12.03	ClF_5	7.47
AlF_3	11.50	BrF_3	7.35
$AlFCl_2$	11.50	SiF_4	7.35
AlF_2Cl	11.47	SeF_4	7.12
$AlCl_3$	11.46	SOF_4	6.60
$TeOF_4$	10.79	$XeOF_4$	6.37
InF_3	10.75	TeF_6	6.15
GaF_3	10.70	POF_3	5.86
AsF_5	10.59	XeF_4	5.71
SnF_4	9.82	SF_4	5.67
Cis-IO_2F_3	9.66	COF_2	4.99
PF_5	9.49	PF_3	4.49
$SeOF_4$	8.69	HF	3.68
TeF_4	8.34	NO_2F	1.92
BF_3	8.31	NOF	1.74
GeF_4	8.30		

^{a}pF$^-$ is defined in Eq. (1-2).

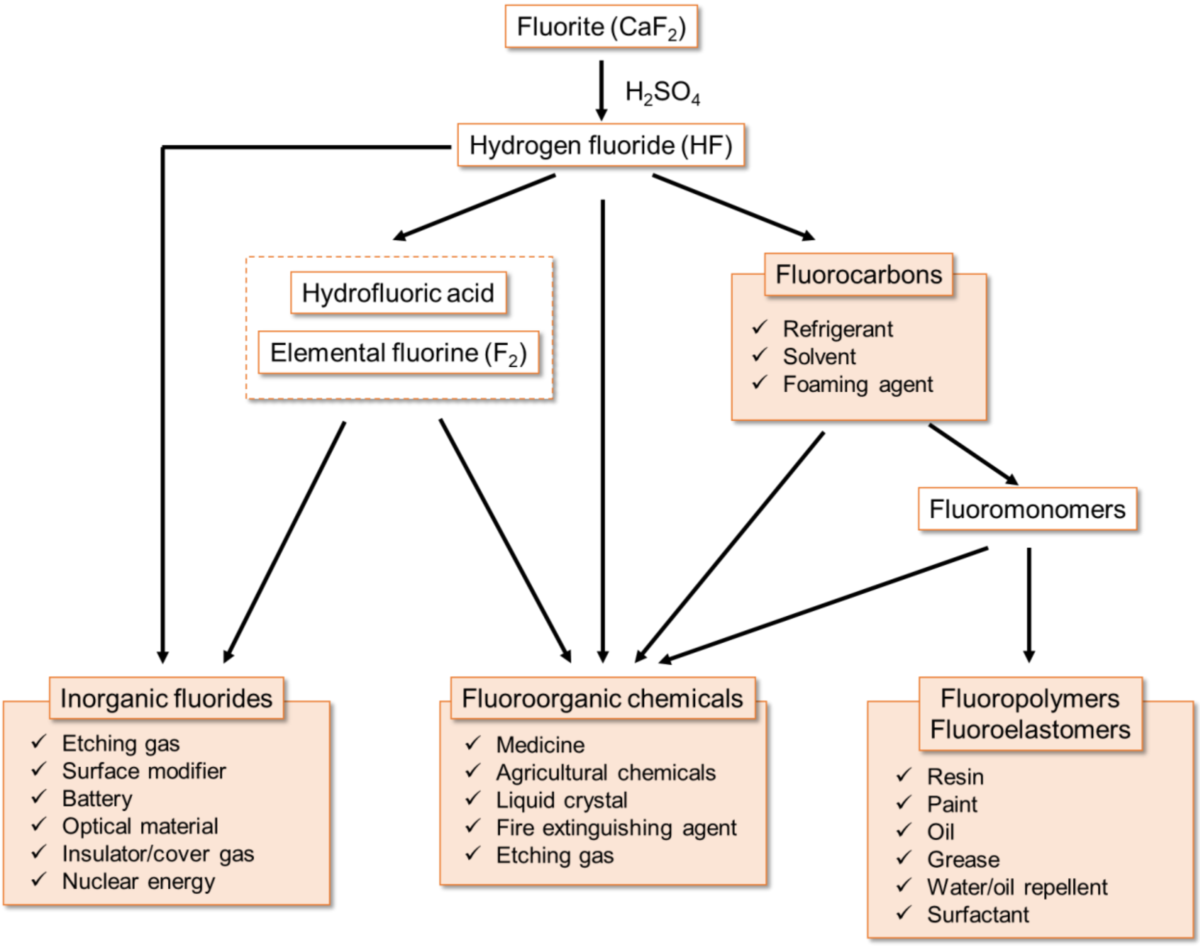

Figure 1-1 A schematic illustration of production flow and application of fluorine-containing materials [101].

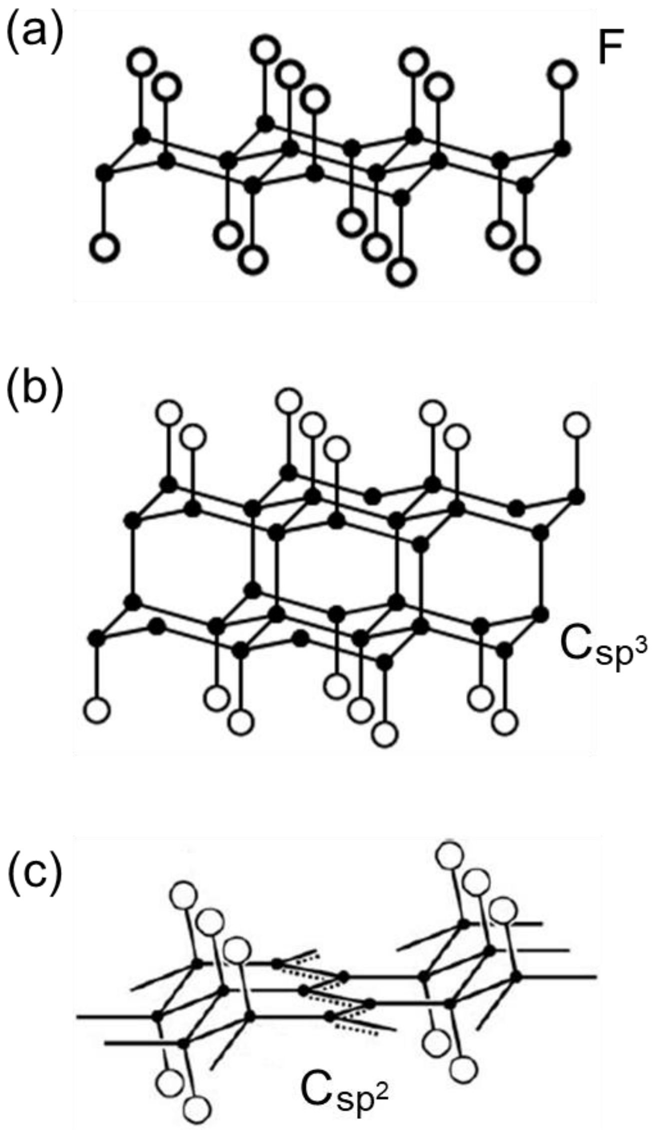

Figure 1-2 Schematic illustrations of structures of fluorinated graphite materials ((a) $(CF)_n$, (b) $(C_2F)_n$, and (c) C_xF) [26, 31, 32].

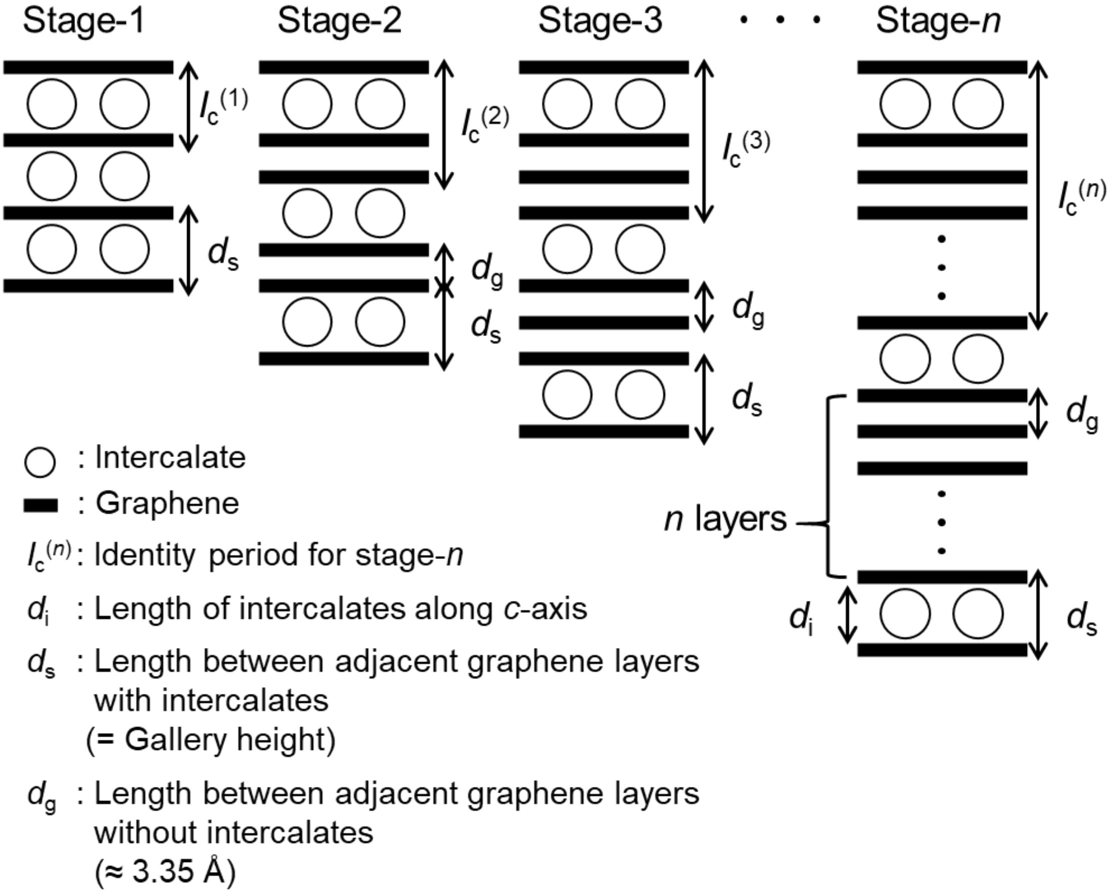

Figure 1-3 A schematic illustration of a staging model of GICs.

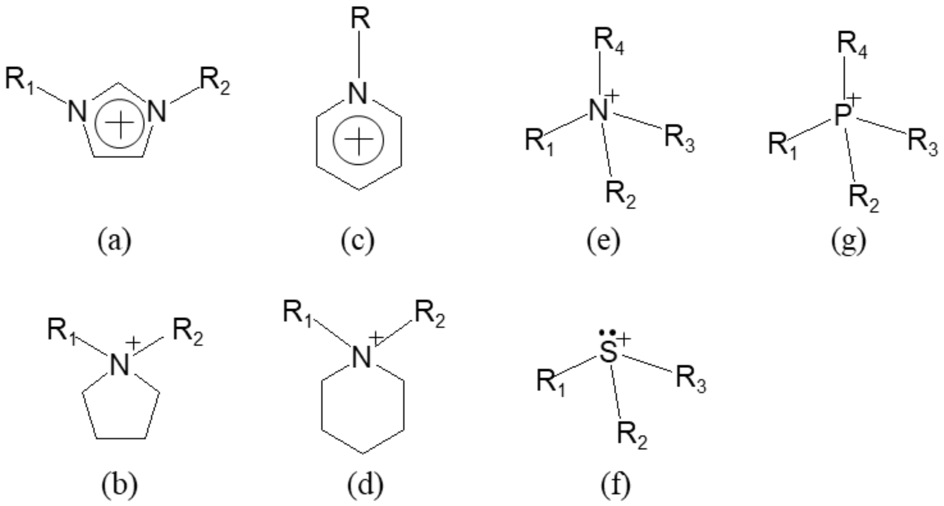

Figure 1-4 Structures of various cations for ILs; (a) dialkylimidazolium, (b) *N*,*N*-dialkylpyrrolidinium, (c) alkylpyridinium, (d) *N*,*N*-dialkylpipelidinium, (e) tetraalkylammonium, (f) trialkylsulfonium, and (g) tetraalkylphosphonium.

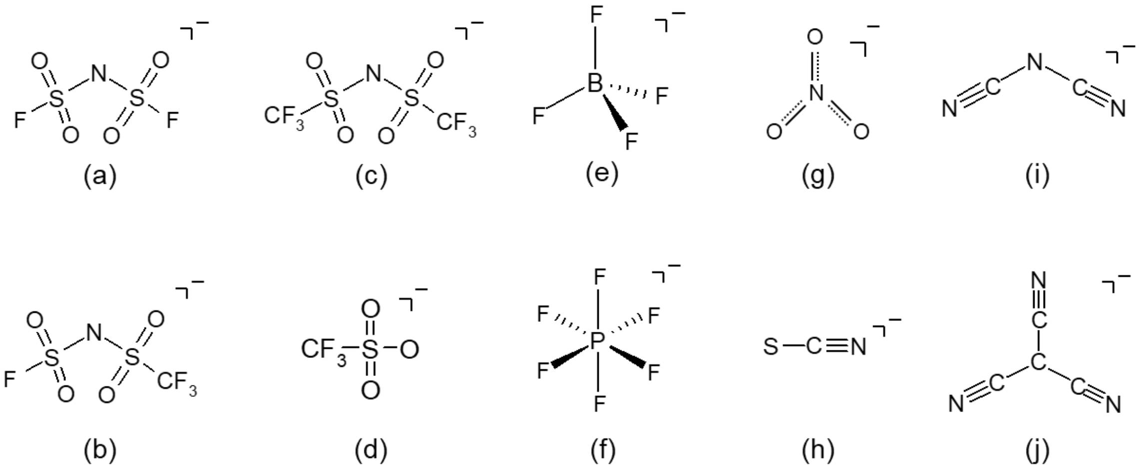

Figure 1-5 Structures of various anions for ILs; (a) bis(fluoromethylsulfonyl)amide (b) (fluoromethylsulfonyl)(trifluorosulfonyl)amide (c) bis(trifluoromethylsulfonyl)amide, (d) triflate, (e) tetrafluoroborate, (f) hexafluorophosphate, (g) nitrate, (h) thiocyanate, (h) dicyanamide, and (i) tricyanomethanide.

References

[1] M. Takashima, S. Yonezawa, R. Hagiwara, K. Matsumoto, Y. Kida, Y. Matsuo, *Introduction to Fluorine Chemistry 2010*, T. Nakajima (Ed.), Sankyo Shuppan, Tokyo, (2010) 1.

[2] F. W. Clarke, H. S. Washington, in *Report The Composition of the Earth's Crust*, (1924) 1.

[3] H. R. Moissan, *C. R. Hebd. Seances Acad. Sci.* , **75** (1886) 1543.

[4] M. R. Moissan, *C. R. Hebd. Seances Acad. Sci.*, **103** (1886) 202.

[5] G. H. Cady, *J. Am. Chem. Soc.*, **56** (1934) 1431.

[6] K. O. Christe, *Inorg. Chem.*, **25** (1986) 3721.

[7] J. Schmedt auf der Günne, M. Mangstl, F. Kraus, *Angew. Chem. Int. Ed.*, **51** (2012) 7847.

[8] D. H. R. Barton, R. H. Hesse, R. E. Markwell, M. M. Pechet, S. Rozen, *J. Am. Chem. Soc.*, **98** (1976) 3036.

[9] C. Gal, S. Rozen, *Tetrahedron Lett.*, **26** (1985) 2793.

[10] M. A. Reddy, M. Fichtner, *Advanced Fluoride-Based Materials for Energy Conversion*, T. Nakajima, H. Groult (Ed.), Elsevier, Amsterdam, (2015) 51.

[11] C. M. Julien, A. Mauger, H. Groult, *Advanced Fluoride-Based Materials for Energy Conversion*, T. Nakajima, H. Groult (Ed.), Elsevier, Amsterdam, (2015) 77.

[12] K. Mori, A. Mineshige, T. Saito, M. Sugiura, Y. Ishikawa, F. Fujisaki, K. Namba, T. Kamiyama, T. Otomo, T. Abe, T. Fukunaga, *ACS Appl.*, **3** (2020) 2873.

[13] H. Groult, A. Tressaud, *Chem. Commun.*, **54** (2018) 11375.

[14] M. Inagaki, F. Kang, *J. Mater. Chem. A*, **2** (2014) 13193.

[15] D. S. Su, S. Perathoner, G. Centi, *Chem. Rev.*, **113** (2013) 5782.

[16] J. Lee, J. Kim, T. Hyeon, *Adv. Mater.*, **18** (2006) 2073.

[17] F. Diederich, M. Gómez-López, *Chem. Soc. Rev.*, **28** (1999) 263.

[18] Y. Liu, L. Jiang, H. Wang, H. Wang, W. Jiao, G. Chen, P. Zhang, D. Hui, X. Jian, *Nanotechnol. Rev.*, **8** (2019) 573.

[19] E. Jeong, M.-J. Jung, Y.-S. Lee, *J. Fluorine Chem.*, **150** (2013) 98.

[20] M.-J. Jung, E. Jeong, S. Kim, S. I. Lee, J.-S. Yoo, Y.-S. Lee, *J. Fluorine Chem.*, **132** (2011) 1127.

[21] G. Nansé, E. Papirer, P. Fioux, F. Moguet, A. Tressaud, *Carbon*, **35** (1997) 175.

[22] H. Touhara, F. Okino, *Carbon*, **38** (2000) 241.

[23] W. Feng, P. Long, Y. Feng, Y. Li, *Adv. Sci.*, **3** (2016) 1500413.

[24] W. Zhang, L. Spinelle, M. Dubois, K. Guérin, H. Kharbache, F. Masin, A. P. Kharitonov, A. Hamwi, J. Brunet, C. Varenne, A. Pauly, P. Thomas, D. Himmel, J. L. Mansot, *J. Fluorine Chem.*, **131** (2010) 676.

[25] N. Watanabe, T. Nakajima, H. Touhara, *Graphite Fluorides*, Elsevier, Amsterdam (1988).

[26] Y. Sato, K. Itoh, R. Hagiwara, T. Fukunaga, Y. Ito, *Carbon*, **42** (2004) 2897.

[27] T. Nakajima, *TANSO*, **2004** (2004) 265.

[28] R. L. Fusaro, *Wear*, **53** (1979) 303.

[29] N. Watanabe, T. Nakajima, N. Ohsawa, *Bull. Chem. Soc. Jpn.*, **55** (1982) 2029.

[30] T. Nakajima, M. Touma, *J. Fluorine Chem.*, **57** (1992) 83.

[31] M. Murakami, K. Matsumoto, R. Hagiwara, Y. Matsuo, *Carbon*, **138** (2018) 179.

[32] Y. Sato, K. Itoh, R. Hagiwara, T. Fukunaga, Y. Ito, *Carbon*, **42** (2004) 3243.

[33] T. Szabó, O. Berkesi, I. Dékány, *Carbon*, **43** (2005) 3186.

[34] T. Szabó, O. Berkesi, P. Forgó, K. Josepovits, Y. Sanakis, D. Petridis, I. Dékány, *Chem. Mater.*, **18** (2006) 2740.

[35] O. Jankovský, P. Šimek, D. Sedmidubský, S. Matějková, Z. Janoušek, F. Šembera, M. Pumera, Z. Sofer, *RSC Adv.*, **4** (2014) 1378.

[36] T. Nakajima, Y. Matsuo, *Carbon*, **32** (1994) 469.

[37] T. Nakajima, A. Mabuchi, R. Hagiwara, *Carbon*, **26** (1988) 357.

[38] Z. Wang, J. Wang, Z. Li, P. Gong, X. Liu, L. Zhang, J. Ren, H. Wang, S. Yang, *Carbon*, **50** (2012) 5403.

[39] L. Pu, Y. Ma, W. Zhang, H. Hu, Y. Zhou, Q. Wang, C. Pei, *RSC Adv.*, **3** (2013) 3881.

[40] A. Hamwi, I. Al Saleh, *J. Power Sources*, **48** (1994) 311.

[41] X. Gao, X. Tang, *Carbon*, **76** (2014) 133.

[42] A. Hamwi, I. Al Saleh, D. Djurado, J. C. Cousseins, *Mater. Sci. Forum*, **91-93** (1992) 245.

[43] A. Wang, S. Bok, C. J. Mathai, R. Thiruvengadathan, C. M. Darr, H. Chen, M. R. Zachariah, K. Gangopadhyay, J. A. McFarland, M. R. Maschmann, S. Gangopadhyay, *Combust. Flame*, **215** (2020) 324.

[44] M. S. Dresselhaus, G. Dresselhaus, *Adv. Phys.*, **30** (1981) 139.

[45] Y. Li, Y. Lu, P. Adelhelm, M.-M. Titirici, Y.-S. Hu, *Chem. Soc. Rev.*, **48** (2019) 4655.

[46] E. Stumpp, *Physica B+C*, **105** (1981) 9.

[47] R. Hagiwara, N. Bartlett, *Fluorine-Carbon and Fluoride-Carbon Materials*, Marcel Dekker, Inc., New York (1995).

[48] K. O. Christe, D. A. Dixon, D. McLemore, W. W. Wilson, J. A. Sheehy, J. A. Boatz, *J. Fluorine Chem.*, **101** (2000) 151.

[49] G. M. T. Foley, C. Zeller, E. R. Falardeau, F. L. Vogel, *Solid State Commun.*, **24** (1977) 371.

[50] T. E. Thompson, E. R. Falardeau, L. R. Hanlon, *Carbon*, **15** (1977) 39.

[51] T. C. Wu, F. L. Vogel, L. A. Pendrys, C. Zeller, *Mater. Sci. Eng.*, **47** (1981) 161.

[52] G. Wortmann, F. Godler, B. Perscheid, G. Kaindl, R. Schlögl, *Synth. Met.*, **26** (1988) 109.

[53] G. Wang, L. Zhang, J. Zhang, *Chem. Soc. Rev.*, **41** (2012) 797.

[54] E. Frackowiak, F. Béguin, *Carbon*, **39** (2001) 937.

[55] R. L. McCreery, *Chem. Rev.*, **108** (2008) 2646.

[56] D. Chen, L. Tang, J. Li, *Chem. Soc. Rev.*, **39** (2010) 3157.

[57] M. F. L. De Volder, S. H. Tawfick, R. H. Baughman, A. J. Hart, *Science*, **339** (2013) 535.

[58] T. Achiha, T. Nakajima, Y. Ohzawa, *J. Electrochem. Soc.*, **154** (2007) A827.

[59] V. Gupta, T. Nakajima, Y. Ohzawa, H. Iwata, *J. Fluorine Chem.*, **112** (2001) 233.

[60] T. Nakajima, V. Gupta, Y. Ohzawa, M. Koh, R. N. Singh, A. Tressaud, E. Durand, *J. Power Sources*, **104** (2002) 108.

[61] T. Nakajima, V. Gupta, Y. Ohzawa, H. Iwata, A. Tressaud, E. Durand, *J. Fluorine Chem.*, **114** (2002) 209.

[62] T. Nakajima, J. Li, K. Naga, K. Yoneshima, T. Nakai, Y. Ohzawa, *J. Power Sources*, **133** (2004) 243.

[63] M.-H. Kim, J.-H. Yang, Y.-M. Kang, S.-M. Park, J. T. Han, K.-B. Kim, K. C. Roh, *Colloids Surf. A Physicochem. Eng. Asp.*, **443** (2014) 535.

[64] E. Jeong, M.-J. Jung, S. H. Cho, S. I. Lee, Y.-S. Lee, *Colloids Surf. A Physicochem. Eng. Asp.*, **377** (2011) 243.

[65] T. Nakajima, M. Kawaguchi, N. Watanabe, *Solid State Ion.*, **11** (1983) 65.

[66] E. Jeong, M.-J. Jung, S. G. Lee, H. G. Kim, Y.-S. Lee, *J. Ind. Eng. Chem.*, **43** (2016) 78.

[67] M.-J. Jung, E. Jeong, S. Cho, S. Y. Yeo, Y.-S. Lee, *J. Colloid Interface Sci.*, **381** (2012) 152.

[68] Z.-B. Zhou, H. Matsumoto, K. Tatsumi, *Chem. Eur. J.*, **10** (2004) 6581.

[69] S. A. Forsyth, S. R. Batten, Q. Dai, D. R. MacFarlane, *Aust. J. Chem.*, **57** (2004) 121.

[70] H.-B. Han, J. Nie, K. Liu, W.-K. Li, W.-F. Feng, M. Armand, H. Matsumoto, Z.-B. Zhou, *Electrochim. Acta*, **55** (2010) 1221.

[71] D. R. MacFarlane, J. Golding, S. Forsyth, M. Forsyth, G. B. Deacon, *Chem. Commun.*(2001) 1430.

[72] Q. Zhou, W. A. Henderson, G. B. Appetecchi, M. Montanino, S. Passerini, *J. Phys. Chem. B*, **112** (2008) 13577.

[73] K. Matsumoto, J. Hwang, S. Kaushik, C.-Y. Chen, R. Hagiwara, *Energy Environ. Sci.*, **12** (2019) 3247.

[74] J. S. Wilkes, *Green Chem.*, **4** (2002) 73.

[75] R. Hagiwara, Y. Ito, *J. Fluorine Chem.*, **105** (2000) 221.

[76] M. Armand, F. Endres, D. R. MacFarlane, H. Ohno, B. Scrosati, *Nat. Mater.*, **8** (2009) 621.

[77] V. Etacheri, R. Marom, R. Elazari, G. Salitra, D. Aurbach, *Energy Environ. Sci.*, **4** (2011) 3243.

[78] K. Xu, *Chem. Rev.*, **104** (2004) 4303.

[79] R. D. Rogers, K. R. Seddon, *Science,* **302** (2003) 792.

[80] R. Hagiwara, T. Nohira, K. Matsumoto, Y. Tamba, *Electrochem. Solid-State Lett.*, **8** (2005) A231.

[81] M. P. S. Mousavi, B. E. Wilson, S. Kashefolgheta, E. L. Anderson, S. He, P. Bühlmann, A. Stein, *ACS Appl. Mater. Inter.*, **8** (2016) 3396.

[82] I. Takeuchi, K. Asaka, K. Kiyohara, T. Sugino, N. Terasawa, K. Mukai, S. Shiraishi, *Carbon*, **47** (2009) 1373.

[83] H. Xue, R. Verma, J. n. M. Shreeve, *J. Fluorine Chem.*, **127** (2006) 159.

[84] S. Wilken, P. Johansson, P. Jacobsson, *Solid State Ion.*, **225** (2012) 608.

[85] A. Guéguen, D. Streich, M. He, M. Mendez, F. F. Chesneau, P. Novák, E. J. Berg, *J. Electrochem. Soc.*, **163** (2016) A1095.

[86] S. Wilken, M. Treskow, J. Scheers, P. Johansson, P. Jacobsson, *RSC Adv.*, **3** (2013) 16359.

[87] C. Ding, T. Nohira, A. Fukunaga, R. Hagiwara, *Electrochemistry*, **83** (2015) 91.

[88] K. Yoshii, T. Masese, M. Kato, K. Kubota, H. Senoh, M. Shikano, *ChemElectroChem*, **6**

(2019) 3901.

[89] T. Masese, K. Yoshii, Y. Yamaguchi, T. Okumura, Z.-D. Huang, M. Kato, K. Kubota, J. Furutani, Y. Orikasa, H. Senoh, H. Sakaebe, M. Shikano, *Nat. Commun.*, **9** (2018) 3823.

[90] T. Yamamoto, K. Matsumoto, R. Hagiwara, T. Nohira, *J. Phys. Chem. C*, **121** (2017) 18450.

[91] K. Matsumoto, Y. Okamoto, T. Nohira, R. Hagiwara, *J. Phys. Chem. C*, **119** (2015) 7648.

[92] C. Ding, T. Nohira, R. Hagiwara, K. Matsumoto, Y. Okamoto, A. Fukunaga, S. Sakai, K. Nitta, S. Inazawa, *J. Power Sources*, **269** (2014) 124.

[93] K. Matsumoto, T. Hosokawa, T. Nohira, R. Hagiwara, A. Fukunaga, K. Numata, E. Itani, S. Sakai, K. Nitta, S. Inazawa, *J. Power Sources*, **265** (2014) 36.

[94] M. B. Pinson, M. Z. Bazant, *J. Electrochem. Soc.*, **160** (2012) A243.

[95] M. Wang, L. Huai, G. Hu, S. Yang, F. Ren, S. Wang, Z. Zhang, Z. Chen, Z. Peng, C. Shen, D. Wang, *J. Phys. Chem. C*, **122** (2018) 9825.

[96] M.-T. F. Rodrigues, F. N. Sayed, H. Gullapalli, P. M. Ajayan, *J. Power Sources*, **381** (2018) 107.

[97] M. Haruta, T. Okubo, Y. Masuo, S. Yoshida, A. Tomita, T. Takenaka, T. Doi, M. Inaba, *Electrochim. Acta*, **224** (2017) 186.

[98] T. Jaumann, J. Balach, M. Klose, S. Oswald, U. Langklotz, A. Michaelis, J. Eckert, L. Giebeler, *Phys. Chem. Chem. Phys.*, **17** (2015) 24956.

[99] G. G. Eshetu, T. Diemant, M. Hekmatfar, S. Grugeon, R. J. Behm, S. Laruelle, M. Armand, S. Passerini, *Nano Energy*, **55** (2019) 327.

[100] G. G. Eshetu, S. Grugeon, H. Kim, S. Jeong, L. Wu, G. Gachot, S. Laruelle, M. Armand, S. Passerini, *ChemSusChem*, **9** (2016) 462.

[101] M. Yamabe, *Tokoton Yasashii Fusso no Hon*, Nikkan Kogyo Shinbun, Tokyo (2012).

Chapter 2

Experimental

2.1 Apparatus and material handling

2.1.1 Glove box and open dry chamber

Materials sensitive to the air and moisture were handled in Ar-filled glove boxes (Glove boxes: Miwa Manufacturing Co., Ltd., DBO-1KH-HNBR3, or Unico Ltd., UL-1800AA-KIZ, Ar: Kyoto Teisan K. K., purity > 99.998 %) equipped with a gas purification system. The dew point was typically maintained below –80 °C by monitoring it with a dew point meter and the oxygen concentration was monitored to keep below 1 ppm with an oxygen analyzer (GE Sensing & Inspection Technologies Co., Ltd., DF-150ε). Handling of moisture sensitive materials were also carried out in an open dry chamber filled with dried air (Daikin Industries, Ltd., HRG-50AR or HRW-60AR). The dew point was monitored to be below −60 °C.

2.1.2 Reaction manifold

Figure 2-1 shows a schematic illustration of a corrosion-resistant reaction manifold made of stainless steel (316) for handling corrosive materials and drying materials. It consisted of stainless-steel pipes (316, 1/2 inch o.d.) connected to stainless steel unions (Swagelok Co., 316, 1/2 inch o.d. and 1/4 inch o.d.) and valves (Swagelok Co., 316) with Kel-F (polychlorotrifluoroethylene) tips. A tetrafluoroethylene-perfluoroalkylvinylether copolymer (PFA) tube (1/4 inch o.d.) was used for connecting parts to reactors and gas cylinders. The manifold was connected to rotary vacuum pumps (Ulvac, Inc., GLD-137CC) through a chemical trap and a cold trap. The chemical trap was a stainless cylinder filled with soda lime to detoxify corrosive gases for preventing them going into the pumps. The cold trap was made of Pyrex glass and cooled by liquid nitrogen to trap volatile substances including water vapor. Pumping only through the cold trap provided high vacuum below 1 Pa. Pressures in the manifold was monitored with a Bourdon gauge (Nagano Keiki Co., Ltd.) for high pressure regions (above 1 kPa) and a Pirani gauge (Ulvac, GP-1G) for low pressure regions (below 100 kPa).

Caution: Gaseous and liquidus fluoride substances such as HF, SF_4, SiF_4, and PF_5 are hazardous, and must be carefully handled using appropriate protective gear with immediate access to appropriate treatment procedures in the event of accident or their contact with skin [1].

2.1.3 Reactors and drying vessels

Figures 2-2, 2-3, and 2-4 show schematic illustrations of a PFA reactor, a nickel reactor, and a drying vessel. The bottom of PFA tube (1 inch o.d.) was heat-sealed and the top was attached to the stainless-steel valve. The nickel reactor was used for reactions requiring high temperatures (≥ 100 °C) or high pressures (> 2 atm). A sample was placed in a nickel boat and in the nickel reactor. The drying vessel was made of Pyrex glass and sealed using a Viton o-ring, a clamp, and a stainless-steel cover. A sample was loaded in a beaker made of Pyrex glass in the drying vessel.

2.2 Structural characterizations

2.2.1 X-ray diffraction (XRD)

Structures of the samples were characterized by an XRD diffractometer in a Bragg-Brentano geometry (Smartlab, Rigaku Corp., Cu$K\alpha$ radiation; $\lambda = 1.5418$ Å, 40 kV–30 mA). It was equipped with a D-tex Ultra 250 Si-strip high speed detector. The XRD patterns were obtained in a scan rate of 1° min^{-1}. Air-sensitive materials were loaded in an airtight cell with beryllium windows (Rigaku Corp.) under a dry Ar atmosphere.

2.2.2 X-ray photoelectron spectroscopy (XPS)

Chemical states of elements on the surface were analyzed by an XPS spectrometer (JPS-9010 MC spectrometer, JEOL, Ltd., Mg*K*α radiation). Samples were placed on an indium foil and an airtight cell was used to prevent their exposures to air.

2.2.3 X-ray fluorescence spectroscopy (XRF)

Elemental compositions were investigated by an energy dispersive XRF analyzer (EDXL3000, Rigaku Corp.) under a He flow atmosphere. Samples were placed in a sample holder made of polyethylene, and prolene film (Chemplex, thickness: 4.0 μm) was used as a window to seal the sample holder to prevent the exposure of a sample to air.

2.2.4 Infrared spectroscopy (IR)

Functional groups were analyzed by an FT-IR spectrometer (ALPHA I or ALPHA II, Bruker Optics Laboratories, Inc.) at a resolution of 4 cm^{-1}. Gas samples were measured in the transmission mode using a gas cell with AgCl windows. Solid samples were measured by the single reflection attenuated total reflection (ATR) method on the diamond prism in the open dry chamber.

2.2.5 Transmission electron microscopy – energy dispersive X-ray spectroscopy – electron energy loss spectroscopy (TEM–EDS–EELS)

Structures, elemental compositions, and morphologies of selected samples were characterized by a field emission transmission electron microscope (JEM-2100F microscope, JEOL, Ltd.) operated at an accelerating voltage of 60 kV.

2.2.6 Elemental analysis

Chemical compositions of organic elements (C, H, N, F, and S) were analyzed at Organic Microanalysis Laboratory, Kyoto University. The elements of C, H, and N were analyzed with organic elemental analyzers (JM-10 or JM-11, J-Science Lab Co. Ltd., or MT-5 or MT-6, Yanaco Technical Science Co., Ltd.), and those of F and S were analyzed by the ion chromatography (XS-2100H, Nittoseiko Analytech Co., Ltd.).

2.3 Thermal and physicochemical characterizations

2.3.1 Thermogravimetry–differential thermal analysis (TG–DTA)

Thermal behaviors of the samples were investigated by a thermogravimetric differential thermal analyzer (ThermoPlusEvo2 TG8120) at a scan rate of 5 °C min^{-1} in air. An Al pan was used as a sample holder.

2.3.2 Differential scanning calorimetry (DSC)

Thermal transition temperatures were measured with a differential scanning calorimeter (DSC220 for Chapter 6 or DSC7000 for Chapter 7, Hitachi High-Tech Corporation) under a N_2 gas flow atmosphere at a scan rate of 10 °C min^{-1} or 2 °C min^{-1}. A sample was sealed in an Al pan in the open dry chamber to prevent its exposure to air.

2.3.3 Viscosity measurement

Viscosity was measured using an electro-magnetically spinning viscometer (EMS-100, Kyoto Electronics Manufacturing Co., Ltd.). A sample was sealed in glass tubes with a spherical Al probe (2 mm in diameter) in the dry chamber. Bubbles in the test tube were carefully removed prior to measurements. The glass tube was kept for 30 minutes before measurements at each temperature (between 50 °C and 150 °C), and measurements were conducted 10 times at each temperature and the average was regarded to be the true value.

2.3.4 Ionic conductivity measurement

Ionic conductivities were measured by AC impedance spectroscopy with an AC perturbation of 10 mV using an electrochemical analyzer (HZ-Pro, Hokuto Denko Corporation). A sample was sealed in a cell with two Pt black electrodes (Radiometer Analytical SAS). The ionic conductivity was calculated by the following equation Eq. (2-1);

$$\sigma = K / R \tag{2-1}$$

Here, σ is the specific ionic conductivity, K is the cell constant, and R is the measured resistance. The cell constant K was calculated to be 2.37 $\mathrm{cm^{-1}}$ using $\sigma = 1.408\ \mathrm{mS \cdot cm^{-1}}$ and $R = 1680\ \Omega$, which is obtained by measuring the resistance of a KCl saturated standard solution with the cell.

2.3.5 Density measurement

Density was obtained either by using a 5-mL or 1-mL of volumetric cylinder. For the 5-mL cylinder, it was obtained by measuring the volume of a certain weight of a sample. For the 1-mL cylinder, it was obtained by measuring a weight of a sample to give the volume of 1 mL at each temperature.

2.4 Electrochemical measurements

2.4.1 Electrode preparation

Two different graphite negative electrodes were prepared in Chapters 6 and 7. In

Chapter 6, natural graphite powder (SNO-10, SEC Carbon Ltd., mean diameter of 10 μm) as an active material, polyvinylidene fluoride (PVDF, Kureha Corporation) as a binder, and Cu foil as a current collector were used (graphite : PVDF = 80 : 20 in wt%). The PVDF, which is dissolved in *N*-methyl-2-pyrrolidone (NMP) with 12 wt%, and the natural graphite powder were mixed in a plastic container and another portion of NMP (Fujifilm Wako Pure Chemical Industries Corporation, purity 99%) was added to it to adjust the ratio of solid components (graphite and PVDF) to be 25 wt% against all components (graphite + PVDF + NMP). They were mixed by a planetary centrifugal mixer (AR-100, Thinky) to make a slurry. The resulting slurry was cast on Cu foil and dried under vacuum at 60 °C overnight. The resulting electrode sheet was punched into disks with 10 mm diameter (area of 0.785 cm^2). The disks were dried at 100 °C under vacuum for 1 day.

In Chapter 7, natural graphite powder (SNO-10, SEC Carbon Ltd., mean diameter of 10 μm) as an active material, acetylene black (AB, Fujifilm Wako Pure Chemical Industries Corporation) as a conductive material, carboxymethyl cellulose (CMC) as a dispersant, styrene butadiene rubber (SBR) as a binder, and Al foil as a current collector were used (graphite : AB: CMC: SBR = 80 : 10 : 5 : 5 in wt%). The natural graphite powder, 2 wt% of CMC solution, and 40 wt% SBR solution were mixed in a container, and further mixed by the planetary centrifugal mixer to make a slurry. The slurry was cast on Al foil and dried under vacuum at 60 °C overnight. The resulting sheet was punched into disks with 10 mm diameter (area of 0.785 cm^2). The disk electrode thus obtained was dried at 80 °C under vacuum for 1 day.

2.4.2 Cell configuration

In Chapter 5, a beaker-type cell in a three-electrode configuration was used as is shown in Figure 2-5. An activated carbon sheet (ACS, thickness: 0.2 mm, 85 wt % of activated carbon from phenol resin with a surface area of 2050 $\mathrm{m}^2\cdot\mathrm{g}^{-1}$, mean pore diameter of 2.14 nm, and total pore volume, 1.10 cm^3 g^{-1}) was punched into disks (6 mm in diameter as working electrodes (W.E.) and 8 or 16 mm in diameter as counter electrodes (C.E.)). The disks with a diameter of 6 mm were used for the reactions with SF_4. The ACS was pressed on Al mesh (The Nilaco Corporation, 0.11 mm in thickness, mesh openings of 149 μm) as is shown in Figure 2-6, and Al wire (The Nilaco Corporation, 0.50 mm in diamter, purity > 99.999%) was fixed with the Al mesh. The wire was fixed in a hole of a socket electrode (EC Frontier Co. Ltd.) as is shown in Figure 2-6. Potential of the electrochemical measurements was referenced to a reference electrode (R.E.) of the Ag^+/Ag redox couple. Silver trifluoromethanesulfonate (Ag[TfO], FUJIFILM Wako Pure Chemical Corporation, purity > 97 %) was dissolved in an electrolyte (1 M [TEA][BF_4]/PC, [TEA][BF_4]: tetraethylammonium tetrafluoroborate, PC: propylene carbonate, Kishida Chemical Co., Ltd., CPG-00005, water content < 10 ppm)) to give the concentration of 0.01 M. The electrolyte was poured into a glass compartment with a Vycor porous glass (RE-6, EC Flontier CO., Ltd.) junction and kept for about 1 day to immerse the electrolyte sufficiently into the Vycor porous glass.

In Chapter 6, a flat-type cell (Hohsen Corp., HS-2) in a two-electrode configuration with the potassium metal counter electrode was used as shown in Figure 2-7. A glass filter (Nippon Sheet Glass, TGP010, thickness of 100 μm) was used as a separator, and was impregnated with the electrolytes. The cell was assembled in the glove box. In Chapter 7, the same flat-type cell as in Chapter 6 was used for electrochemical measurements using the graphite working electrodes. For electrochemical measurements using an Al or Pt plate electrode, 2032-type coin cells with a K metal disk (Sigma-Aldrich, purity 98%) counter electrode were used. Figure 2-8 shows the schematic illustration of the coin cell. Aluminum or Pt foil (16 mm in diameter) was set at the bottom as a working electrode, and Kapton film (16 mm in diameter and 25 μm in thickness) with a hole (10 mm in diameter) at the center was fixed on the foils to adjust the areas of the working electrodes (0.785 cm^2). Glass fiber filter

(Whatman, GF-A, 260 mm in thickness and 22 mm in diameter) was used as a separator after drying under vacuum at 100 °C for 1 day. Its large size was for preventing liquidus potassium metal from reaching the working electrode for short circuit. The electrolyte of $K[FSA]_{0.33}[FTA]_{0.33}[TfO]_{0.33}$ was impregnated into the separator at 80 °C under vacuum overnight. The large separator in size was necessary to prevent short circuit by molten K metal at high temperatures. A K metal disk (Aldrich, purity 98 %) was used as a counter electrode.

2.4.3 Potential sweep electrochemical measurements

Cyclic voltammetry was performed by a potentiostat (VSP, Bio-Logic Sciences Instruments Ltd.) using the beaker-type cell in Chapters 5. In Chapter 6, it was conducted by another potentiostat (SP-50, Bio-Logic Sciences Instruments Ltd.) using the flat-type cell. In Chapter 7, cyclic voltammetry was performed using Pt or Al foil in the coin cell by the VSP potentiostat and using the graphite electrode in the flat-type cell by the SP-50 potentiostat.

2.4.4 Galvanostatic electrochemical measurements

In Chapter 5, galvanostatic charge-discharge tests were performed by a galvanostat (VSP, Bio-Logic Sciences Instruments Ltd.) using the beaker-type cell. In Chapter 6, galvanostatic charge-discharge tests were performed by a charge-discharge device (HJ-1001SD8C, Hokuto Denko Corporation) using the flat-type cell. In Chapter 7, galvanostatic charge-discharge tests using an Al foil working electrode were performed by the VSP galvanostat using the coin cell and those using the graphite electrode were conducted by the charge-discharge device using the flat-type cell.

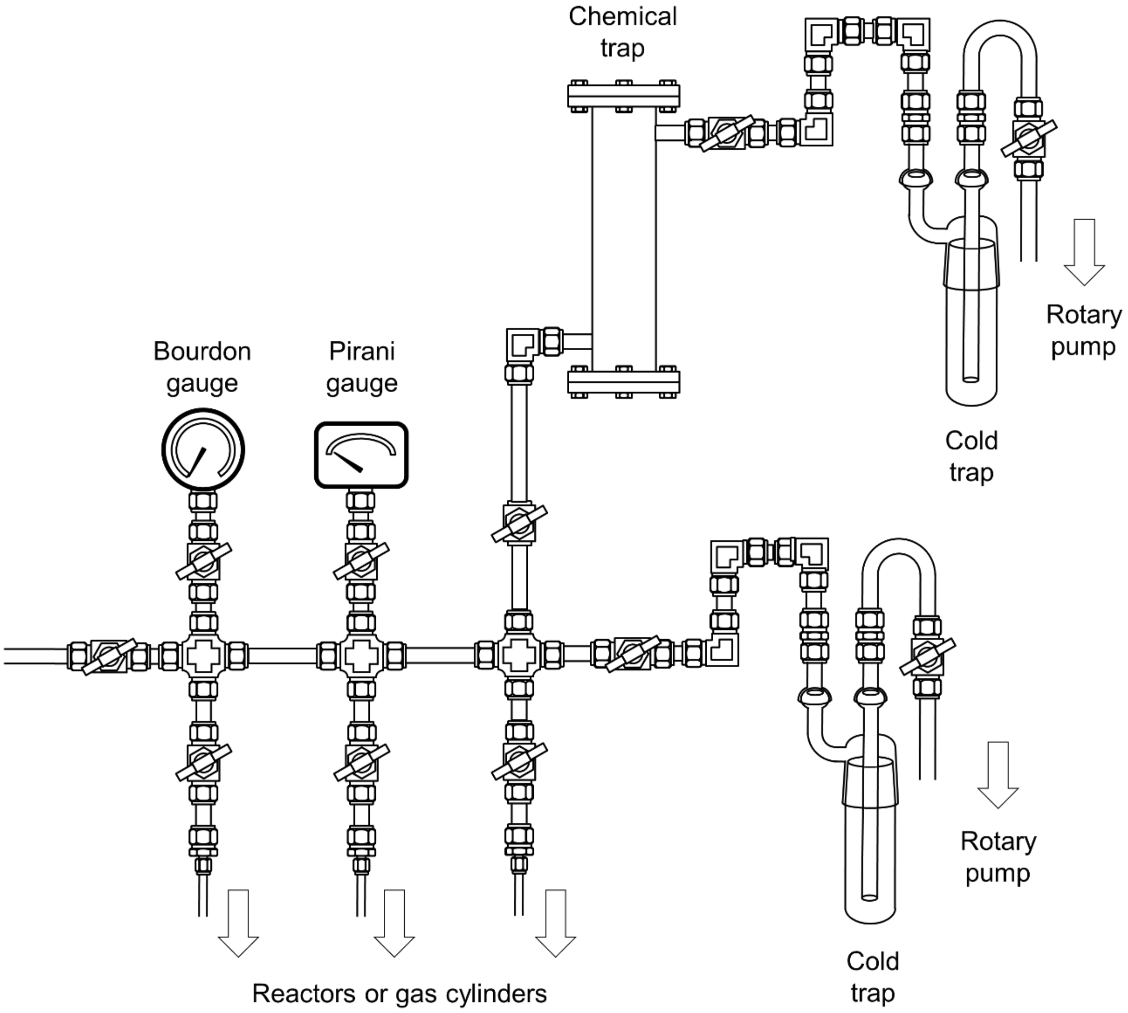

Figure 2-1 A schematic illustration of the reaction manifold [2].

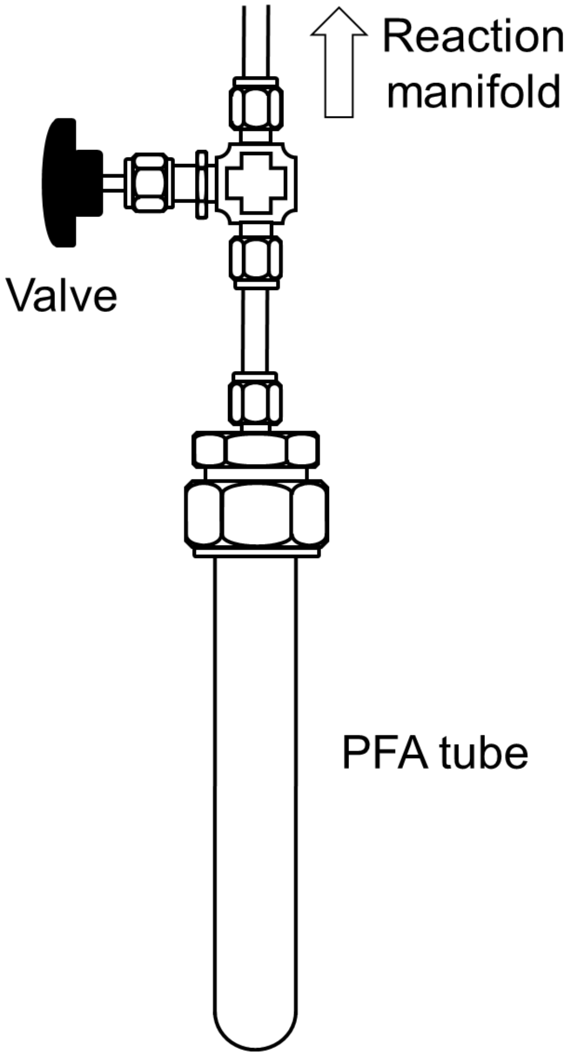

Figure 2-2 A schematic illustration of the PFA reactor [2].

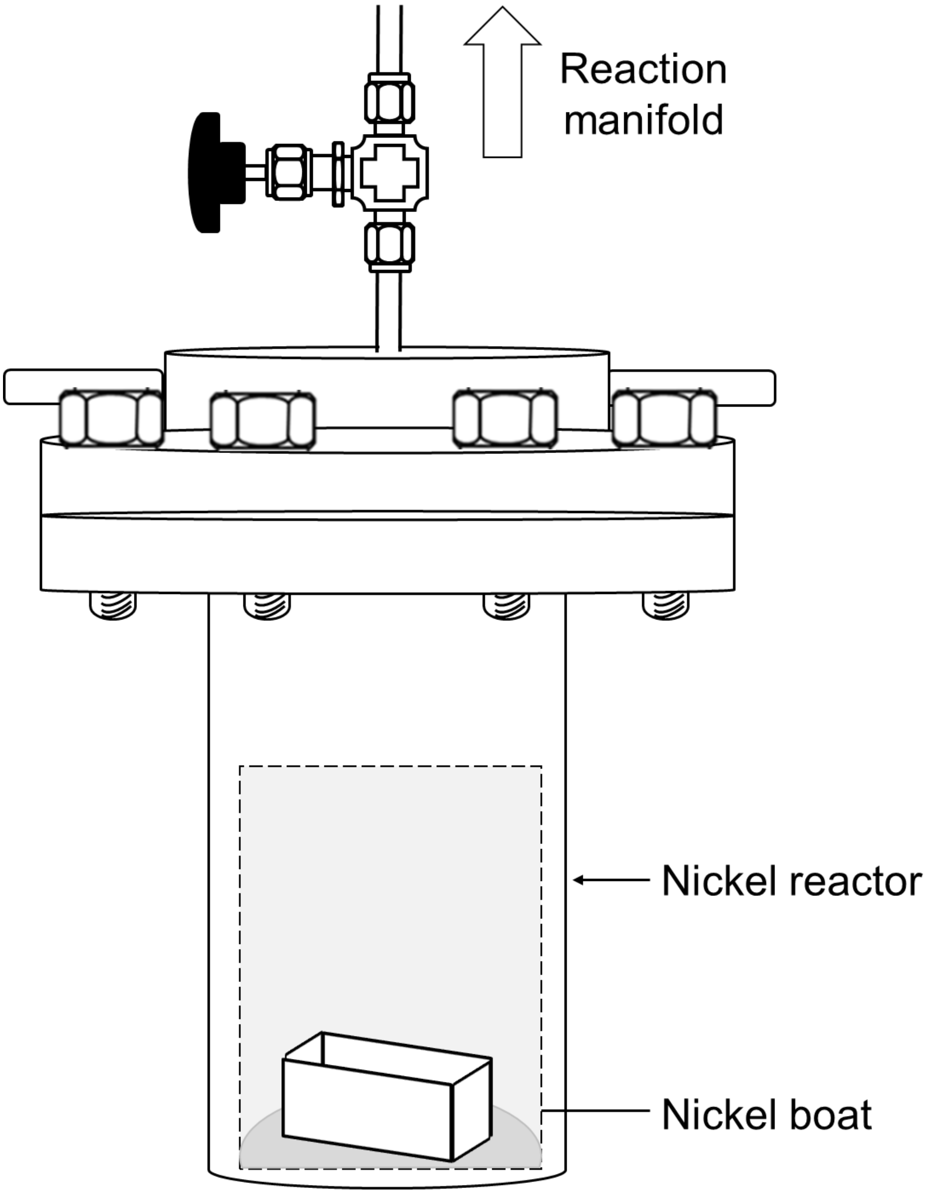

Figure 2-3 A schematic illustration of the nickel reactor with a nickel boat inside.

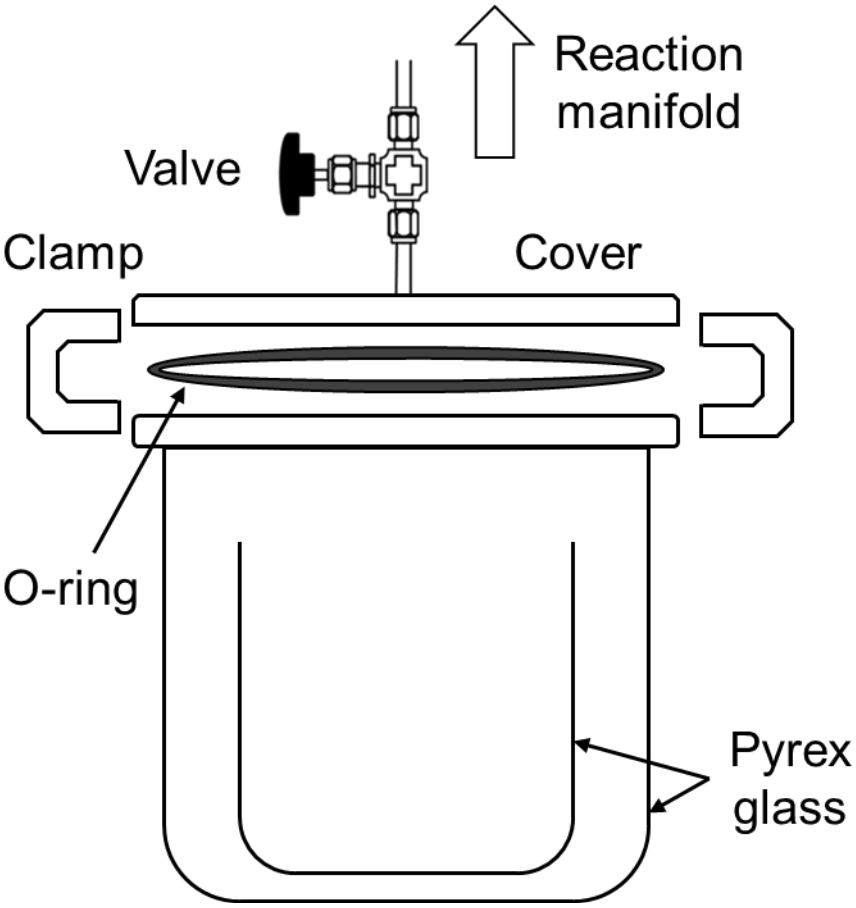

Figure 2-4 A schematic illustration of a drying vessel.

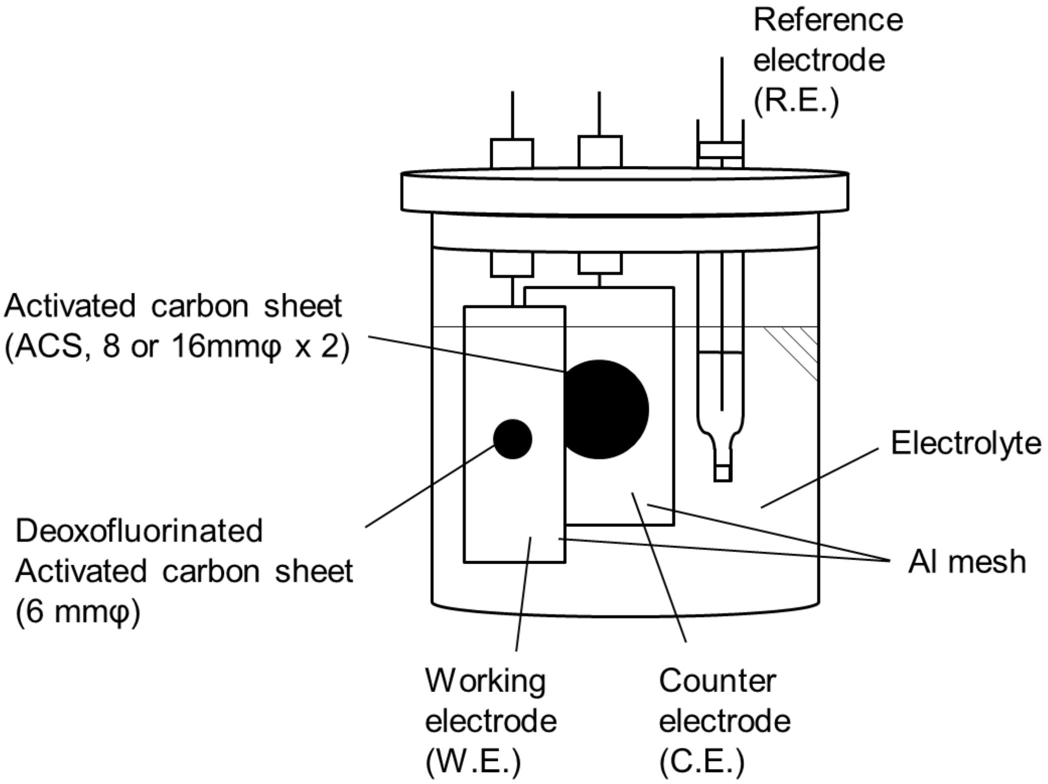

Figure 2-5 A schematic illustration of a beaker cell in a three-electrode configuration.

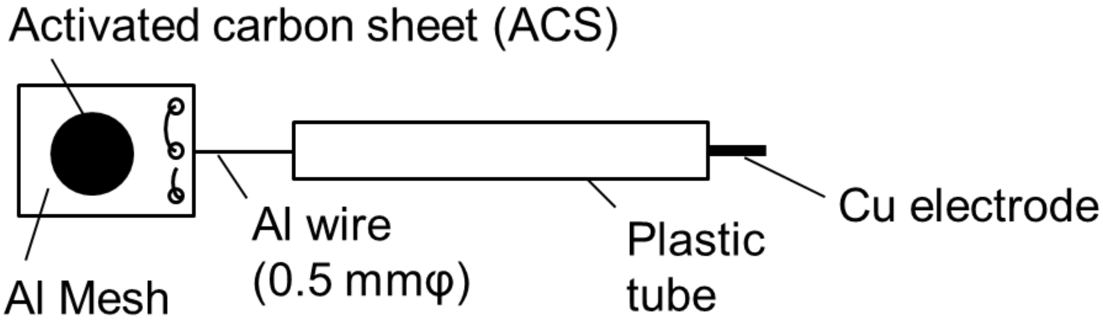

Figure 2-6 A schematic illustration of working and counter electrodes.

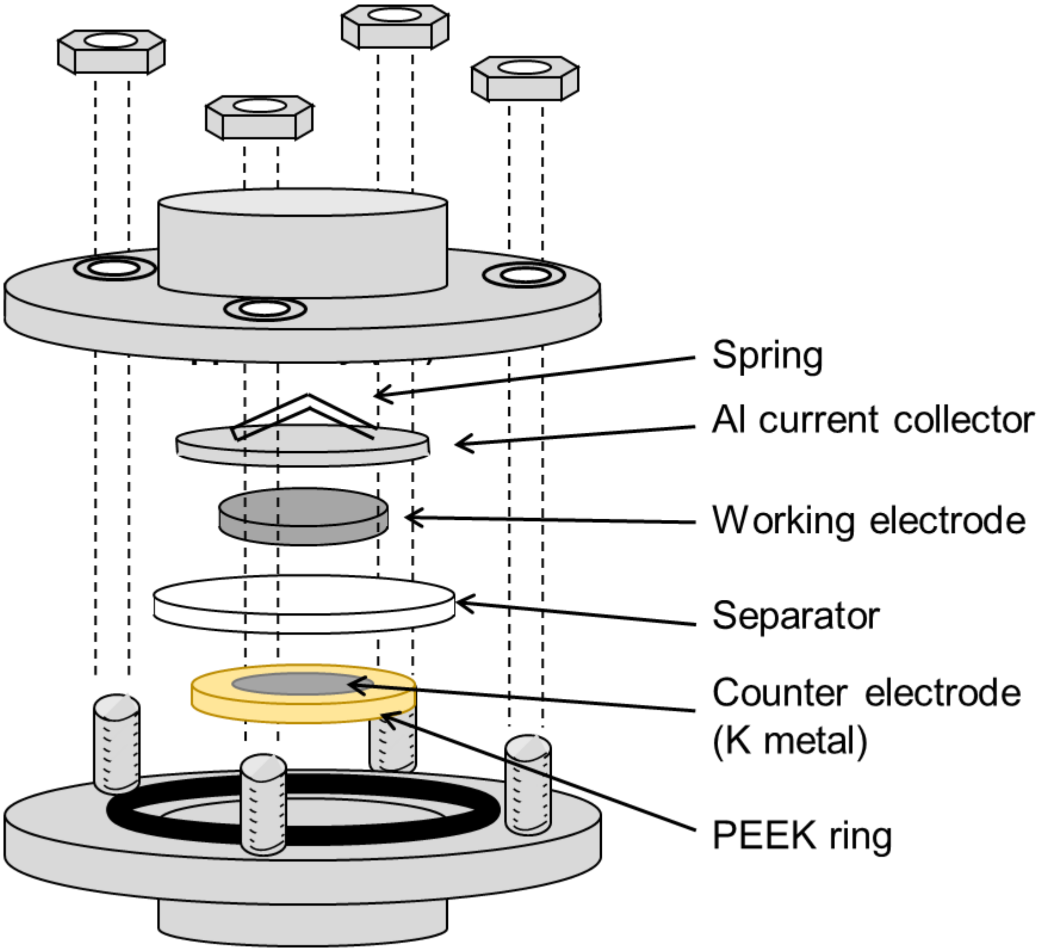

Figure 2-7 A schematic illustration of a flat-type cell in a two-electrode configuration.

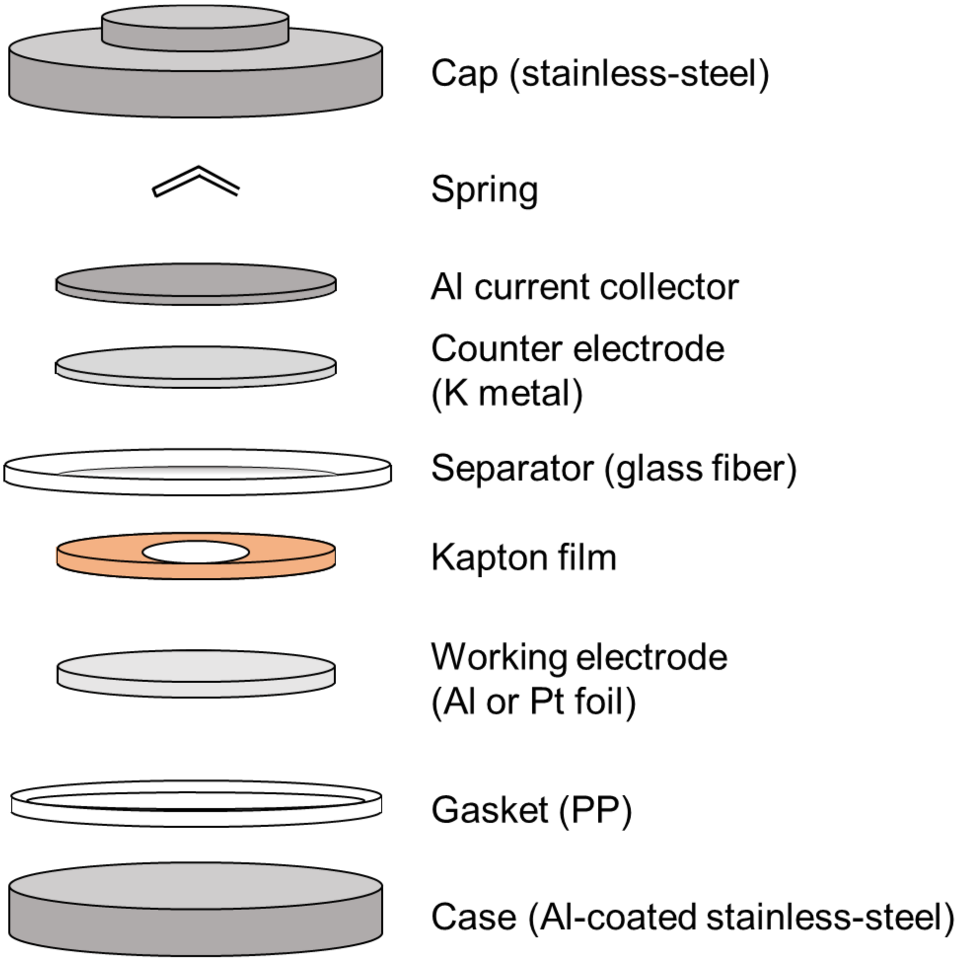

Figure 2-8 A schematic illustration of a 2032-type coin cell in a two-electrode configuration.

References

[1] D. Peters, R. Miethchen, *Journal of Fluorine Chemistry*, **79** (1996) 161.

[2] S. Tawa, Master Thesis, Graduate School of Energy Science, Kyoto University (2015).

Chapter 3

Stage-number Dependence of Intercalated Species for Fluorosilicate Graphite Intercalation Compounds: Pentafluorosilicate vs. Hexafluorosilicate

3.1 Introduction

Graphite is one of the carbon allotropes with a layered structure of so-called graphene consisting of a hexagonal skeleton of sp^2 hybridized carbon atoms. The graphene layers weakly interact with each other by the van der Waals interaction in graphite. This unique structure allows various chemical species to be intercalated into the space between the layers to form graphite intercalation compounds (GICs) [1, 2]. There are some known and possible applications of GICs, such as negative electrodes for lithium ion batteries [3, 4], precursors of exfoliated graphite [5, 6], and electrical conductive materials [7, 8].

The formation of GICs is accompanied by the redox reactions between graphite and a chemical species, resulting in intercalation of cations or anions. Donor- and acceptor-type GICs are formed by reduction and oxidation of graphite, along with intercalation of cations and anions, respectively. A variety of intercalates are known such as Li^+, K^+, and Cs^+ for donor-type, and $AlCl_4^-$, AsF_6^-, and $N(SO_2F)_2^-$ for accepter-type GICs, partly in view of applications as electrodes for energy storage devices [1, 9-11]. Neutral molecules can be co-intercalated together with cations and anions for weakening electrostatic repulsion among them. For donor-type GICs, organic molecules such as furan and epoxyethane can be co-intercalated into K-

GICs to form ternary GICs [12]. Intercalation of organic solvents into graphite together with Li^+ is also known, related to GIC formation for lithium-ion batteries [13, 14]. For AsF_6-GICs, reaction of graphite with AsF_5 brings co-intercalation of AsF_3 and AsF_5 neutral molecules. However, release of the neutral molecules under vacuum was confirmed, and the stability of the neutral molecules is still controversial [15, 16].

One of the most interesting structural properties for GICs is the staging structure, where intercalates are periodically present between graphene layers; the staging structure with intercalates in every n graphene layers is called stage-n. Whereas the Rüdorff–Hoffmann model is a classical and simple staging model, the Daumas–Hérold model is known to explain better how the stage number changes accompanied by the increase of the quantity of intercalates [1, 17, 18]. The characteristic arrangements of intercalates in the graphite gallery are also great interests for theoretical researchers and have been investigated from kinetic aspects using various computational methods [19-22]. For the structure of the stage-n GICs, the following equation (Eq. (3-1)) is known to be established:

$$I_c^{(n)} = l \cdot d_{00l}^{(n)} = d_s + (n-1) \cdot d_g = d_i + n \cdot d_g \tag{3-1}$$

where n is the stage number of GICs, $I_c^{(n)}$ is the repeat distance of stage-n GICs along the c-axis (identity period), $d_{00l}^{(n)}$ is the d spacing of the $00l$ diffraction for stage-n GICs, d_s is the gallery height, d_g is the interplanar distance of pure graphite ($d_g \approx 3.35$ Å), and d_i is the ion height along the c-axis (see Figure 1-3 for the Rüdorff–Hoffmann model of GICs). The stage number is related to properties of GICs. For example, the electric conductivity along the ab-plane of the graphene layer for AsF_6-GICs is the largest for stage-2, although the quantity of intercalates for stage-2 is smaller than that of stage-1 [7, 23]. Therefore, exploring the properties and structure along with the stage number is an interesting subject in this field.

Almost all the intercalated ions in the previous literature are singly charged such as Li^+, K^+, AsF_6^-, and SbF_6^- [1]. There are only a limited number of papers reporting the presence of doubly charged discrete ions, including the GICs of Ca^{2+}, PbF_6^{2-}, SnF_6^{2-}, and GeF_6^{2-} [8, 24, 25]. For PbF_6^{2-} and SnF_6^{2-}, intercalation of singly charged anions of PbF_5^- and SnF_5^- was suggested in other previous papers [26, 27]. The GeF_6^{2-} anion was suggested to be intercalated in the equilibrium with GeF_5^- under the presence of F_2 [25]. Therefore, the intercalation of PbF_6^{2-}, SnF_6^{2-}, and GeF_6^{2-} is still under discussion. Within the tetrafluorides of the 14th-group elements, SiF_4 was not reported to be intercalated as SiF_6^{2-} although intercalation of SiF_5^- to form stage-2 SiF_5-GICs was reported before [28]. In this chapter, chemical states of the intercalates and structures of GICs of fluorosilicate complex anions (SiF_y^{z-}) (SiF_y-GICs) are investigated by structural transformation along with the stage number change and reactivity with PF_5. Results are discussed based on the experimental data obtained by gravimetry, XRD, XRF, and IR.

3.2 Experimental

Silicon tetrafluoride (Mitsui Chemicals, Inc.), PF_5 (Kanto Denka Kogyo Co., Ltd.), and F_2 (Daikin Industries, Ltd.) were used as supplied. Synthetic graphite powder (Union Carbide Corporation, SP-1, 100μm) was dried at 300°C under vacuum for 1 day prior to use.

Synthetic conditions of SiF_y-GICs are summarized in Table 3-1. For the syntheses of SiF_y-GICs under total pressures of SiF_4 and F_2 of or below 2 atm (No. 1, 2, and 3 in Table 3-1), graphite was weighed and loaded in the PFA reactor (typically 100–200 cm^3 in volume) in the glove box. The PFA reactor was evacuated to remove Ar. SiF_4 and F_2 were introduced into the reactor though the reaction manifold up to the target pressure and kept it at the reaction temperatures during the reaction time. The SiF_4 and F_2 gases were added into the reactor once or twice during the reactions to supply the consumed gases. After the reaction, the reactor was cooled down to 298 K and the volatile gases were removed under vacuum for 1 day. For the synthesis of SiF_y-GICs under total pressures of SiF_4 and F_2 higher than 2 atm (No. 4 in Table 3-1), graphite was weighed and loaded in the Ni reactor (typically 100 cm^3 in volume) in the glove box. The Ni reactor was evacuated to remove Ar. SiF_4 and F_2 were introduced into the reaction manifold and condensed into the reactor by cooling the reactor with liquid nitrogen, which resulted in 2.5 atm of SiF_4 and F_2 (total pressure of 5.0 atm). After 24-hour reaction at 298 K, the reactor was warmed up to 323 K and kept for 24 h. Then, the reactor was cooled down to 298 K and the volatile gases were removed under vacuum for 1 day.

Reaction conditions of SiF_y-GICs with PF_5 are summarized in Table 3-2. The synthesized SiF_y-GICs were weighed and loaded in the PFA reactor in the glove box. After the evacuation of Ar in the reactor, PF_5 was introduced into the reactor through the reaction manifold up to 1.0 atm at 298 K. After the reactions overnight, the volatile gases were removed at 298 K under vacuum through a soda lime chemical trap at first and though a cold trap cooled with liquid nitrogen for 1 day.

3.3 Results and discussion

Table 3-1 shows synthetic conditions of SiF_y-GICs by the reaction of graphite with SiF_4 in the presence of F_2. Structures of GICs were characterized by XRD measurements to determine their stage numbers, n. For many fluorocomplex-anion-GICs, the strongest and second strongest peaks can be indexed as $00n+1$ and $00n+2$ diffraction, respectively, due to the similar d_s for fluorocomplex anions to the c-cell constant of graphite [29, 30]. Therefore, in this chapter study, n is determined by Eq. (3-2):

$$(n+1)\cdot d_{00n+1}^{(n)} = (n+2)\cdot d_{00n+2}^{(n)} \ (= I_c^{(n)}) \qquad (3\text{-}2)$$

Eq. (3-2) can be arranged to Eq. (3-3) to evaluate n:

$$n = (2\cdot d_{00n+2}^{(n)} - d_{00n+1}^{(n)}) / (d_{00n+1}^{(n)} - d_{00n+2}^{(n)}) \qquad (3\text{-}3)$$

The n should be integer ideally, and the non-integer number suggests mixing of several stage numbers.

Figure 3-1 (a), (b), (c), and (d) show XRD patterns of SiF_y-GICs formed under 0.1, 0.4, 1.0, and 2.5 atm of SiF_4 and F_2, respectively (No. 1, 2, 3, and 4 in Table 3-1). The diffraction data (see the caption of Figure 3-1) provide n = 4.3, 3.4, 2.8, and 2.3 for (a), (b), (c), and (d), respectively, calculated by Eq. (3-3). Suppose these numbers mean stage mixing, they are regarded as the mixtures of stage-5 and stage-4 for (a), stage-4 and stage-3 for (b), and stage-3 and stage-2 for (c) and (d). These stage numbers are denoted as stage-[5+4], -[4+3], $-[3+2]_H$, and $-[3+2]_L$ for (a), (b), (c), and (d), respectively, in the present study. The interesting feature of these patterns are the position of the $00n+2$ diffraction peaks (the second strongest peaks) for (d) compared with (c).

The second strongest peak of SiF_y-GICs is generally considered to shift to the higher angle along with the decrease of the stage number due to their peak positions above 26.5°. For the relation between the repeat distance along the c-axis and d spacing of $00n+1$ and $00n+2$ diffraction lines for stage-n GICs, Eqs. (3-4) and (3-5) are established using Eq. (3-1):

$$(I_c^{(n)} =)\ (n+1)\cdot d_{00n+1}^{(n)} = d_s + (n-1)\cdot d_g \qquad (3\text{-}4)$$

$$(I_c^{(n)} =)\ (n+2)\cdot d_{00n+2}^{(n)} = d_s + (n-1)\cdot d_g \qquad (3\text{-}5)$$

Similarly for the relation between the repeat distance along the *c*-axis and *d* spacing of 00*n*+2 and 00*n*+3 diffraction lines for stage-*n*+1 GICs, Eqs. (3-6) and (3-7) are established using Eq. (3-1):

$$(I_c^{(n+1)} =)\ (n+2)\cdot d_{00n+2}^{(n+1)} = d_s + n\cdot d_g \tag{3-6}$$

$$(I_c^{(n+1)} =)\ (n+3)\cdot d_{00n+3}^{(n+1)} = d_s + n\cdot d_g \tag{3-7}$$

By eliminating d_s from Eqs. (3-4) and (3-6), Eq. (3-8) is obtained regarding the strongest peak, and by eliminating d_s from Eqs. (3-5) and (3-7), Eq. (3-9) is obtained regarding the second strongest peak as shown below:

$$(d_{00n+1}^{(n)} - d_{00n+2}^{(n+1)}) = (d_{00n+2}^{(n+1)} - d_g) / (n+1) \tag{3-8}$$

$$(d_{00n+2}^{(n)} - d_{00n+3}^{(n+1)}) = (d_{00n+3}^{(n+1)} - d_g) / (n+2) \tag{3-9}$$

In Eq. (3-8), $d_{00n+2}^{(n+1)} - d_g$ is always a positive value in the present study, which suggests $d_{00n+1}^{(n)}$ is larger than $d_{00n+2}^{(n+1)}$ (the 00*n*+1 diffraction line of stage-*n* appears at the lower angle than the 00*n*+2 diffraction line of stage-*n*+1). In Eq. (3-9), $d_{00n+3}^{(n+1)} - d_g$ is always a negative value in the present study, which suggests $d_{00n+2}^{(n)}$ is smaller than $d_{00n+3}^{(n+1)}$ (the 00*n*+2 diffraction line of stage-*n* appears at the higher angle than the 00*n*+3 diffraction line of stage-*n*+1). Thus the strongest and the second strongest peaks shift to lower and higher angles, respectively, accompanied by the decrease of the stage number for GICs of a certain fluorocomplex anion.

The rules above can be applied for SiF_y-GICs at stage-[5+4], -[4+3], and -$[3+2]_H$, as is shown in Figure 3-1 (a), (b), and (c). However, the second strongest diffraction peak for stage-$[3+2]_L$ is located at a smaller angle than that for stage-$[3+2]_H$ in spite of the smaller stage number (Figure 3-1 (c) and (d)). This result suggests that the intercalated species are different between them and the size of the intercalate of (d) is larger than that of (a), (b), and (c). On the other hand, peaks suggesting in-plane structures are not observed unlike other GICs such as Li-GICs and AsF_6-GICs [16, 31, 32].

The reactions of SiF_y-GICs with PF_5 provided crucial information to clarify the intercalates of SiF_y-GICs. Table 3-2 shows their reaction conditions. These reactions proceed based on the stronger F^- affinity of PF_5 than that of SiF_4 because the stability of fluorocomplex-anions-GICs almost depends on F^- affinity of parent fluorides [28]. Figure 3-2 (a), (b), (c), and (d) shows XRD patterns of the products formed by the reactions of SiF_y-GICs (corresponding to Figure 3-1 (a), (b), (c) and (d), respectively) with 1.0 atm of PF_5 at 298 K (No. 1, 2, 3, and 4 in Table 3-2), respectively. The diffraction data (see the caption of Figure 3-2) provide n = 3.1, 2.1, 2.1, and 1.8 for (a), (b), (c) and (d), respectively, according to Eq. (3-3), indicating the formation of stage-3 for (a), stage-2 for (b), and stage-2 for (c). In the case of (d), the stage-1 compound seems to be contained in addition to the stage-2 compound because a shoulder peak at the lower angle is confirmed. Therefore, its stage number is denoted as stage-[2+1]. The gallery heights calculated by Eq. (3-1) are d_s = 7.53, 7.46, and 7.45 for (a), (b), and (c), respectively, which are similar to each other and close to d_s of PF_6-GICs reported [28].

It can be recognized that the peaks ascribed to unreacted graphite in the XRD patterns of SiF_y-GICs at stage-[5+4] and -[4+3] (Figure 3-1 (a) and (b)) disappear after their reactions with PF_5 (Figure 3-2 (a) and (b)). As is known in previous works [28], PF_5 alone does not react with graphite due to its weak oxidation power unlike AsF_5 and SbF_5. Therefore, the reaction of graphite with PF_5 is considered to occur owing to the presence of SiF_y-GICs. The PF_6-GICs are first formed by the reactions of SiF_y-GICs with PF_5, and the PF_6-GICs were reacted with graphite by transfer of PF_6^- between them in the second step. A similar phenomenon was reported for AsF_6-GICs, where stage-1 AsF_6-GICs react with graphite to form stage-2 AsF_6-

GICs [16].

It is noteworthy that the stage number decreases after the reactions of SiF_y-GICs with PF_5; stage-[5+4], -[4+3], -$[3+2]_H$, and -$[3+2]_L$ for SiF_y-GICs changed to stage-3, -2, -2, and -[2+1] for PF_6-GICs, respectively. Although the reactions of stage-2 SiF_5-GICs with PF_5 were investigated in a previous study, stage-2 PF_6-GICs were formed without the change of the stage number [28]. The substitution reaction of SiF_4 with PF_5 to intercalate PF_6^- was confirmed in the previous study, but the decrease of the stage number in the present study cannot be explained solely by the substitution reaction, because it requires to fill the space in the gallery. This result is consistent with the weight change; as shown in Table 3-2, the increases of weight after the reactions are too large to be explained by the simple replacement of SiF_4 with PF_5.

Substitution of SiF_4 with PF_5 to intercalate PF_6^- was confirmed by XRF spectroscopy as shown in Figure 3-3, regarding the reaction No. 4 in Table 3-2. In Figure 3-3 (a), the XRF spectrum of the SiF_y-GIC has a peak at 1.739 keV corresponding to Si-$K\alpha$. After its reaction with PF_5, as shown in Figure 3-3 (b), the peak for Si-$K\alpha$ almost disappears and a peak at 2.013 keV, corresponding to P-$K\alpha$, appears. The negligible Si content (the Si/P ratio < 1.0 at%) suggests complete substitution of SiF_4 with PF_5.

Infrared spectrum of the residual gas after the reaction was also investigated as shown in Figure 3-4 (a). The spectra of PF_5 and SiF_4 are also shown for comparison in Figure 3-4 (b) and (c), respectively. Although the strongest band of SiF_4 at 1030 cm^{-1} (ν_3) cannot be clearly identified because of its overlapping with the ν_5 band of PF_5 under the condition of excess PF_5 gas, the $\nu_1+\nu_4$ combination mode of SiF_4 is certainly observed at 1190 cm^{-1} [33, 34]. This result also indicates that SiF_4 is liberated from SiF_y-GICs by the reactions with PF_5.

As mentioned above, the intercalated species for SiF_y-GICs is considered to change with the decrease of the stage number according to XRD measurements. In addition, reactions of SiF_y-GICs with PF_5 cause the decrease of the stage number and the large weight increase which cannot be explained by the substitution of SiF_4 with PF_5. Two possible models are given below to explain these results (see Figure 3-5 for Model 1 and Figure 3-6 for Model 2).

The first model (Model 1) involves the change of the intercalated species; it is SiF_6^{2-} at high stage numbers and changes from SiF_6^{2-} to SiF_5^- with the decrease of the stage number (Figure 3-5). It can be written in the following Eqs. (3-10) and (3-11) at high stage numbers, and Eq. (3-12) and (3-13) at low stage numbers:

At high stage numbers,

$$x\,C + SiF_4 + F_2 \rightarrow C_xSiF_6 \qquad (3\text{-}10)$$

$$C_xSiF_6 + 2\,PF_5 \rightarrow 2C_{x/2}(PF_6) + SiF_4 \qquad (3\text{-}11)$$

At low stage numbers,

$$x\,C + SiF_4 + 1/2\,F_2 \rightarrow C_xSiF_5 \qquad (3\text{-}12)$$

$$C_xSiF_5 + PF_5 \rightarrow C_xPF_6 + SiF_4 \qquad (3\text{-}13)$$

Here, SiF_6^{2-} and SiF_5^- could be co-intercalated in the same galleries. The increase of gallery height d_s for SiF_y-GICs from stage-[5+4] to -$[3+2]_L$ is well-explained by the change of the intercalate from SiF_6^{2-} to SiF_5^-. The pentagonal bipyramidal SiF_5^- (D_{3h}) provides different heights along the c-axis, depending on its orientation in the gallery (see Figure 3-7 for various orientation of SiF_5^-). The smallest height in GICs for SiF_5^- is achieved when F_{ax} and F_{ex} meet both of the upper and lower graphene layers (Figure 3-7 (a); F_{ax} and F_{ex} are fluorine atoms at the axial and equatorial positions of SiF_5^-). It is considered to occur at low stage number, and Eq. (3-1) provides the ion height along c-axis, d_i, of 4.60 Å from I_c of 11.30 Å for the stage-2 SiF_5-GICs in the previous literature [28]. In addition, the radius of F atom is calculated to be 1.23 Å from d_i (4.60 Å) and Si−F bond lengths of SiF_5^- (1.660 Å for Si–F_{ax} and 1.622 Å for

Si–F_{eq} [35]). On the other hand, the smallest height of the octahedral SiF_6^{2-} (O_h) is achieved when its C_3-axis is located along the c-axis. When the radius of F atom is regarded to be the same in SiF_5- and SiF_6-GICs, d_i of SiF_6^{2-} is determined to be 4.42 Å (Si–F bond length is 1.699 Å according to the literature [36]). Deconvolution of the strongest peak in Figure 3-1 (a) under the assumption that SiF_y-GICs at stage-[5+4] is the mixture of stage-5 and stage-4 SiF_6-GICs with d_i = 4.42 Å can fit the experimental data well as shown in Figure 3-8 for the peak separation of XRD pattern.

On the other hand, the weight change accompanied by the reactions of SiF_y-GICs with PF_5 can also be explained by Model 1. The number of PF_5 molecules to react with one SiF_6^{2-} is two, which means that SiF_6^{2-} brings more weight increase than SiF_5^- along with the change of intercalated anions (SiF_6^{2-} (142.1 g mol^{-1}) → $2PF_6^-$ (290 g (2 mol)$^{-1}$); SiF_5^- (123.1 g mol^{-1}) → PF_6^- (145 g·mol^{-1})). Therefore, the change of intercalates from SiF_6^{2-} to SiF_5^- along with the decrease of the stage number can also rationalize the weight increase. In order to determine the compositions of SiF_y-GICs from the weight changes in the reactions, Eqs. (3-10), (3-11), (3-12), and (3-13), are combined in the following way:

$$x\,C + SiF_4 + (y-4)/2\ F_2 \rightarrow C_xSiF_y \qquad (3\text{-}14)$$

$$C_xSiF_y + (y-4)\ PF_5 \rightarrow (y-4)\ C_{x/(y-4)}(PF_6) + SiF_4 \qquad (3\text{-}15)$$

When a is the weight of graphite and b is the weight of C_xSiF_y in Eq. (3-14), and p is the weight of C_xSiF_y and q is the weight of $C_{x/(y-4)}(PF_6)$ in Eq. (3-15), the equations below are established to calculate x and y to determine the composition of SiF_y-GICs (C_xSiF_y):

$$a/(12\cdot x) = b/(12\cdot x + 28.1 + 19\cdot y) \qquad (3\text{-}16)$$

$$p/(12\cdot x + 28.1 + 19\cdot y) = q/(12\cdot x + 145\cdot(y-4)) \qquad (3\text{-}17)$$

By using the values of a, b, p, and q which are given in Tables 3-1 and 3-2 or 3-3, x and y are calculated to obtain the compositions of SiF_y-GICs as shown in Table 3-3. The y value is nearly 6 for SiF_y-GICs at stage-[5+4] and -[4+3] and decreases from 6 to 5 accompanied by the decrease of the stage number, indicating the ratio of SiF_5^- to SiF_6^{2-} increases with decreasing the stage number. The SiF_y-GICs at stage-$[3+2]_H$ and -$[3+2]_L$, which contain stage-2 GICs, provide y lower than 6 ($y = 5.6$ and 5.2, respectively), suggesting that intercalate species are SiF_6^{2-} for stage-n ($n \geq 3$), and SiF_5^- for stage-2. Moreover, the y value of 5.2 for SiF_y-GICs at stage-$[3+2]_L$, which is close to 5, indicates that SiF_5^- is the major intercalates and it could cause the shift of 00n+2 peaks to lower angles compared with those of the other SiF_y-GICs in the XRD pattern in Figure 3-1.

The presence of SiF_6^{2-} is probably more favorable at high stage numbers in terms of the lattice energy. However, at low stage numbers, the repulsive forces between SiF_6^{2-} anions in different galleries or between positively charged adjacent graphene layers lead to the unstableness of doubly charged SiF_6^{2-}. Particularly for the stage-2 GICs, the repulsive forces between adjacent graphene layers are strong, because the graphene layers facing intercalates are next to each other, which is considered to be a driving force to change the intercalated species from SiF_6^{2-} to SiF_5^- for stage-2 GICs. Another possible reason for the unstableness of SiF_6-GICs at low stage numbers is the too-high charge density on the graphene sheets to compensate the doubly negative charge. Different gallery heights according to chemical species were also suggested for GeF_6^{2-} (d_s = 7.80 Å) and GeF_5^- (d_s = 8.23 Å) [25].

The other model (Model 2) is the case that only SiF_5^- is intercalated in SiF_y-GICs and intercalation of PF_5 neutral molecules occurs along with the substitution of SiF_4 with PF_5 to intercalate PF_6^- as shown in Figure 3-6. The PF_5 molecules may interact with PF_6^- to form dinuclear complex anion such as $P_2F_{11}^-$, although its presence was not confirmed in previous works [37]. The reactions are described in the following Eqs. (3-18) and (3-19):

$$x\,\mathrm{C} + \mathrm{SiF_4} + 1/2\ \mathrm{F_2} \rightarrow \mathrm{C}_x\mathrm{SiF_5} \tag{3-18}$$

$$\mathrm{C}_x\mathrm{SiF_5} + (1+w)\ \mathrm{PF_5} \rightarrow \mathrm{C}_x\mathrm{PF_6(PF_5)}_w + \mathrm{SiF_4} \tag{3-19}$$

When a is the weight of graphite and b is the weight of $\mathrm{C}_x\mathrm{SiF_5}$ in Eq. (3-18), and p is the weight of $\mathrm{C}_x\mathrm{SiF_5}$ and q is the weight of $\mathrm{C}_x\mathrm{(PF_6)(PF_5)}_w$ in Eq. (3-19), the equations below are established,

$$a\ /\ (12\cdot x) = b\ /\ (12\cdot x + 123.1) \tag{3-20}$$

$$p\ /\ (12\cdot x + 123.1) = q\ /\ (12\cdot x + 145 + 126\cdot w) \tag{3-21}$$

By using the values of a, b, p, and q given in Tables 3-1 and 3-2, or 3-3, x and w can be determined. Although the intercalated species is $\mathrm{SiF_5^-}$ for all the SiF_y-GICs, the different orientation of $\mathrm{SiF_5^-}$ in the gallery may cause the different gallery heights. The large weight increase is explained by the co-intercalation of $\mathrm{PF_5}$ neutral molecules along with $\mathrm{PF_6^-}$ (see Table 3-3 for the quantity of co-intercalated $\mathrm{PF_5}$). However, this model has some unfeasible points. The reason for the orientation change along with the decrease of the stage number cannot be rationalized because the increase of d_s is generally unfavorable for the thermodynamic stability of GICs. Moreover, the presence of $\mathrm{PF_5}$ molecules vacuum stable in the gallery is uncertain. Whereas there is a report about the presence of $\mathrm{PF_5}$ molecules in $\mathrm{PF_6}$-GICs (evacuation procedure is not mentioned) [37], a certain $\mathrm{PF_5}$ dissociation pressure over $\mathrm{PF_6}$-GICs was also suggested [28].

3.4 Conclusions

Exploring intercalation of doubly charged anions into graphene layers is not sufficiently studied, but important to extend possibilities of GICs. For the GICs of fluorosilicate anions, only the intercalation of SiF_5^- was reported in a previous work, although the chemical state of SiF_6^{2-} is more widely known. In this chapter, SiF_y-GICs at various stage numbers (the mixtures of stage-5 and -4 (stage-[5+4]), stage-4 and -3 (stage-[4+3]), stage-3 and -2 (stage-$[3+2]_H$), and stage-3 and -2 (stage-$[3+2]_L$)) were synthesized and characterized by gravimetry, XRD, XRF, and IR, and their reactions with PF_5. The XRD measurements for SiF_y-GICs confirmed that SiF_y-GICs at stage-$[3+2]_L$ had a larger gallery height d_s than the others (stage-[5+4], -[4+3], and -$[3+2]_H$), suggesting that different chemical species were intercalated depending on the stage number. The reactions of SiF_y-GICs with PF_5 caused large weight increases and stage-number decreases cannot be explained only by the substitution reaction of SiF_4 with PF_5 to intercalate PF_6^-. The reaction of graphite with PF_5 was also confirmed in the presence of SiF_y-GICs despite the weak oxidation power of PF_5. Two possible models were proposed here to explain these observations. In Model 1, intercalated species was changed from SiF_6^{2-} to SiF_5^- with decreasing the stage number (SiF_6^{2-} for stage-n ($n \geq 3$) and SiF_5^- for stage-2 were suggested), which could explain the change of d_s along the large weight increases and decreases of the stage numbers by the reactions with PF_5. In Model 2, SiF_5^- was regarded as the only intercalated species, but this model suffered from several inconsistencies, and Model 1 was more plausible. Intercalation of multiply charged fluorocomplex anions of the third raw main group element and difference in intercalate species, depending on the stage number, were suggested for the first time in this study, which can make a significant impact on various chemistries related to GICs. Subsequent theoretical and analytical studies in this field are expected near future.

Table 3-1 Synthetic conditions of SiF_y-GICs by the reactions of graphite with SiF_4 in the presence of F_2.

No.	Gas pressure [atm]	Reaction time[a] [h]	Temp.[b] [K]	W_{before}[c] [mg]	W_{after}[c] [mg]	Product
1	SiF_4 : 0.1 F_2 : 0.1	48	298	510	565	SiF_y-GICs (stage-[5+4]) and graphite
2	SiF_4 : 0.4 F_2 : 0.4	24 24	298 348	228	268	SiF_y-GICs (stage-[4+3]) and graphite
3	SiF_4 : 1.0 F_2 : 1.0	44	298	1001	1292	SiF_y-GICs (stage-$[3+2]_H$)
4	SiF_4 : 2.5 F_2 : 2.5	24 24	298 323	396	541	SiF_y-GICs (stage-$[3+2]_L$)

[a] First and second lines for No. 2 and 4 mean reaction times in the first and second steps, respectively. [b] First and second lines for No. 2 and 4 mean reaction temperatures in the first and second steps, respectively. [c] W_{before} and W_{after} denote the weights before and after the reactions.

Table 3-2 Reaction conditions of SiF$_y$-GICs with PF$_5$.[a]

No.	Starting GICs	W_{before}[b] [mg]	W_{after}[b] [mg]	W_{subst}[c] [mg]	Product
1	SiF$_y$-GICs (stage-[5+4]) and graphite	202	224	205	PF$_6$-GICs (stage-3)
2	SiF$_y$-GICs (stage-[4+3]) and graphite	156	182	160	PF$_6$-GICs (stage-2)
3	SiF$_y$-GICs (stage-[3+2]$_H$)	299	348	311	PF$_6$-GICs (stage-2)
4	SiF$_y$-GICs (stage-[3+2]$_L$)	201	221	211	PF$_6$-GICs (stage-[2+1])

[a] The reactions were performed overnight at 298 K under the PF$_5$ pressure of 1.0 atm. [b] W_{before} and W_{after} denote the weights before and after the reactions. [c] W_{subst} denotes the weight after the reaction when the substitution of SiF$_4$ with PF$_5$ to intercalate PF$_6^-$ is assumed to occur.

Table 3-3 Compositions of SiF_y-GICs and PF_6-GICs calculated by the weight changes in the syntheses of SiF_y-GICs and their reactions with PF_5 based on Model 1 and Model 2.

Stage number for SiF_y-GICs	Weight change [mg] Synthesis of SiF_y-GICs	Weight change [mg] Reaction with PF_5	Composition[a] Model 1 SiF_y-GICs	Composition[a] Model 1 PF_6-GICs	Composition[a] Model 2 SiF_y-GICs	Composition[a] Model 2 PF_6-GICs[b]
Stage-[5+4] (and graphite)	510 → 565	202 → 224	$C_{111}SiF_{6.1}$	$C_{53}PF_6$	$C_{95}SiF_5$	$C_{95}PF_6(PF_5)_{0.92}$
Stage-[4+3] (and graphite)	228 → 268	156 → 182	$C_{68}SiF_{6.1}$	$C_{32}PF_6$	$C_{58}SiF_5$	$C_{58}PF_6(PF_5)_{0.92}$
Stage-$[3+2]_H$	1001 → 1292	299 → 348	$C_{39}SiF_{5.6}$	$C_{24.4}PF_6$	$C_{35}SiF_5$	$C_{35}PF_6(PF_5)_{0.54}$
Stage-$[3+2]_L$	396 → 541	201 → 221	$C_{29}SiF_{5.2}$	$C_{24.2}PF_6$	$C_{28}SiF_5$	$C_{28}PF_6(PF_5)_{0.19}$

[a] Details to determine the compositions are given in the text. [b] PF_5 may be stabilized by the interaction with PF_6^- to form dinuclear complex anion, $P_2F_{11}^-$ (its presence is just suggested in the previous study [37]).

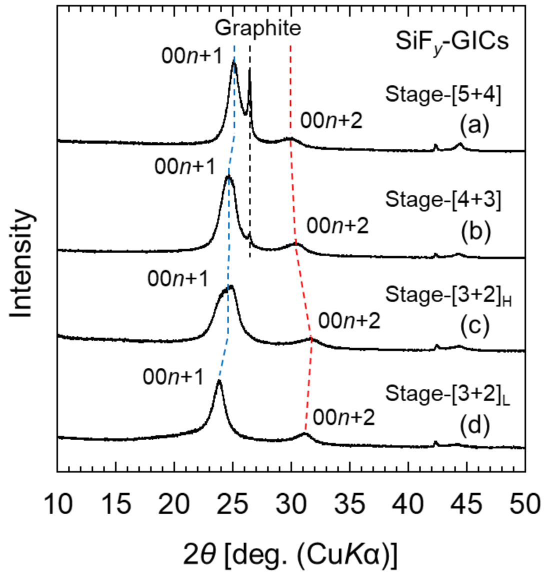

Figure 3-1 XRD patterns of SiF_y-GICs at different stage numbers. Diffraction patterns, (a), (b), (c), and (d), correspond to the products formed by the reactions of graphite with 0.1, 0.4, 1.0, and 2.5 atm of SiF_4 and F_2, respectively (see Table 3-1 for synthetic conditions). The numbers in the brackets show the mixed stage numbers. Diffraction angles of the strongest and the second strongest peaks are 25.10° and 29.94° (d = 3.55 Å, and d = 2.98 Å) for (a), 24.74° and 30.50° (d = 3.60 Å, and d = 2.93 Å) for (b), 24.96° and 31.64° (d = 3.57 Å and d = 2.83 Å) for (c), and 23.85° and 31.17° (d = 3.73 Å and d = 2.87 Å) for (d).

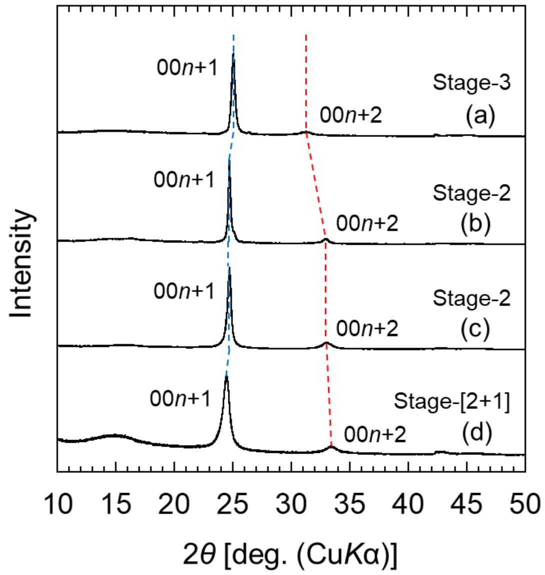

Figure 3-2 XRD patterns of PF_6-GICs at different stage numbers. Diffraction patterns, (a), (b), (c) and (d), correspond to the products formed by the reactions of SiF_y-GICs at stage-[5+4], -[4+3], -[3+2]$_H$, and -[3+2]$_L$ with 1.0 atm of PF_5 at 298 K (see Table 3-2 for reaction conditions). The numbers in the bracket show the mixed stage numbers. Diffraction angles for the strongest and the second strongest peaks are 25.03° and 31.24° (d = 3.56 Å and 2.86 Å) for (a), 24.70° and 32.96° (d = 3.60 Å and 2.72 Å) for (b), 24.72° and 33.03° (d = 3.60 Å and 2.71 Å) for (c), and 24.46° and 33.38° (d = 3.64 Å and 2.68 Å) for (d).

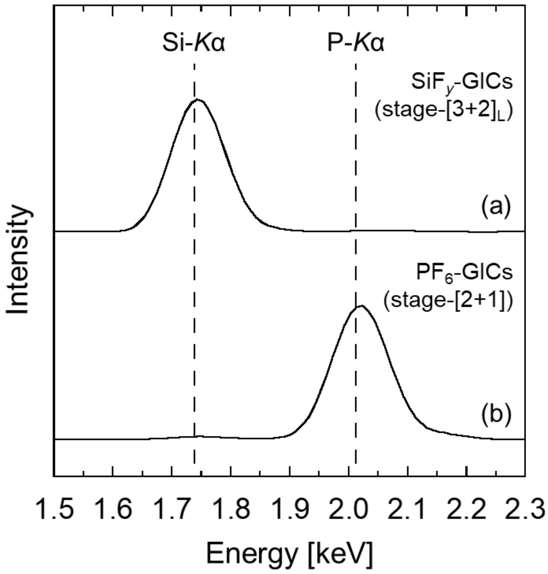

Figure 3-3 XRF spectra of (a) SiF_y-GICs at stage-$[3+2]_L$ obtained by the reaction of graphite with 2.5 atm of SiF_4 and F_2 (No. 4 in Table 3-1) and (b) PF_6-GICs at stage-[2+1] obtained by reaction of SiF_y-GICs at stage-$[3+2]_L$ with PF_5 (No. 4 in Table 3-2). The Si/P ratio in the spectrum (b) < 1.0 at%.

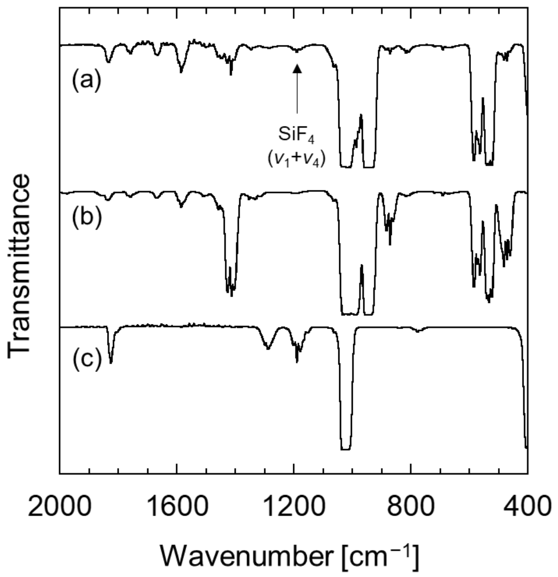

Figure 3-4 IR spectra of (a) the residual gas obtained after the reaction of SiF_y-GICs at stage-$[3+2]_L$ with PF_5 (reaction for No. 4 in Table 3-2), (b) PF_5, and (c) SiF_4. The v_1+v_4 combination mode of SiF_4 is certainly observed at 1190 cm^{-1} although the strongest band of SiF_4 at 1030 cm^{-1} (v_3) cannot be clearly identified because of its overlapping with the v_5 band of PF_5 under the condition of excess PF_5 gas [33, 34].

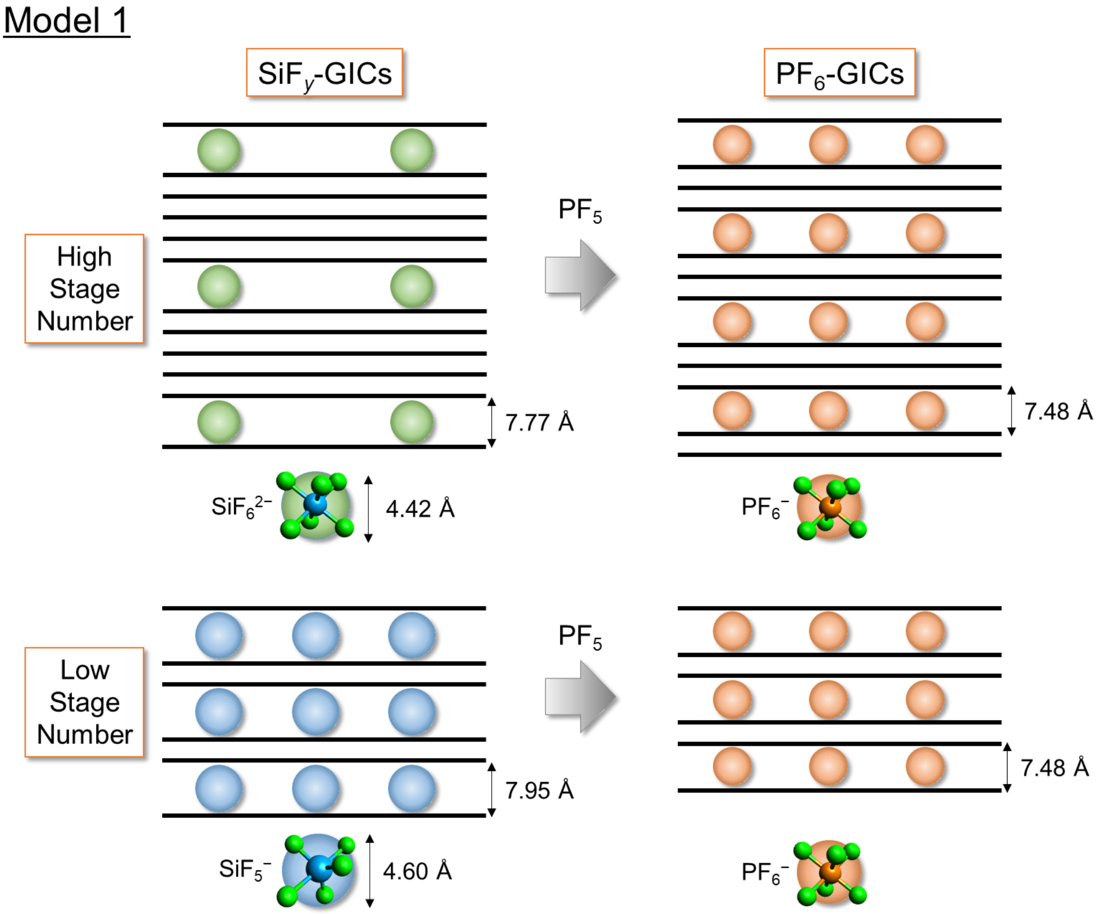

Figure 3-5 A schematic illustration of Model 1 for the reactions of SiF$_y$-GICs with PF$_5$. The intercalated species of SiF$_y$-GICs changes depending on stage number; SiF$_6^{2-}$/SiF$_5^-$ is intercalated into GICs at a high/low stage number (SiF$_6^{2-}$ for stage-n ($n \geq 3$) and SiF$_5^-$ for stage-2 are suggested). Sizes of SiF$_6^{2-}$ and SiF$_5^-$ are calculated based on their molecular and ionic structures and d_s of stage-2 SiF$_5$-GICs from literature (see for Figure 3-7 for details on the heights of SiF$_5^-$ at different orientations) [28, 35, 36]. The number of ions in each gallery for SiF$_6^{2-}$ is considered to be lower than that for SiF$_5^-$, because the distance between doubly charged SiF$_6^{2-}$ anions is longer than that between singly charged SiF$_5^-$ anions due to stronger repulsive forces.

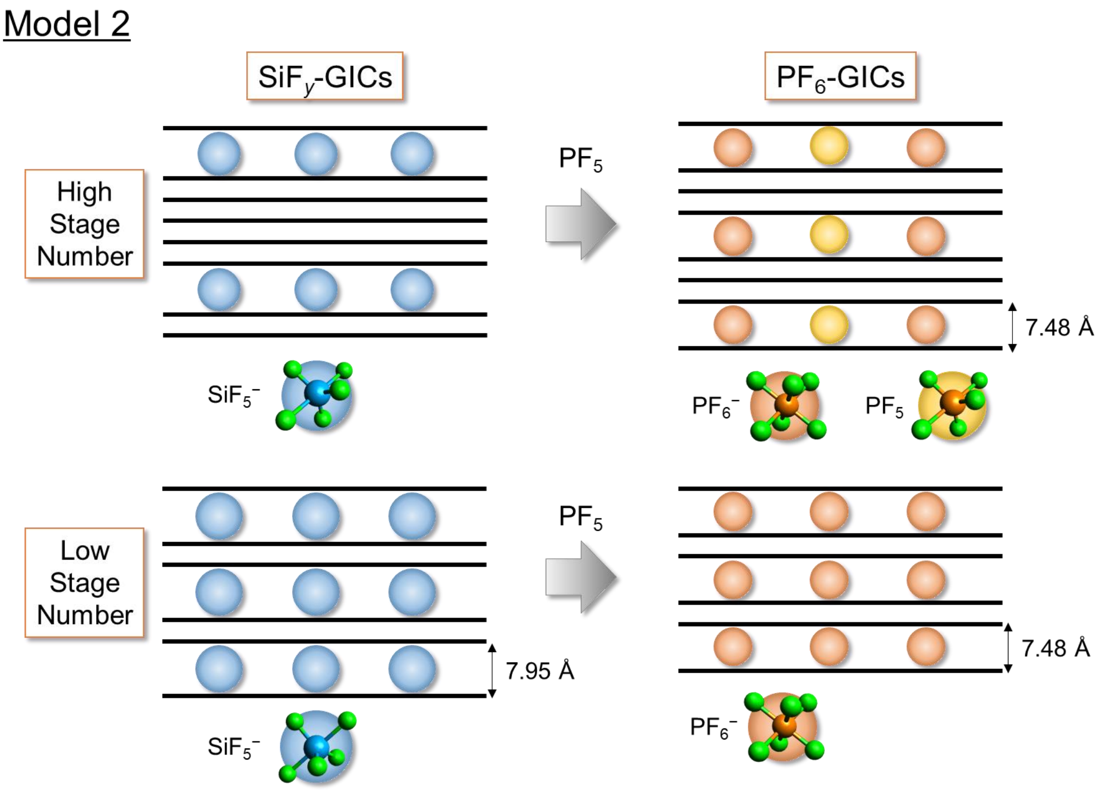

Figure 3-6 A schematic illustration of Model 2 for the reactions of SiF$_y$-GICs with PF$_5$. In Model 2, the intercalated species of SiF$_y$-GICs is SiF$_5^-$ regardless of the stage numbers, but its orientation changes depending on the stage number. The orientation at high stage numbers is achieved to be minimum when F$_{ax}$ and F$_{ex}$ meet both of the upper and lower graphene layers, and that for low stage numbers is achieved when one F$_{ax}$ and one F$_{ex}$ meet one graphene layer and F$_{ax}$ is on the other. On the other hand, the unexpected large weight increases are explained by the intercalation of PF$_5$ neutral molecules (see Table 3-3, for the PF$_5$/PF$_6^-$ ratios of each PF$_6$-GICs. A dinuclear complex anion such as P$_2$F$_{11}^-$ may be formed by the interaction between PF$_5$ and PF$_6^-$ [37]). This model has some unfeasible points as mentioned in the text.

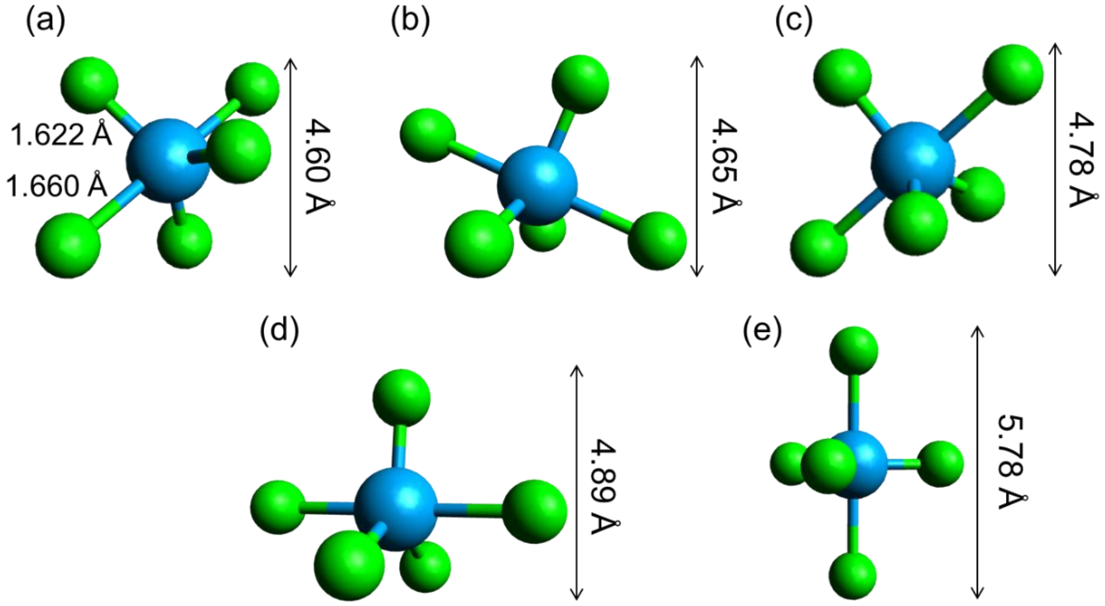

Figure 3-7 Possible orientations of SiF_5^- in GICs and their heights therein. Lengths of Si–F_{ax} and Si–F_{eq} are 1.660 Å and 1.622 Å, respectively, according to the previous literature [35]. The heights were calculated based on Model 1 in the text, where the stage-2 SiF_5-GICs in a previous work (d_s = 7.95 Å) corresponds to the orientation (a) [28]. The resulting radius of fluorine atom is 1.23 Å. Corresponding d_i (Å): (a) 4.60 Å, (b) 4.65 Å, (c) 4.78 Å, (d) 4.89 Å, and (e) 5.78 Å.

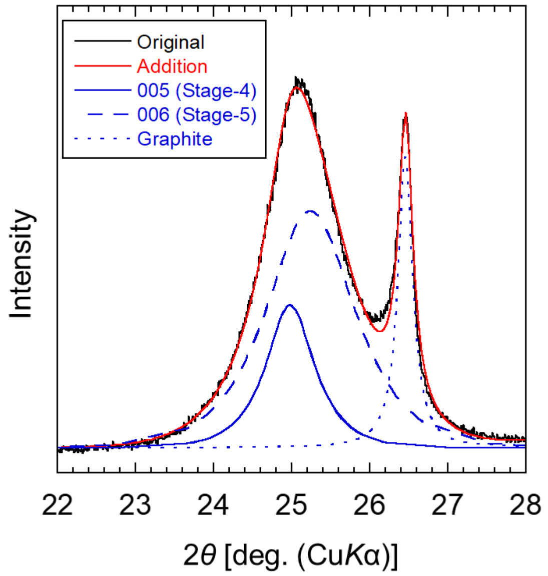

Figure 3-8 Peak deconvolution of the strongest peak of SiF_y-GICs with n = 4.3 under the assumption that it consists of the stage-5 and stage-4 of SiF_6-GICs (d_s = 7.77 Å). Fitting function is Gaussian Lorentzinan cross product. The angles of 005 and 006 diffraction peaks for stage-5 and stage-4 SiF_6-GICs, respectively are 24.98° (d = 3.56 Å) for (a), 25.24° (d = 3.53 Å), and that of 002 diffraction peak of graphite is 26.46° (d = 3.37 Å).

References

[1] M. S. Dresselhaus, G. Dresselhaus, *Adv. Phys.*, **30** (1981) 139.

[2] M. Inagaki, *J. Mater. Res.*, **4** (1989) 1560.

[3] D. Aurbach, B. Markovsky, I. Weissman, E. Levi, Y. Ein-Eli, *Electrochim. Acta*, **45** (1999) 67.

[4] S. J. An, J. Li, C. Daniel, D. Mohanty, S. Nagpure, D. L. Wood, *Carbon*, **105** (2016) 52.

[5] A. Celzard, J. F. Marêché, G. Furdin, *Prog. Mater Sci.*, **50** (2005) 93.

[6] K. Matsumoto, D. Minori, K. Takagi, R. Hagiwara, *Carbon*, **67** (2014) 434.

[7] G. M. T. Foley, C. Zeller, E. R. Falardeau, F. L. Vogel, *Solid State Commun.*, **24** (1977) 371.

[8] T. E. Weller, M. Ellerby, S. S. Saxena, R. P. Smith, N. T. Skipper, *Nat. Phys.*, **1** (2005) 39.

[9] K. Beltrop, P. Meister, S. Klein, A. Heckmann, M. Grünebaum, H.-D. Wiemhöfer, M. Winter, T. Placke, *Electrochim. Acta*, **209** (2016) 44.

[10] M. Zhang, X. Song, X. Ou, Y. Tang, *Energy Stor. Mater.*, **16** (2019) 65.

[11] Y. Kondo, Y. Miyahara, T. Fukutsuka, K. Miyazaki, T. Abe, *Electrochem. Commun.*, **100** (2019) 26.

[12] J. Jegoudez, C. Mazieres, R. Setton, *Synth. Met.*, **7** (1983) 85.

[13] T. Abe, N. Kawabata, Y. Mizutani, M. Inaba, Z. Ogumi, *J. Electrochem. Soc.*, **150** (2003) A257.

[14] G. H. Wrodnigg, *J. Electrochem. Soc.*, **146** (1999) 470.

[15] Y. Yacoby, *Synth. Met.*, **34** (1989) 437.

[16] F. Okino, S. Kawasaki, H. Touhara, *Mol. Cryst. Liq. Cryst.*, **387** (2002) 185.

[17] W. Rüdorff, U. Hofmann, *Z. Anorg. Allg. Chem.*, **238** (1938) 1.

[18] N. Daumas and A. Hérold, *C. R. Acad. Sci. Ser. C.*,, **268** (1969) 373.

[19] E. M. Gavilán-Arriazu, O. A. Pinto, B. A. López de Mishima, D. E. Barraco, O. A. Oviedo, E. P. M. Leiva, *Electrochem. Commun.*, **93** (2018) 133.

[20] E. M. Gavilán-Arriazu, M. P. Mercer, O. A. Pinto, O. A. Oviedo, D. E. Barraco, H. E. Hoster, E. P. M. Leiva, *J. Electrochem. Soc.*, **167** (2020) 013533.

[21] M. Z. Bazant, *Acc. Chem. Res.*, **46** (2013) 1144.

[22] M. Chandesris, D. Caliste, D. Jamet, P. Pochet, *J. Phys. Chem. C*, **123** (2019) 23711.

[23] Y. Gotoh, K. Tamada, N. Akuzawa, M. Fujishige, K. Takeuchi, M. Endo, R. Matsumoto, Y. Soneda, T. Takeichi, *J. Phys. Chem. Solids*, **74** (2013) 1482.

[24] Y. Hattori, M. Kurihara, S. Kawasaki, F. Okino, H. Touhara, *Synth. Met.,* **74** (1995) 89.

[25] E. M. McCarron, Y. J. Grannec, N. Bartlett, *J. Chem. Soc., Chem. Commun.*(1980) 890.

[26] H. Touhara, K. Kadono, H. Imoto, N. Watanabe, A. Tressaud, J. Grannec, *Synth. Met.*, **18** (1987) 549.

[27] L. Fournes, T. Roisnel, J. Grannec, A. Tressaud, P. Hagenmuller, H. Imoto, H. Touhara, *Mater. Res. Bull.,* **25** (1990) 79.

[28] G. L. Rosenthal, T. E. Mallouk, N. Bartlett, *Synth. Met.*, **9** (1984) 433.

[29] G. Schmuelling, T. Placke, R. Kloepsch, O. Fromm, H.-W. Meyer, S. Passerini, M. Winter, *J. Power Sources*, **239** (2013) 563.

[30] X. Zhang, N. Sukpirom, M. M. Lerner, *Mater. Res. Bull.*, **34** (1999) 363.

[31] D. Billaud, F. X. Henry, M. Lelaurain, P. Willmann, *J. Phys. Chem. Solids*, **57** (1996) 775.

[32] F. Okino, N. Bartlett, *J. Chem. Soc., Dalton Trans.*(1993) 2081.

[33] E. A. Jones, J. S. Kirby-Smith, P. J. H. Woltz, A. H. Nielsen, *J. Chem. Phys.*, **19** (1951) 242.

[34] J. E. Griffiths, R. P. C. Jr., R. R. Holmes, *J. Chem. Phys.,* **41** (1964) 863.

[35] D. Schomburg, R. Krebs, *Inorg. Chem.*, **23** (1984) 1378.

[36] R. P. Sharma, R. Bala, R. Sharma, U. Rychlewska, B. Warżajtis, *J. Fluorine Chem.*, **126** (2005) 967.

[37] H. Selig, A. J. Leffler, *Inorg. Chem.*, **32** (1993) 490.

Chapter 4

Deoxofluorination of Graphite Oxide with Sulfur Tetrafluoride

4.1 Introduction

Introduction of fluorine into graphite is an important way to modify its properties because fluorine imparts various unique properties such as hydrophobicity and high thermal and chemical stability to graphite [1]. Fluorine substitution has also been attracting the attention of many researchers as a method to open the band gap of graphene, which is a monolayer of graphite that is known as a zero-band-gap material [2-8]. One of the most common fluorinated graphite materials is poly(carbon monofluoride), $(CF)_n$, obtained by the reaction of graphite with F_2 at around 600 °C [1, 9]. This material is utilized as a solid lubricant and a positive electrode material of lithium primary batteries [1, 10, 11]. The low-temperature reaction of graphite with F_2 (350–400 °C) results in a graphite fluoride with a low degree of fluorination, poly(dicarbon monofluoride), $(C_2F)_n$ [1, 9]. Both $(CF)_n$ and $(C_2F)_n$ are composed of layers with saturated sp^3-hybridized fluorinated carbon frames; each layer of $(CF)_n$ has a carbon skeleton made of cyclohexane chairs, whereas $(C_2F)_n$ has a double-decked layer formed by the connection of two carbon skeletons of cyclohexane chairs with a C−C covalent bond. Another type of fluorinated graphite, C_xF, is formed in the presence of catalytic fluoroacids such as HF and some acidic metal fluorides at room temperature or slightly elevated temperatures [12-18]. The C_xF-type carbon fluoride has covalent C−F bonds and the carbon skeleton is partially buckled at the sp^3-hybridized carbon atoms bound to fluorine atoms [19, 20]. Partially fluorinated or surface fluorinated graphitic compounds are also widely known and are considered for some applications [21-23].

The synthesis of fluorinated graphite has also been attempted using graphite oxide (GO) as the precursor [17, 24-31]. Although the structure of GO is not fully understood, it has oxygen-containing functional groups such as hydroxy, carbonyl, and epoxy groups attached to its carbon skeleton [32]. These functional groups can be substituted with fluorine using fluorinating agents such as F_2 and HF [24-28]. Although the fluorination of GO with pure F_2 leads to a high degree of fluorination, the carbon skeleton is destroyed and the crystallinity of the product is lowered owing to the strong oxidizing power of F_2 [25]. Further, although F_2 can be diluted with N_2 to render the reaction milder and thus prevent the destruction of the carbon skeleton, the fluorination of hydroxy groups does not proceed as expected [24]. Thus, it is difficult to optimize the fluorination of GO using F_2. As for the fluorination of GO with hydrofluoric acid and gaseous HF [27, 28], the reduction occurs in addition to the fluorination of GO. Attempts have been made to fluorinate GO using IF_5, however, IF_5 does not react with GO by itself, and the mixture of F_2, HF, and IF_5 does not seem to facilitate the substitution of the oxygen-containing functional groups with fluorine (graphene oxide is also included here, as the definitions of graphene oxide and graphite oxide are ambiguous) [31].

In this chapter, fluorination of GO using sulfur tetrafluoride (SF_4) as the fluorinating agent was attempted. Sulfur tetrafluoride has the ability to deoxofluorinate both inorganic and organic compounds [33, 34], and is also used as a starting material for preparation of various deoxofluorinating agents such as DAST (Diethylaminosulfur Trifluoride) and Deoxofluor (Bis(2-methoxyethyl)aminosulfur Trifluoride) [35]. Sulfur tetrafluoride can be synthesized from inexpensive starting materials such as S, Cl_2, and NaF [33, 36], and its milder oxidation power than that of F_2 is expected to enable fluorination of GO without destruction of its carbon skeleton. Although there is a report on the fluorination of GO using SF_4 at 800 °C along with the exfoliation of the graphene sheet to obtain fluorinated graphene [37], the fluorination of

GO using SF_4 below the decomposition temperature of GO (≈ 200 °C) has not been explored [38]. The decrease in the reaction temperature leads to a higher degree of fluorination without exfoliation of material, because oxygen-containing functional groups are preserved until fluorination of carbon skeleton with SF_4 occurs. Herein, the effects of SF_4 pressure and reaction temperature on reactivity and structures of the products are systematically investigated. Further, catalytic activity of HF in the reaction of GO with SF_4 is also examined, as HF was reported to function as a catalyst in fluorination of organic compounds using SF_4 [34, 39, 40]. The obtained products were characterized by spectroscopic studies and electron microscopic observation.

4.2 Experimental

Sulfur tetrafluoride (SynQuest Laboratories, 94%) was used as received. The main impurity contained in SF_4 was SOF_2 which does not affect the present experiments. Anhydrous HF (Daikin Industries) was dried over K_2NiF_6 (Ozark-Mahoning Co.) before use. Graphite oxide was prepared by the Brodie method as described in a previous work [41] using natural graphite (Ito Graphite Co., Ltd, Z-5F) as a precursor. The product obtained was dried at 100 °C for 1–2 days under vacuum prior to the treatment with SF_4.

The conditions of the reaction of GO with SF_4 are summarized in Table 4-1. Graphite oxide was weighed and loaded in a nickel reactor (100 mL) under dry Ar atmosphere. After evacuation of Ar in the reactor, SF_4 was introduced into the reactor and was distilled onto GO by cooling the reactor with liquid nitrogen, followed by slow warming up the reactor to the reaction temperature (25 or 150 °C). After the reaction, the reactor was cooled to 25 °C in the case of the reaction at 150 °C, and volatile gases were removed by evacuation through a soda lime chemical trap at first and through a cold trap cooled by liquid nitrogen for 24 h.

Conditions for the reaction of GO with SF_4 in the presence of HF catalyst are shown in Table 4-2. The procedure was the same as that of the reaction of GO with SF_4, except for the introduction of gaseous HF onto GO after the distillation of SF_4. The amount of HF was volumetrically measured and adjusted to be 0.5 atm at 25 °C in the reactor. The FGO-150-5-HF sample (see Table 4-2 for its condition) was treated with H_2O. The sample after treating with H_2O was dried at 100 °C under dynamic vacuum for 2 days. The final product is denoted as FGO-150-5-HF-W.

4.3 Results and discussion

Figure 4-1 shows the IR spectra of GO before and after the reaction with SF_4 under different reaction conditions (temperature and SF_4 pressure, see Table 4-1 for the detailed reaction conditions and the designated names of the products). The reaction did not proceed at 1 atm of SF_4 even when the temperature was elevated to 150 °C. As the thermal decomposition of GO starts around 200 °C [38], no further increase in temperature was attempted. Instead, the SF_4 pressure was increased to 5, 8, and 10 atm. In the case of reactions at 25 °C, changes in the IR spectra were observed for the products obtained at 8 and 10 atm of SF_4. The absorption bands assigned to the O–H stretching (3500 cm^{-1}) and C–O–H bending (1300 cm^{-1}) modes almost disappeared, and the intensity of the peak assigned to the C=O stretching mode (1720 cm^{-1}) decreased, while a new absorption band assigned to the C–F stretching mode (1220 cm^{-1}) appeared [1, 42]. These results indicate that the hydroxyl and carbonyl groups on GO were successfully substituted with fluorine at high SF_4 pressures. On the other hand, characteristic absorption bands assignable to those of solid SF_4 and SOF_2 appeared below 1400 cm^{-1} [43, 44], indicating the presence of SF_4 and SOF_2 in the product even after prolonged evacuation. It has been postulated that alkoxysulfur trifluoride (C–O–SF_3) is formed as a byproduct, or as an intermediate in the reaction of C–OH or C=O with SF_4 [33, 34, 45]. In addition, several types of reactions that lead to C–O–S bonds are known to occur between SF_4 and organic compounds with oxygen-based functional groups [46-48]. However, absence of the S–O stretching band at

~700 cm^{-1} in the IR spectra suggests that the formation of such species are highly improbable [49]. With regard to the presence of SF_4, a band corresponding to the asymmetric vibration mode of $S-F_{ax2}$ (F_{ax} is the F atom at the axial position) was observed at ~660 cm^{-1}, at the same position as that for solid SF_4, while that of gaseous SF_4 appears at ~730 cm^{-1} [43, 50]. This observation indicates that SF_4 is stabilized through the interaction of F_{ax} with an electropositive site between the fluorinated GO layers. On the other hand, the fluorination does not proceed on the epoxy groups, as suggested by the unchanged intensity of the band corresponding to the C–O stretching mode at ~1040 cm^{-1} [51].

Figure 4-2 shows the XRD patterns of GO before and after its reaction with SF_4. Changes in the XRD patterns were observed for the products of reactions at 8 and 10 atm of SF_4 and 25 °C. The 001 diffraction peak at 15.56° corresponding to d = 5.70 Å disappeared after the reaction, while two new broad peaks appeared at 12.9° and 17.9° corresponding to d = 6.9 Å and 5.0 Å, respectively. These two peaks cannot be indexed as a single phase of a layered compound, and the product is considered to consist of two different phases with low crystallinity. The repeating distance of 6.9 Å can be attributed to the stacking of the carbon layer along the *c*-axis. The origin of the peak at 17.9° is currently unknown, although it cannot be attributed to reduced GO because the interlayer distance is too large compared to that of reduced GO (≈ 4 Å) and the corresponding peak disappears after water-washing of the sample formed by the reaction with 5 atm of SF_4 in the presence of HF as described in the following section [27, 28, 30]. Although the structure of the product obtained by the reaction of GO with SF_4 (10 atm) at 25 °C (denoted as FGO-25-10) was also characterized by electron diffraction (ED), the ED pattern only provided information about the graphite layer because of the preferred orientation of the material on the TEM grid (see Figure 4-3). The energy dispersive X-ray spectroscopy (EDS) and electron energy loss spectroscopy (EELS) analyses of FGO-25-10 enabled the identification of only a small amount of sulfur (S/C = 0.003 for EDS and 0.009

for EELS) and a uniform distribution of all the elements (C, O, F, S) (see Figure 4-3), indicating that the two different materials were distributed uniformly in the product.

The thermal behavior of GO also changed after its reaction with SF_4. Figure 4-4 shows the thermogravimetric (TG) curves and differential thermal analyses (DTA) of the pristine GO and FGO-25-10. As shown in the figure, the weight loss of the pristine GO started around 200 °C and accelerated around 300 °C, accompanied by the heat emission detected by DTA. The decomposition of oxygen-containing functional groups caused heat release and gas evolution to bring expansion of GO [52]. On the other hand, such an abrupt weight loss was not observed for FGO-25-10, indicating that the expansion of GO does not occur upon heating because of the elimination of oxygen-containing functional groups during the reaction. There are three possible decomposition paths (liberation of SOF_2 and SF_4, decomposition of oxygen-containing functional groups, and decomposition of C−F) for FGO-25-10. DTA of FGO-25-10 shows two exothermic peaks around 160 °C and 260 °C. The latter peak could correspond to decomposition of oxygen-containing functional groups because the temperature is close to that of exothermic peak for GO. The former could derive from liberation of SF_4 and SOF_2 because decomposition of C–F bonds occur over 500 °C according to thermal behavior of fluorinated graphite [53].

As described above, a high SF_4 pressure is required for the reaction of GO with SF_4. As HF is known to catalyze the deoxofluorination reaction with SF_4 [33], it was expected that the fluorination of GO with SF_4 will be catalyzed by HF. As a controlled reaction, GO was first attempted to react with HF in the absence of SF_4 and no change in the XRD pattern of the material in the following the reaction was confirmed (see Figure 4-5 for the XRD pattern of the product obtained by the treatment of GO with HF (0.5 atm) at 150 °C). The possible reasons for this result in contrast to the previous report on the reaction of graphene oxide with gaseous HF could be different experimental conditions such as the graphite powder used as the precursor, synthetic method of GO or graphene oxide, and fluorination method [28].

Figure 4-6 shows the IR spectra of GO before and after its reaction with SF_4 in the presence of HF (see Table 4-2 for detailed reaction conditions). The intensity of the absorption band of the hydroxyl group (3500 cm^{-1}) decreased significantly, and that of carbonyl group (1720 cm^{-1}) showed some decrease, whose reactions are confirmed in the XPS section below, accompanied by the appearance of the C–F stretching mode (1220 cm^{-1}), even for a reaction at 1 atm of SF_4 and 25 °C in the presence of HF as a catalyst. This is in contrast to the low reactivity of GO with SF_4 in the absence of HF (no reaction occurs at 1 atm and 150 °C, see above) and confirms the catalytic activity of HF in this reaction. Table 4-3 presents the results of the elemental analysis of the products of the reaction of GO with SF_4 in the presence of HF. The F/C molar ratio increased slightly upon increasing the reaction temperature, from a value of 0.09 at 25 °C to 0.10 at 100 °C, and to 0.13 at 150 °C under the same SF_4 pressure of 1 atm although some fluorine wt% could come from SF_4 and SOF_2 in the samples. An increase in the SF_4 pressure from 1 to 5 atm led to a further increase in the F/C ratio to 0.17 at 150 °C. On the other hand, characteristic absorption bands appeared below 1400 cm^{-1} as is the case of the reaction between GO and SF_4 in the absence of HF (see Figure 4-1). Although the intensity ratio of bands assigned to SF_4 to those assigned to SOF_2 is small for the products of the reaction at 1 atm of SF_4, the ratio increased upon increasing the SF_4 pressure from 1 to 5 atm (Figure 4-6 (f) and (g)). This result indicates that the ratio of SF_4 to SOF_2 introduced into the product depends on the SF_4 pressure. On the other hand, the carbon skeleton does not appear to be destructed because no band corresponding to >CF–CF_3 at ~1900 cm^{-1}, generally found upon the destruction, is observed in the IR spectrum [25]. This inference is also supported by the absence of fluorocarbon gases such as CF_4 in the residual gas after the reaction of GO with SF_4 (5 atm) in the presence of HF (see Figure 4-7).

Figure 4-8 shows the XRD patterns of GO before and after its reaction with SF_4 in the presence of HF. A new diffraction peak appears at ~14.9° after the reaction at 25 °C, but the 001 diffraction peak of pristine GO at 15.56° corresponding to $d = 5.70$ Å still remains. The 001 diffraction peak of GO disappears after reactions at 100 and 150 °C. The peak that appeared newly at 14.9° corresponds to $d = 5.94$ Å and is accompanied by a weak shoulder at a higher angle. On the other hand, two broad peaks appear at 13.6° and 17.2°, corresponding to $d = 6.5$ and 5.2 Å, respectively, upon increasing the SF_4 pressure from 1 to 5 atm as in the case of the reaction of GO at a high SF_4 pressure in the absence of HF (see Figure 4-2 (d), (e), and (f)). These observations suggest that these two broad peaks are characteristic for the products of GO treated at high SF_4 pressures and suggest the incorporation of SF_4 and SOF_2 molecules in the product.

Figure 4-9 shows the C 1s XPS spectra of GO before and after its reaction with SF_4 (5 atm) at 150 °C in the presence of HF (denoted as FGO-150-5-HF). Dotted lines show peak positions of carbon atoms with different bonding states (C–C (284.8 eV), $\underline{\text{C}}$–CF (285.4 eV), C–O (286.2 eV), C=O (287.8 eV), C–$\underline{\text{C}}$F (288.5 eV), and O–C=O (289.0 eV)) according to references [24, 54]. Comparison of the two spectra indicates decreases in the intensities of the peaks assigned to C–O and C=O after the reaction of GO with SF_4. On the other hand, peaks assigned to $\underline{\text{C}}$–CF and C–$\underline{\text{C}}$F are observed in the spectrum of FGO-150-5-HF, and fluorine is detected by elemental analysis for this sample (see Table 4-3). The larger binding energy of the C 1s peak of $\underline{\text{C}}$–CF than that of C–C was observed in the XPS spectra of C_xF [55], which is explained by hyperconjugation involving C–F and C–C bonds. An electron is donated from an sp^2 carbon to the antibonding σ^* orbital of C–F bonds, which also leads to a higher chemical shift of F in the ^{19}F NMR spectrum [16, 20, 56]. This can also explain the lower binding energy of the C 1s peak of C–$\underline{\text{C}}$F (288.5 eV) than that of C–F (290 eV, observed in $(CF)_n$, in which all the carbon atoms take sp^3-hybridized form) [15]. There seems to be a peak at ~290 eV in the spectrum of FGO-150-5-HF, which is not assigned in the figure and will be discussed in the following section.

As mentioned above, the presence of SF_4 and SOF_2 in the products is indicated after the reactions. Therefore, FGO-150-5-HF, which is the most fluorinated product, was treated with H_2O to remove SF_4 and SOF_2, followed by the evacuation of volatiles at 100 °C for 2 days. The obtained product is denoted as FGO-150-5-HF-W.

Figure 4-10 shows the IR spectra of pristine GO, FGO-150-5-HF, and FGO-150-5-HF-W. The absorption bands assigned to SF_4 and SOF_2 disappear after water-washing, and the intensity of the C–F stretching band at ~1220 cm^{-1} becomes stronger. This may be due to further fluorination of GO by SF_4 in the presence of water, resulting in the relative increase in the C–F bond on the surface of the material, as IR spectroscopy mainly detects surface species. This hypothesis of further fluorination is further validated by the XPS of FGO-150-5-HF-W in the C 1s region shown in Figure 4-9 (c), wherein the intensity of the peak at ~285.4 eV assigned to $\underline{C}$–CF increases after water-washing. On the other hand, the peak at ~290 eV observed in the spectrum of FGO-150-5-HF disappeared after water-washing (not assigned in the spectrum). Although a peak assigned to C–F is observed at ~290 eV in $(CF)_n$ [15], C–F bonds should be stable in water. Therefore, it is not attributed to C–F. The IR bands assigned to SF_4 and SOF_2 disappeared after water-washing, which could be related to the above result although it is not sure.

Figure 4-11 shows the XRD patterns of pristine GO and FGO-150-5-HF-W. The two broad peaks observed in the pattern of FGO-150-5-HF (Figure 4-8 (e)) disappeared in the pattern of FGO-150-5-HF-W, and a new peak relatively sharp appeared at 15.20° corresponding to d = 5.83 Å, which suggests a slightly longer layer separation than that of the pristine GO (5.70 Å). This result is in contrast to the case for the reaction of graphene oxide with DAST, where the layer separation corresponding to the 001 diffraction peak becomes shorter after the treatment, suggesting the reduction of graphene oxide [30].

Pristine GO and FGO-150-5-HF-W were exposed to air to investigate their reactivity with moisture. The XRD patterns in Figure 4-11 (c, d) show that the 001 diffraction peak of pristine GO shifts to a lower angle from 15.56° (5.70 Å) to 14.02° (6.32 Å) after exposure to the air for 1 hour. On the other hand, FGO-150-5-HF-W exhibits only a slight shift (from 15.20° (5.83 Å) to 15.08° (5.87 Å)) even after 24-h exposure to the air. This result demonstrates that the hygroscopicity of FGO-150-5-HF-W is suppressed significantly compared to that of GO owing to the introduction of fluorine and the elimination of oxygen-containing functional groups such as OH and C=O groups. The F/C ratio of 0.10 for FGO-150-5-HF-W (Table 4-3) is larger than that of the product of the reaction between graphene oxide and SF_4 at 800 °C (F/C = 0.03, including sulfur-containing species) [37], but is slightly smaller than that of FGO-150-5-HF because of the elimination of SF_4 and SOF_2.

Deoxofluorination reactions in this chapter are summarized in Figure 4-12. The reactivity differed significantly depending on the temperature and pressure of SF_4, and the presence or absence of HF catalyst. Compared with the fluorination of GO using pure F_2, fluorination using SF_4 has the advantage of the preservation of the carbon skeleton. The carbon skeleton of GO is destroyed owing to the vigorous oxidation during the deoxofluorination using elemental F_2 [25], while SF_4 does not affect the carbon skeleton because of its weak oxidation power. This is confirmed by the absence of CF_4 in the residual gas of FGO-150-5-HF after the reaction (Figure 4-7) and –CF–CF_3 and CF_3 groups in the products (Figure 4-1, 4-6, and 4-10) [27]. Although fluorination of GO with diluted F_2 occurs more mildly than that with pure F_2 , the fluorination of the hydroxy group is sluggish [24]. In contrast, SF_4 can effectively deoxofluorinate the hydroxy groups without destroying the carbon skeleton.

With regard to the structures of the fluorinated products, their interlayer distance is larger than that of pristine GO. The same results were obtained for the fluorination of GO with F_2 [24, 25]. However, this contradicts the fact that the fluorine atom is smaller in size than the oxygen-containing functional groups. This phenomenon can be interpreted as follows (see the illustration in Figure 4-13). Graphite layers with oxygen-containing groups in GO are highly polar and interact with the adjacent layers. A typical interaction is the hydrogen bonding between the hydrogen atom on the hydroxy group and the oxygen atom of another hydroxy group or epoxy group [57, 58]. F atoms attached to the carbon skeleton only weakly interact with other atoms owing to the small polarizability of F and the strong covalency of the C–F bond, which results in the increase in the interlayer distance of the fluorinated product. The interlayer distance of C_xF-type fluorinated graphite (see Introduction for C_xF-type fluorinated graphite) prepared by the reaction of graphite with F_2 in the presence of HF reached 5.84 Å for the composition of $C_{2.3}F$ [15], which is already larger than that of pristine GO (5.70 Å). The lower hygroscopicity of FGO-150-5-HF-W compared to that of pristine GO also supports this structural model. The lower crystallinity of the fluorinated product compared with that of pristine GO can be also explained by the weak interaction between the layers of the former.

4.4 Conclusions

The reactivity of GO with SF_4 below the decomposition temperature of GO and the structural characterization of the products were presented. The deoxofluorination of GO proceeded only under high SF_4 pressures ($\geq$ 8 atm) at 25 °C. SF_4 and SOF_2 were introduced into GO layer along with deoxofluorination under these conditions. The fluorinated product was not exfoliated upon heating, in contrast to pristine GO that expands to separate layers at ~300 °C. Substitution of oxygen-containing groups with fluorine is considered to suppress the release of gaseous species at high temperatures. The disorganized stacking suggested by the structural analyses might also cause such behavior. The reaction was catalyzed by HF, and in the presence of HF, the deoxofluorination was confirmed even at 1 atm of SF_4 at 25 °C, although SF_4 and SOF_2 were simultaneously introduced into the product. This reaction was further accelerated by the elevation of temperature to 100 and 150 °C, as well as increasing the SF_4 pressure to 5 atm with the introduction of more SF_4 in the product. The SF_4 and SOF_2 species in the products were eliminated by washing with water. Treatment with H_2O was accompanied by further fluorination and the obtained product was less hygroscopic than the pristine GO owing to the hydrophobicity of the fluorine atom. The F/C ratio of the product after water-washing was found to be 0.10, and the final product is regarded as graphite oxyfluoride because the graphite layer in the product was found to contain both fluorine and oxygen (O/C $\approx$ 0.3). Unlike F_2 gas, SF_4 can fluorinate GO without destroying the carbon skeleton, and the reduction of GO was not observed unlike the cases of fluorination using HF and DAST. Further optimization of the reaction condition or the introduction of a more effective catalyst could lead to highly fluorinated graphite materials. Exfoliation of the fluorinated GO is an interesting future work in comparison with fluorinated graphene prepared by fluorination of graphene with diluted F_2 [6-8].

Table 4-1 Conditions of the reaction between GO and SF_4.

Sample name	GO weight [mg]	SF_4 pressure* [atm]	Temp. [°C]	Reaction time [h]	Product weight [mg]
FGO-150-1	92	1	150	24	93
FGO-25-5	167	5	25	72	167
FGO-25-8	274	8	25	72	328
FGO-25-10	329	10	25	72	388

*Pressure at 25°C.

Table 4-2 Conditions of the reaction between GO and SF_4 in the presence of HF.

Sample name	GO weight [mg]	SF_4 pressure* [atm]	Temp. [°C]	Reaction time [h]	HF pressure* [atm]	Product weight [mg]
FGO-25-1-HF	91	1	25	24	0.5	95
FGO-100-1-HF	89	1	100	24	0.5	94
FGO-150-1-HF	90	1	150	24	0.5	96
FGO-150-5-HF**	413	5	150	24	0.5	475

*Pressure at 25°C. **The sample prepared in this condition followed by water-washing is named FGO-150-5-HF-W.

Table 4-3 Results of the elemental analysis of the products of the reaction between GO and SF_4 in the presence and absence of HF.

Sample name	Elements [wt%]					Atomic ratios	
	C	H	F**	S	O*	F/C**	O/C
GO	59.4	1.3	—	—	39.3	—	0.50
FGO-25-10	56.6	0.2	11.5	3.9	27.8	0.13	0.37
FGO-25-1-HF	62.6	0.4	9.1	1.4	26.5	0.09	0.32
FGO-100-1-HF	62.6	0.4	10.2	1.7	25.1	0.10	0.30
FGO-150-1-HF	61.9	0.2	12.5	1.9	23.5	0.13	0.28
FGO-150-5-HF	57.1	0.4	15.5	4.1	22.9	0.17	0.30
FGO-150-5-HF-W	60.8	0.5	9.9	1.9	26.9	0.10	0.33

*Oxygen content was estimated by subtracting weight percentages of all the other elements from 100 wt%. **There could be some contributions of SF_4 and SOF_2 in the products to the value for fluorine.

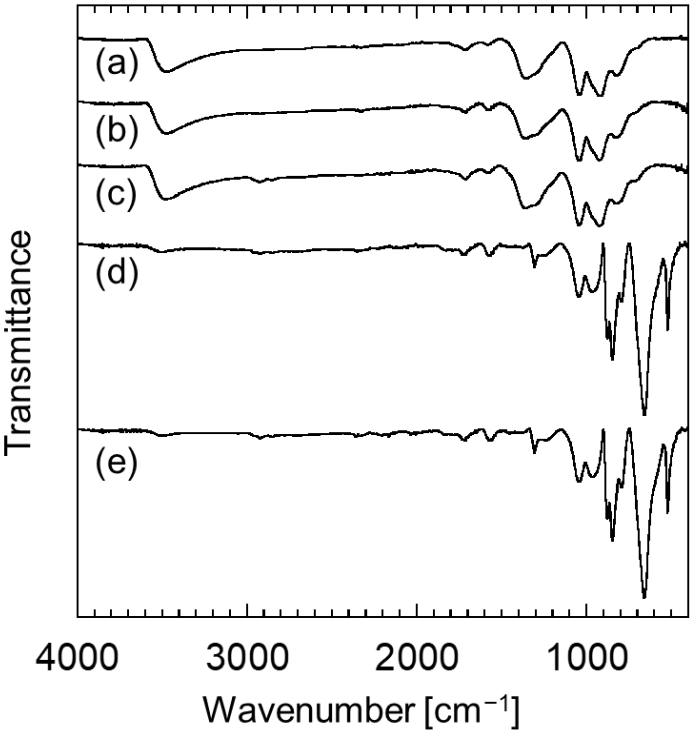

Figure 4-1 IR spectra of GO before and after its reaction with SF_4: (a) pristine GO, (b) FGO-150-1, (c) FGO-25-5, (d) FGO-25-8, and (e) FGO-25-10.

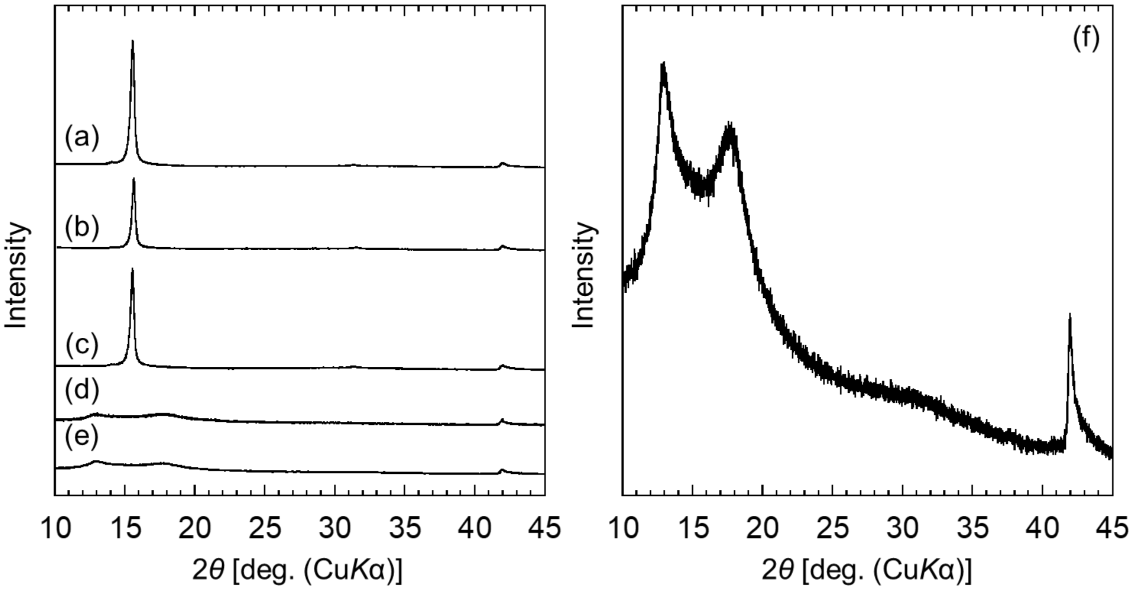

Figure 4-2 XRD patterns of GO before and after its reaction with SF_4. (a) pristine GO, (b) FGO-150-1, (c) FGO-25-5, (d) FGO-25-8, and (e) FGO-25-10. (f) is the magnified pattern of FGO-25-10.

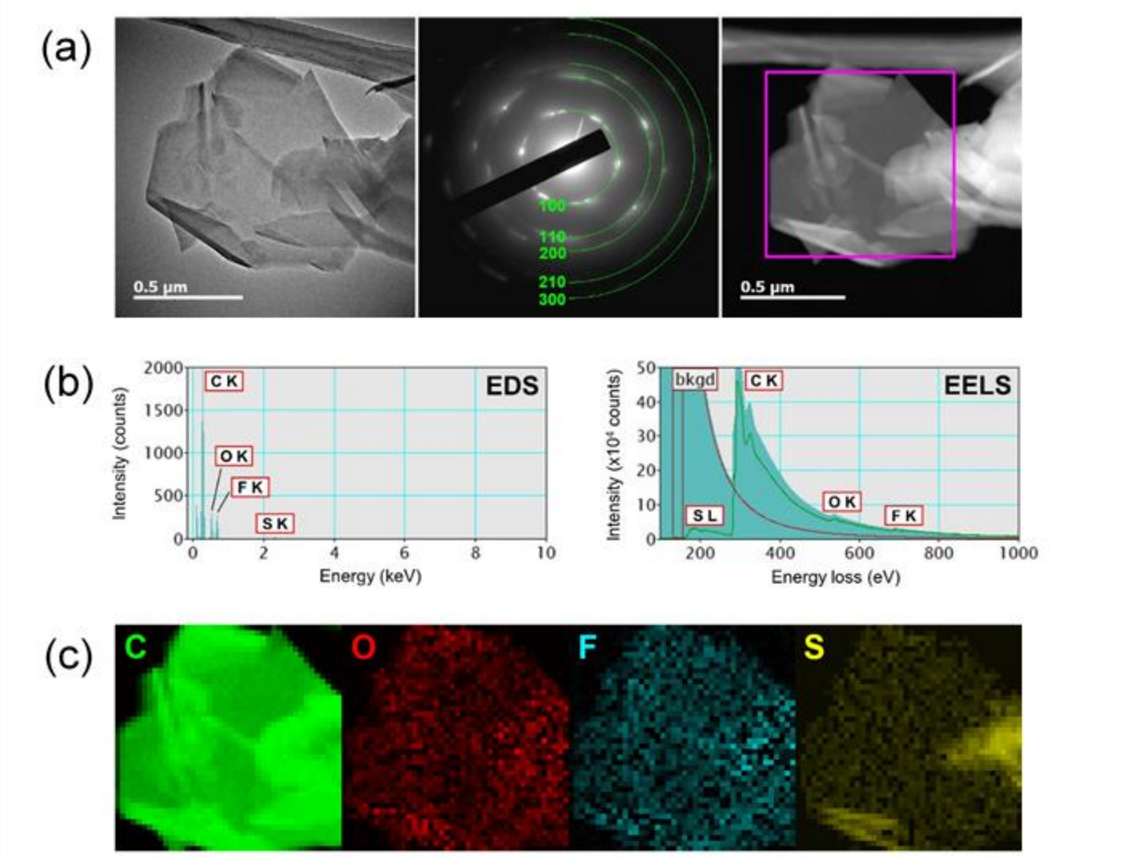

Figure 4-3 TEM and STEM analyses of a flake of FGO-25-10. (a) TEM image (left), ED patterns (center) and annular dark-field STEM image (right). (b) EDS and EELS spectra (left and right, respectively). (c) STEM-EELS chemical maps of carbon (green), oxygen (red), fluorine (blue) and sulfur (yellow) for the area indicated by the purple square in (a). 100, 110, 200, 210, and 300 diffraction correspond to 2.11, 1.24, 1.06, 0.80, and 0.72 Å respectively.

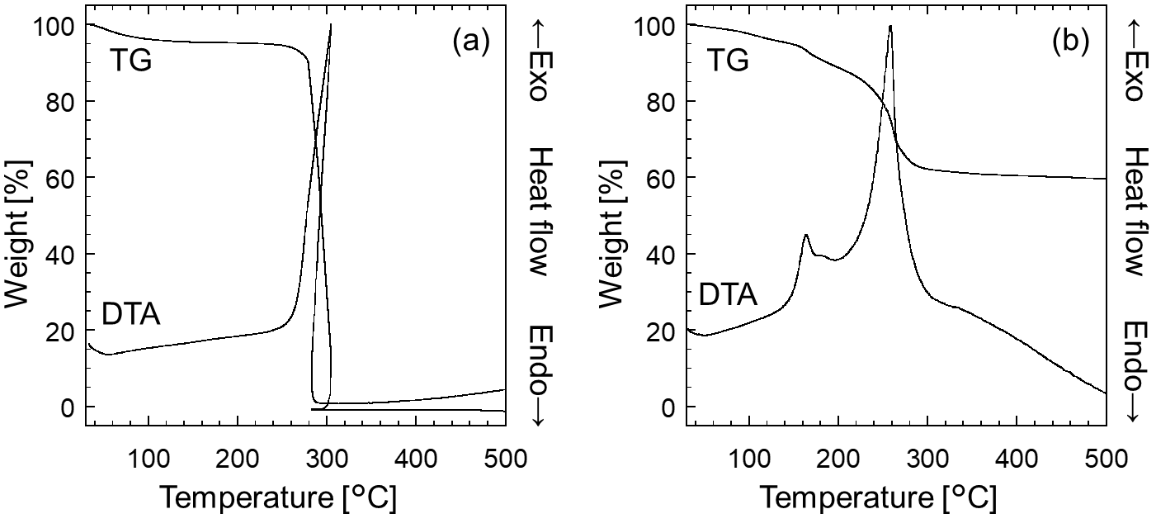

Figure 4-4 TG curves and DTA of (a) pristine GO and (b) FGO-25-10. Pristine GO exothermically expanded at ~300 °C and its weight reached zero.

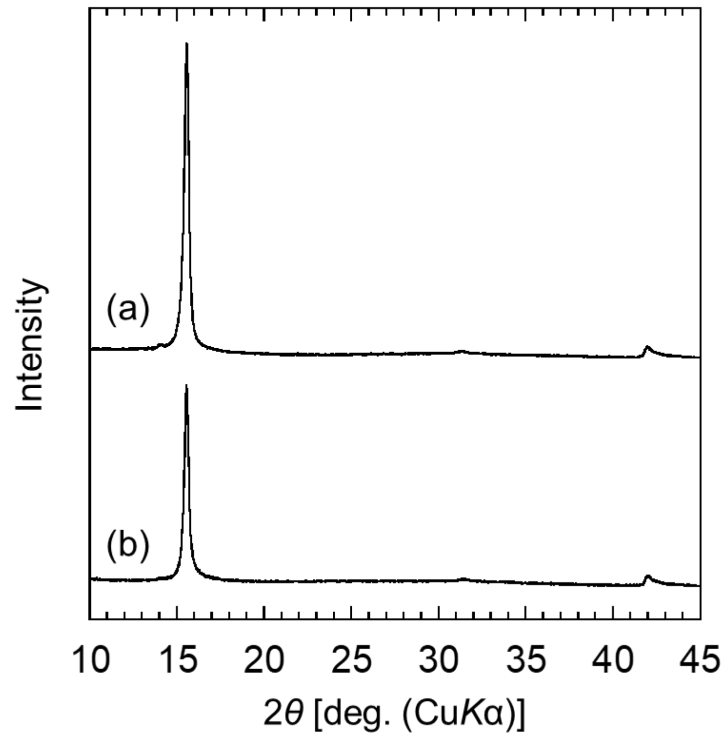

Figure 4-5 XRD patterns of GO (a) before and (b) after the reaction with HF (reaction condition 0.5 atm of HF at 150°C for 24 h).

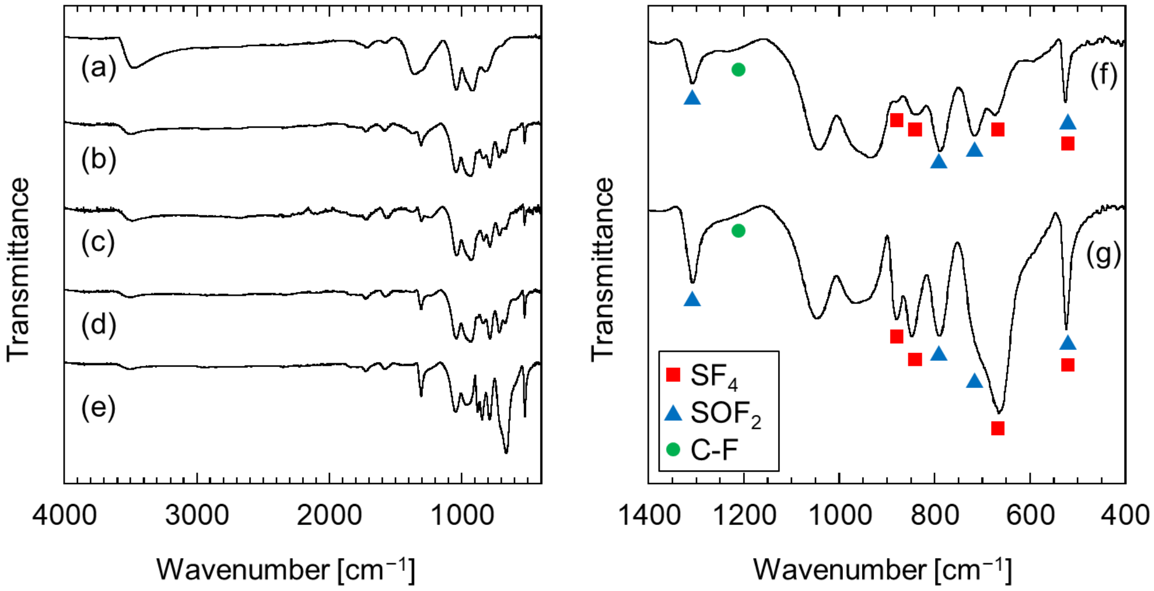

Figure 4-6 IR spectra of GO before and after its reaction with SF_4 in the presence of HF. (a) pristine GO, (b) FGO-25-1-HF, (c) FGO-100-1-HF, (d) FGO-150-1-HF, and (e) FGO-150-5-HF. (f) and (g) show the magnified spectra of FGO-150-1-HF and FGO-150-5-HF (400−1400 cm^{-1}).

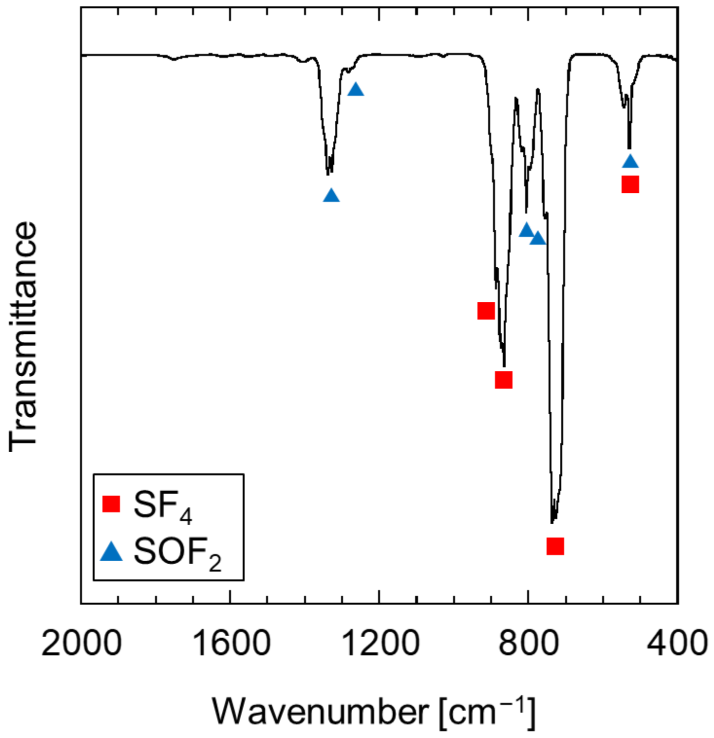

Figure 4-7 IR spectra of the residual gas after reacting GO with 5 atm of SF_4 in the presence of HF at 150°C for 24 h.

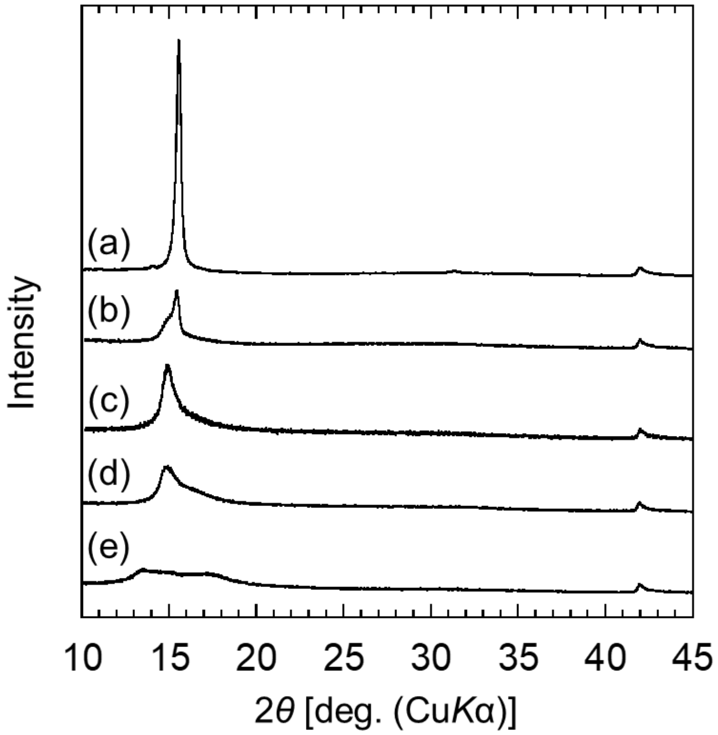

Figure 4-8 XRD patterns of GO before and after its reaction with SF_4 in the presence of HF. (a) pristine GO, (b) FGO-25-1-HF, (c) FGO-100-1-HF, (d) FGO-150-1-HF, and (e) FGO-150-5-HF.

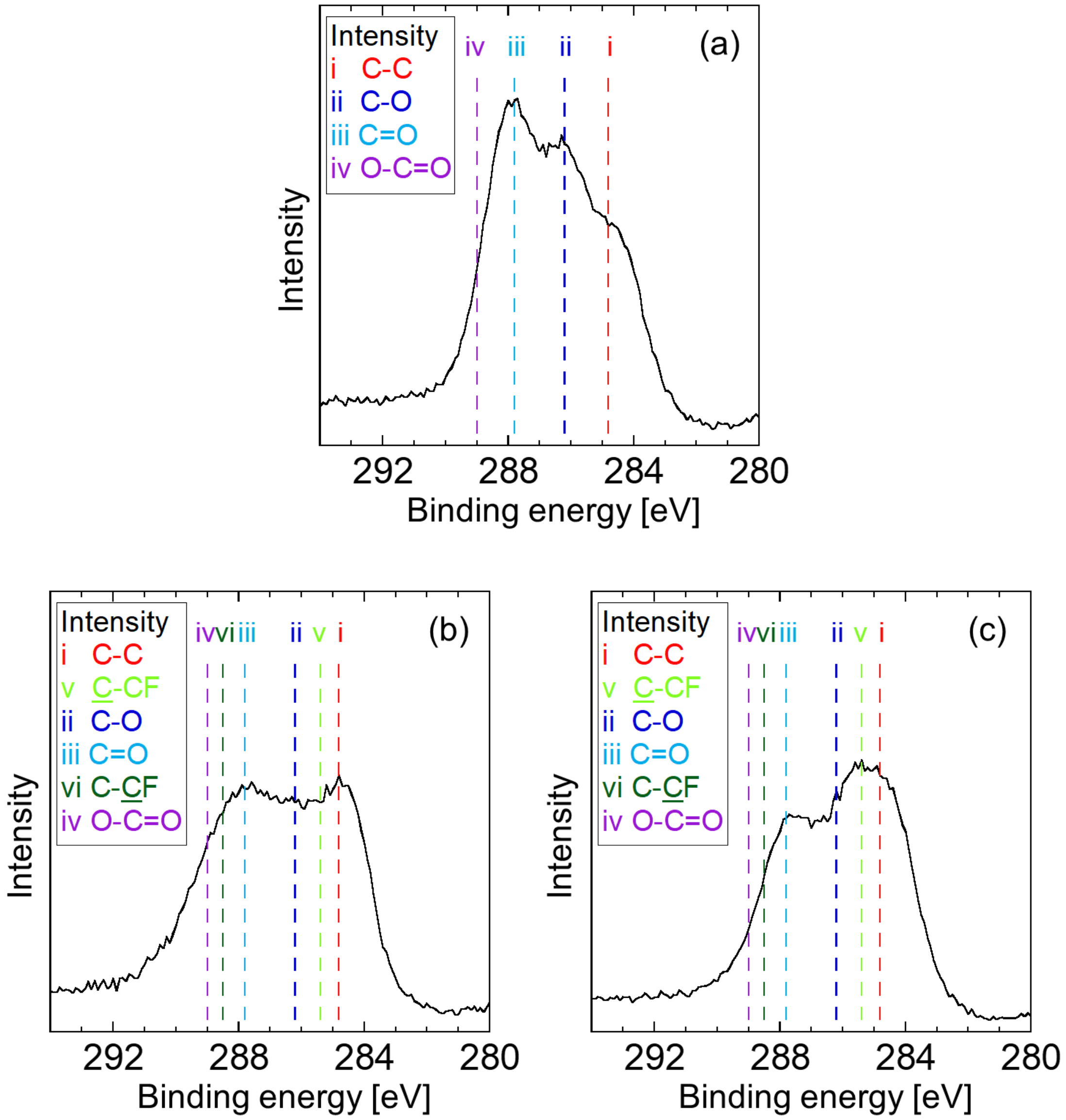

Figure 4-9 XPS spectra (C 1s) of (a) pristine GO, (b) FGO-150-5-HF, and (c) FGO-150-5-HF-W.

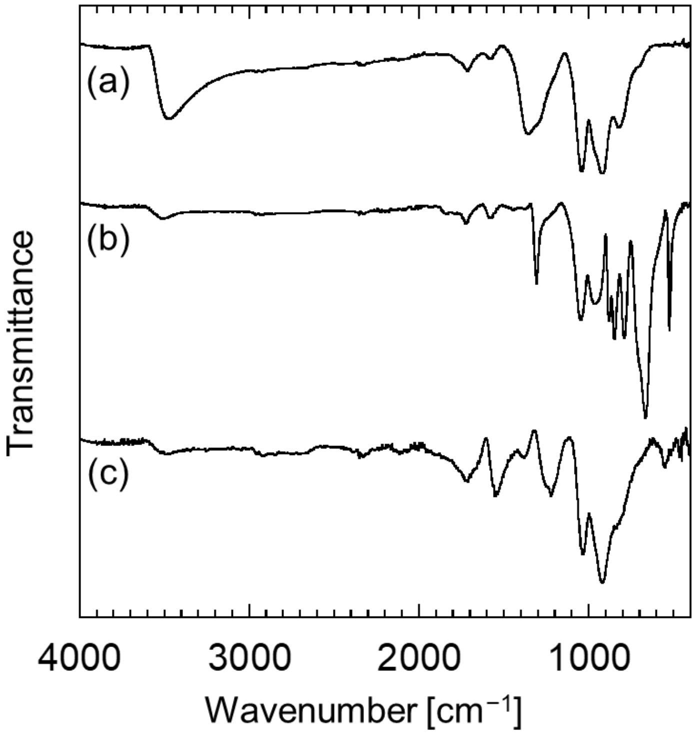

Figure 4-10 IR spectra of (a) pristine GO, (b) FGO-150-5-HF, and (c) FGO-150-5-HF-W.

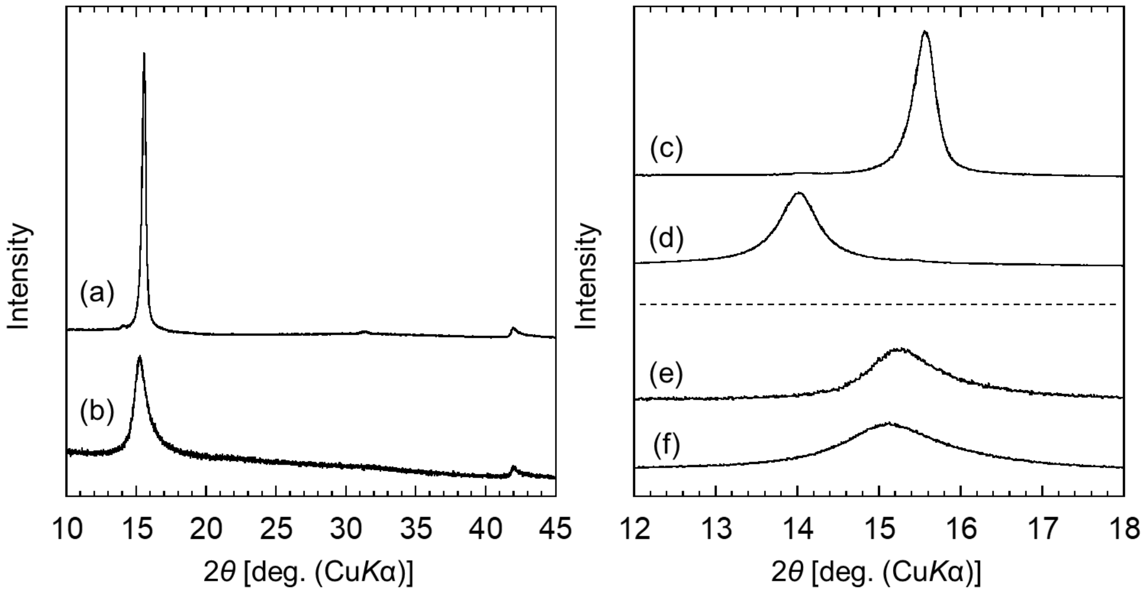

Figure 4-11 XRD patterns of (a) pristine GO and (b) FGO-150-5-HF-W. (c) and (e) are the magnified patterns of pristine GO and FGO-150-5-HF-W. Patterns (d) and (f) are XRD patterns collected after placing pristine GO in the air for 1 h and FGO-150-5-HF-W in air for 24 h, respectively.

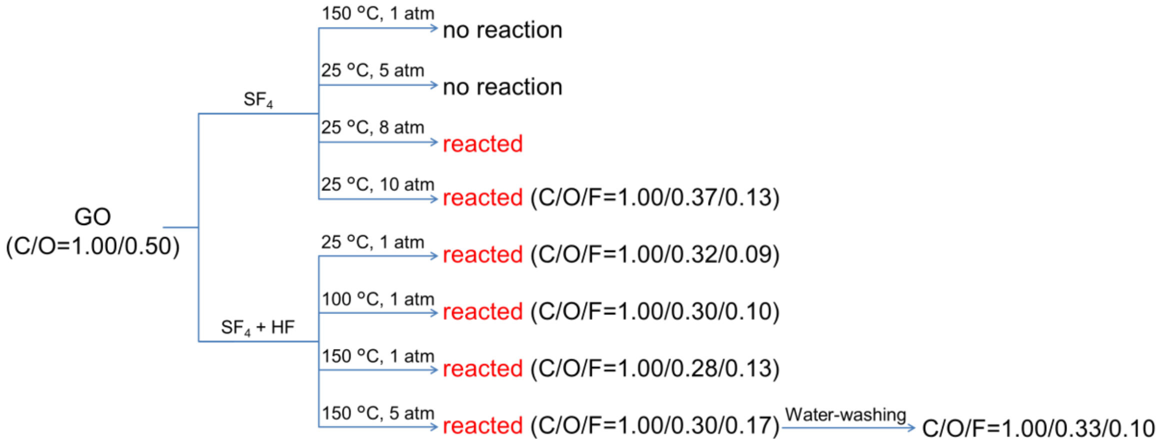

Figure 4-12 Summary of reactions in this chapter. The molar ratios of C/O/F were obtained by elemental analysis (Table 4-3).

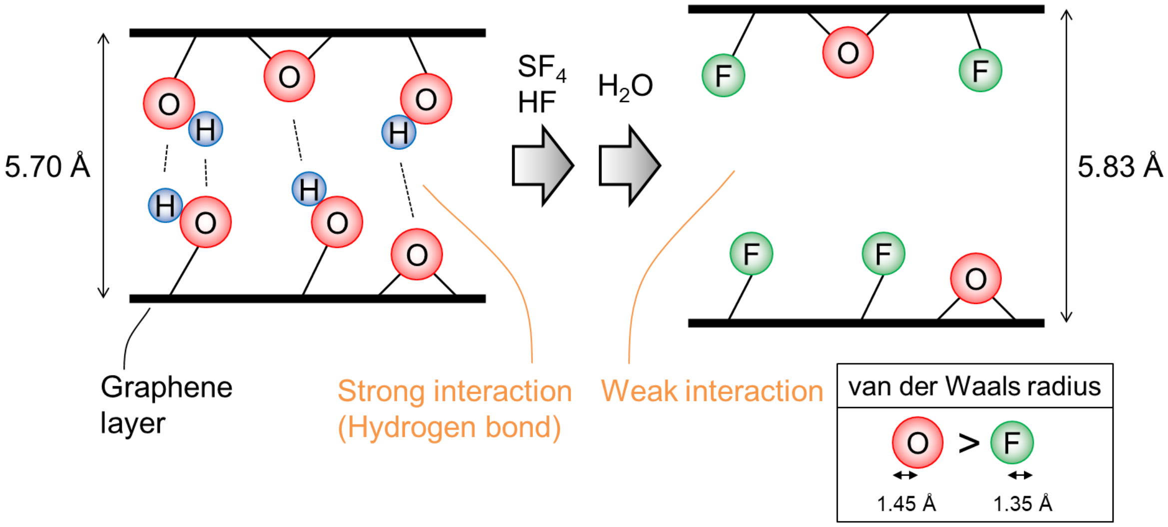

Figure 4-13 A schematic illustration of the deoxofluorination of GO using SF_4. The interlayer distance increases after fluorination owing to the weak interaction, despite the smaller size of F compared to that of O.

References

[1] N. Watanabe, T. Nakajima, H. Touhara, *Graphite Fluorides*, Elsevier, Amsterdam (1988).

[2] R. R. Nair, W. Ren, R. Jalil, I. Riaz, V. G. Kravets, L. Britnell, P. Blake, F. Schedin, A. S. Mayorov, S. Yuan, M. I. Katsnelson, H. M. Cheng, W. Strupinski, L. G. Bulusheva, A. V. Okotrub, I. V. Grigorieva, A. N. Grigorenko, K. S. Novoselov, A. K. Geim, *Small*, **6** (2010) 2877.

[3] K.-J. Jeon, Z. Lee, E. Pollak, L. Moreschini, A. Bostwick, C.-M. Park, R. Mendelsberg, V. Radmilovic, R. Kostecki, T. J. Richardson, E. Rotenberg, *ACS Nano*, **5** (2011) 1042.

[4] J. T. Robinson, J. S. Burgess, C. E. Junkermeier, S. C. Badescu, T. L. Reinecke, F. K. Perkins, M. K. Zalalutdniov, J. W. Baldwin, J. C. Culbertson, P. E. Sheehan, E. S. Snow, *Nano Lett.*, **10** (2010) 3001.

[5] R. Zbořil, F. Karlický, A. B. Bourlinos, T. A. Steriotis, A. K. Stubos, V. Georgakilas, K. Šafářová, D. Jančík, C. Trapalis, M. Otyepka, *Small*, **6** (2010) 2885.

[6] V. Mazánek, A. Libánská, J. Šturala, D. Bouša, D. Sedmidubský, M. Pumera, Z. Janoušek, J. Plutnar, Z. Sofer, *Chem. Eur. J.*, **23** (2017) 1956.

[7] V. Mazánek, L. Pavlikova, P. Marvan, J. Plutnar, M. Pumera, Z. Sofer, *Appl. Mater. Today*, **15** (2019) 343.

[8] S. Hermanová, D. Bouša, V. Mazánek, D. Sedmidubský, J. Plutnar, M. Pumera, Z. Sofer, *Chem. Eur. J.*, **24** (2018) 16833.

[9] Y. Sato, K. Itoh, R. Hagiwara, T. Fukunaga, Y. Ito, *Carbon*, **42** (2004) 2897.

[10] R. L. Fusaro, *Wear*, **53** (1979) 303.

[11] H. Touhara, H. Fujimoto, N. Watanabe, A. Tressaud, *Solid State Ionics*, **14** (1984) 163.

[12] T. Mallouk, N. Bartlett, *J. Chem. Soc., Chem. Commun.* (1983) 103.

[13] I. Palchan, D. Davidov, H. Selig, *J. Chem. Soc., Chem. Commun.* (1983) 657.

[14] C. Delabarre, K. Guérin, M. Dubois, J. Giraudet, Z. Fawal, A. Hamwi, *J. Fluorine Chem.*,

126 (2005) 1078.

[15] Y. Sato, T. Kume, R. Hagiwara, Y. Ito, *Carbon*, **41** (2003) 351.

[16] J. Giraudet, M. Dubois, K. Guérin, C. Delabarre, A. Hamwi, F. Masin, *J. Phys. Chem. B*, **111** (2007) 14143.

[17] A. Hamwi, *J. Phys. Chem. Solids*, **57** (1996) 677.

[18] A. Hamwi, M. Daoud, J. C. Cousseins, *Synth. Met.*, **26** (1988) 89.

[19] Y. Sato, K. Itoh, R. Hagiwara, T. Fukunaga, Y. Ito, *Carbon*, **42** (2004) 3243.

[20] M. Murakami, K. Matsumoto, R. Hagiwara, Y. Matsuo, *Carbon*, **138** (2018) 179.

[21] T. Nakajima, V. Gupta, Y. Ohzawa, H. Iwata, A. Tressaud, E. Durand, *J. Fluorine Chem.*, **114** (2002) 209.

[22] J. Li, K. Naga, Y. Ohzawa, T. Nakajima, A. I. Shames, A. M. Panich, *J. Fluorine Chem.*, **126** (2005) 265.

[23] M.-J. Jung, J. W. Kim, J. S. Im, S.-J. Park, Y.-S. Lee, *J. Ind. Eng. Chem.*, **15** (2009) 410.

[24] O. Jankovský, P. Šimek, D. Sedmidubský, S. Matějková, Z. Janoušek, F. Šembera, M. Pumera, Z. Sofer, *RSC Adv.*, **4** (2014) 1378.

[25] T. Nakajima, Y. Matsuo, *Carbon*, **32** (1994) 469.

[26] T. Nakajima, A. Mabuchi, R. Hagiwara, *Carbon*, **26** (1988) 357.

[27] Z. Wang, J. Wang, Z. Li, P. Gong, X. Liu, L. Zhang, J. Ren, H. Wang, S. Yang, *Carbon*, **50** (2012) 5403.

[28] L. Pu, Y. Ma, W. Zhang, H. Hu, Y. Zhou, Q. Wang, C. Pei, *RSC Adv.*, **3** (2013) 3881.

[29] A. Hamwi, I. Al Saleh, *J. Power Sources*, **48** (1994) 311.

[30] X. Gao, X. Tang, *Carbon*, **76** (2014) 133.

[31] A. Hamwi, I. Al Saleh, D. Djurado, J. C. Cousseins, *Mater. Sci. Forum*, **91-93** (1992) 245.

[32] T. Szabó, O. Berkesi, I. Dékány, *Carbon*, **43** (2005) 3186.

[33] W. C. Smith, *Angew. Chem. Int. Ed.*, **1** (1962) 467.

[34] W. R. Hasek, W. C. Smith, V. A. Engelhardt, *J. Am. Chem. Soc.*, **82** (1960) 543.

[35] W. J. Middleton, *J. Org. Chem.*, **40** (1975) 574.

[36] C. W. Tullock, F. S. Fawcett, W. C. Smith, D. D. Coffman, *J. Am. Chem. Soc.*, **82** (1960) 539.

[37] H. L. Poh, Z. Sofer, K. Klímová, M. Pumera, *J. Mater. Chem. C*, **2** (2014) 5198.

[38] H.-K. Jeong, Y. P. Lee, M. H. Jin, E. S. Kim, J. J. Bae, Y. H. Lee, *Chem. Phys. Lett.*, **470** (2009) 255.

[39] J. Kollonitsch, S. Marburg, L. M. Perkins, *J. Org. Chem.*, **44** (1979) 771.

[40] Y. M. Pustovit, V. P. Nazaretian, *J. Fluorine Chem.*, **55** (1991) 29.

[41] B. MBC, *Ann. Chim. Phys.*, **59** (1860) 466.

[42] T. Szabó, O. Berkesi, P. Forgó, K. Josepovits, Y. Sanakis, D. Petridis, I. Dékány, *Chem. Mater.*, **18** (2006) 2740.

[43] C. V. Berney, *J. Mol. Struct.*, **12** (1972) 87.

[44] R. L. Redington, C. V. Berney, *J. Chem. Phys.*, **43** (1965) 2020.

[45] K. Baum, *J. Am. Chem. Soc.*, **91** (1969) 4594.

[46] P. L. Coe, L. D. Proctor, J. A. Martin, W. A. Thomas, *J. Fluorine Chem.*, **58** (1992) 87.

[47] K. C. Hodges, D. Schomburg, J. V. Weiss, R. Schmutzler, *J. Am. Chem. Soc.*, **99** (1977) 6096.

[48] G. E. Wilson, B. A. Belkind, *J. Am. Chem. Soc.*, **100** (1978) 8124.

[49] Q. Liu, Z. Wu, J. Xu, Y. Lu, H. Li, X. Zeng, *J. Phys. Chem. A*, **121** (2017) 3818.

[50] J. T. Goettel, N. Kostiuk, M. Gerken, *Angew. Chem. Int. Ed.*, **52** (2013) 8037.

[51] D. W. Lee, L. De Los Santos V, J. W. Seo, L. L. Felix, A. Bustamante D, J. M. Cole, C. H. W. Barnes, *J. Phys. Chem. B*, **114** (2010) 5723.

[52] S. Stankovich, D. A. Dikin, R. D. Piner, K. A. Kohlhaas, A. Kleinhammes, Y. Jia, Y. Wu, S. T. Nguyen, R. S. Ruoff, *Carbon*, **45** (2007) 1558.

[53] O. Jankovský, V. Mazánek, K. Klímová, D. Sedmidubský, J. Kosina, M. Pumera, Z. Sofer, *Chem. Eur. J.*, **22** (2016) 17696.

[54] S. Stankovich, R. D. Piner, X. Chen, N. Wu, S. T. Nguyen, R. S. Ruoff, *J. Mater. Chem.*, **16** (2006) 155.

[55] Y. Sato, H. Watano, R. Hagiwara, Y. Ito, *Carbon*, **44** (2006) 664.

[56] A. M. Panich, *Synth. Met.*, **100** (1999) 169.

[57] D. W. Boukhvalov, M. I. Katsnelson, *J. Am. Chem. Soc.*, **130** (2008) 10697.

[58] N. V. Medhekar, A. Ramasubramaniam, R. S. Ruoff, V. B. Shenoy, *ACS Nano*, **4** (2010) 2300.

Chapter 5

Deoxofluorination of Activated Carbon Electrode with Sulfur Tetrafluoride for Electric Double Layer Capacitor

5.1 Introduction

Electrochemical capacitors are energy storage devices with advantages of fast charge-discharge properties and long life span in contrast to secondary batteries [1-3]. High capacitance and improvement of cycle performance is required to widen their application field. Out of various electrode materials [4-8], the most common and widely used one is activated carbon (AC), which has large surface area, high mechanical stability, and low cost [9-11], and is suitable for electric double layer capacitors (EDLCs) storing energy at the electrode surface based on adsorption of ions. The surface of AC is typically covered with oxygen-containing functional groups such as hydroxy, epoxy, and carbonyl groups, and their low resistance against oxidation often limits the operating voltage. Therefore, modification of such functional groups has been a matter of discussion to achieve high-performance operation.

There are a number of reports on surface-modification for porous carbon materials, which affects EDLC-related properties such as wettability, capacitance, and cycleability [11-17]. Functionalization by fluorination was also reported using different fluorination techniques by elemental fluorine, hydrofluoric acid, and ammonium fluoride, resulting in change of surface morphology and increase in capacitance [18-22]. Fluorination is also expected to improve the oxidation resistance because it can reduce HOMO energy level. However, high oxidation power of elemental fluorine could worsen the performance by the introduction of too much F atom in the bulk along with destructing the carbon skeleton. Difficulty in optimization of its reaction conditions is also problematic for the use of elemental fluorine [18]. For fluorinating agents without strong oxidation power, on the other hand, not sufficient examples and discussion have been reported so far, and exploration of new fluorinating agents is required [19-21]. In this chapter, sulfur tetrafluoride (SF_4) is used for this purpose, focusing improvement of oxidative resistance. It has a deoxofluorination (substitution of oxygen-containing functional groups with F atom) ability with a weak oxidation power, and is widely established especially in organic chemistry [23]. Successful introduction of F atom into carbon materials by the use of SF_4 was also reported for a few cases such as graphene oxide [24]. Although there was a report about reactions of AC with SF_4, it did not focus on electrochemical performance but water adsorption properties and surface acidity [25]. Sulfur tetrafluoride is expected to deoxofluorinate only the oxygen-containing functional groups on the AC surface without destructing the carbon skeleton, and its effect on EDLC performance, especially on oxidation resistance, is an interesting topic to be investigated.

5.2 Experimental

Sulfur tetrafluoride was synthesized according to the previous works [23, 26]. A sheet of a mixture (0.2 mm in thickness, 85 wt% of activated carbon (AC, surface area: 2050 m^2 g^{-1}, mean pore diameter: 2.14 nm, and total pore volume: 1.10 cm^3 g^{-1}, 10 wt% of polytetrafluoroethylene as a binder, and 5 wt% of carbon black as a conductive additive) was used for electrochemical measurements after drying under vacuum at 150 ºC for 1 day. Silver trifluoromethanesulfonate (Ag[TfO], FUJIFILM Wako Pure Chemical Corporation, purity > 97 %) for the electrolyte of silver reference electrode (R.E.) was dried at 80 °C for 1 day under vacuum. A solution of 1 M [TEA][BF_4]/PC ([TEA][BF_4]: tetraethylammonium tetrafluoroborate, PC: propylene carbonate, Kishida Chemical Co., Ltd., CPG-00005, water content < 10 ppm) was used as an electrolyte.

Activated carbon (powder and sheet) was treated with 1.0 atm of SF_4 in a PFA reactor (typically 100 cm^3 in volume) and with 5.0 atm of SF_4 in a Ni reactor (100 mL in volume) at 25 °C for 3h. The products obtained by reactions of 1.0 atm and 5.0 atm of SF_4 are denoted as F1-AC and F5-AC, respectively.

Electrochemical measurements were performed using a three-electrode beaker cell with the aid of a VSP electrochemical measurement system (Bio-Logic Sciences Instruments Ltd.). The AC sheet was punched into disks into 6 mm in diameter (surface area: 0.283 cm^2 on one-side) as working electrodes (W.E.) and into 16 mm in diameter (surface area: 2.01 cm^2 on one-side) as counter electrodes (C.E.). The pristine or deoxofluorinated AC sheet was pressed on Al mesh for W.E. and immersed in the electrolyte overnight for impregnation and purification. Two pristine AC sheets of 16 mm diameter were pressed on Al mesh (both sides) for C.E. Electrode potential was referenced to the Ag^+/Ag redox couple. The reference electrode was made of Ag wire immersed in the electrolyte (1 M [TEA][BF_4]/PC) containing 0.01 M of Ag[TfO] and was separated from the electrolyte by a porous glass frit (RE-6, EC Frontier Co., Ltd.). Charge-discharge tests were performed with a lower cutoff potential of 0.0 V and upper cutoff potentials varying from 0.5 to 1.5 V at intervals of 0.1 V. Positive and negative polarizations are defined as charge and discharge, respectively, in this chapter. The cell was charged and discharged for 10 cycles for each upper cutoff potential consecutively at a constant current density of 235 mA $(g\text{-}AC)^{-1}$. Capacitance was calculated based on the slopes of the discharge curve.

5.3 Results and discussion

Figure 5-1 shows C1s and F1s XPS of AC before and after reacting with 1.0 or 5.0 atm of SF_4 at 25 °C for 3h. In the C1s spectra (Figure 5-1 (a)), there is a peak at 284.3 eV corresponding to the C–C bonds for AC, F1-AC, and F5-AC [19, 20, 22, 26]. Although this peak has a weak shoulder at the high energy region corresponding to oxygen-containing functional groups, clear differences are not observed in any cases. On the other hand, the F1s region (Figure 5-1 (b)) of F1-AC and F5-AC has a peak at 686.1 eV in contrast to the pristine AC, which confirms the introduction of fluorine by the reactions with SF_4. Table 5-1 lists the chemical composition and F/C and O/C atomic ratios on the surface of the samples based on the peak area obtained by XPS. These results indicate that increase in SF_4 pressure causes a higher degree of deoxofluorination; the F/C ratio increases and the O/C ratio decreases with increasing SF_4 pressure. While XPS provides chemical compositions on the surface, combustion analysis shown in Table 5-1 provides information of the bulk. The F/C ratio on the surface is larger than that of the bulk, suggesting successful deoxofluorination of surface oxygen-containing functional groups without destructing carbon skeleton. Although surface modification was tried to confirm by infrared spectroscopy, there was no noticeable difference in the obtained spectra before and after the treatment by SF_4.

Effects of deoxofluorination of AC with SF_4 on the electrochemical performance were investigated by galvanostatic charge-discharge tests. Figure 5-2 (a) shows charge-discharge curves of AC, F1-AC, and F5-AC at the 10th cycle of the different cutoff potentials (0.0-0.5 V, 0.0-1.0 V, and 0.0-1.5 V vs. Ag^+/Ag). These charge-discharge curves show typical shapes of an AC electrode in EDLCs. Figure 5-2 (b) shows the resulting capacitances of the discharge process. The capacitances obtained for F1-AC and F5-AC are larger than that of AC in the high cutoff potential range and the entire cutoff range, respectively, and deoxofluorination with SF_4 effectively increases capacitances of the AC electrodes. Figure 5-2 (c) shows the calculated coulombic efficiencies during cycling, which suggests that coulombic efficiencies are also improved by deoxofluorination in the entire range for F5-AC and in the high cutoff potential range for F1-AC. Although the relatively low coulombic efficiencies observed are due to small cycle numbers and are expected to be improved by longer cycling.

5.4 Conclusions

Surface modification of AC is an effective way to improve electrode performance in EDLCs. In this chapter, deoxofluorination of AC with SF_4 and its effects on the electrochemical performance as an electrode material for EDLCs were investigated. The XPS analysis confirmed introduction of F atom and decrease of oxygen-containing functional groups by the SF_4 treatment, and higher pressure of SF_4 was more effective for this purpose. Comparison of elemental analysis by XPS and combustion methods revealed that F atom was selectively introduced to the surface compared to the bulk, suggesting that the reaction proceeded mainly involving deoxofluorination of oxygen-containing functional groups on the surface of AC. Charge-discharge tests indicated slight increase of capacitance and improvement of coulombic efficiency by deoxofluorination, especially the treatment at high pressure.

Table 5-1 Chemical compositions of AC, F1-AC, and F5-AC obtained by XPS and combustion analysis.

<table>
<tr><th colspan="6">XPS for surface</th></tr>
<tr><th rowspan="2">Samples</th><th colspan="3">Elements [at%]</th><th colspan="2">Atomic ratios</th></tr>
<tr><th>C</th><th>F</th><th>O</th><th>F/C</th><th>O/C</th></tr>
<tr><td>AC</td><td>95.8</td><td>—</td><td>4.2</td><td>—</td><td>0.044</td></tr>
<tr><td>F1-AC</td><td>93.3</td><td>4.4</td><td>2.3</td><td>0.047</td><td>0.025</td></tr>
<tr><td>F5-AC</td><td>91.8</td><td>6.2</td><td>2.0</td><td>0.067</td><td>0.022</td></tr>
<tr><th colspan="6">Combustion analysis for bulk</th></tr>
<tr><th rowspan="2">Samples</th><th colspan="3">Elements [wt%]</th><th colspan="2">Atomic ratio</th></tr>
<tr><th>C</th><th>F</th><th>H</th><th colspan="2">F/C</th></tr>
<tr><td>AC</td><td>94.3</td><td>0</td><td>0.7</td><td colspan="2">—</td></tr>
<tr><td>F1-AC</td><td>90.0</td><td>2.1</td><td>0.6</td><td colspan="2">0.015</td></tr>
<tr><td>F5-AC</td><td>89.2</td><td>2.4</td><td>0.6</td><td colspan="2">0.017</td></tr>
</table>

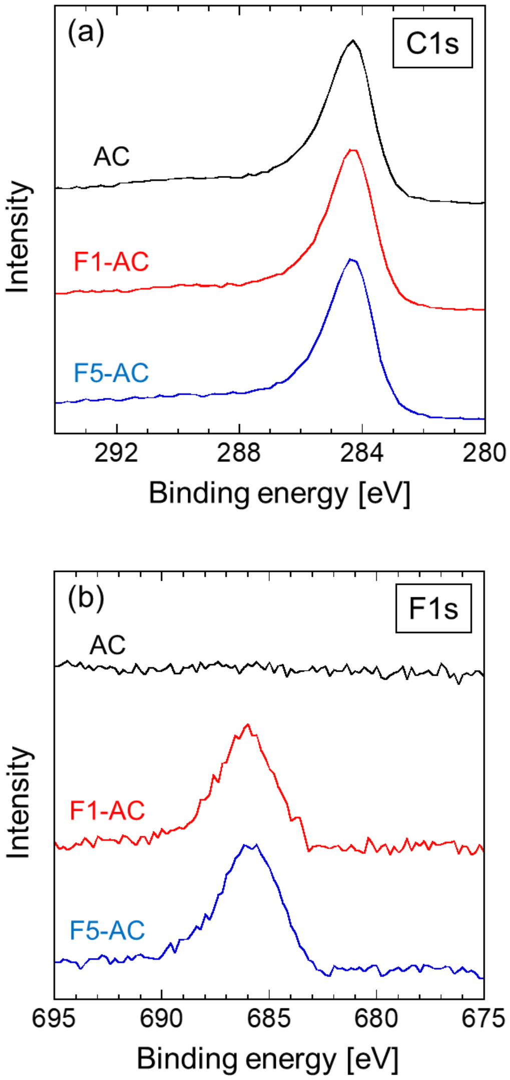

Figure 5-1 XPS of AC before and after reacting with 1.0 atm and 5.0 atm of SF_4 at 25°C for 3h in the (a) C1s and (b) F1s regions.

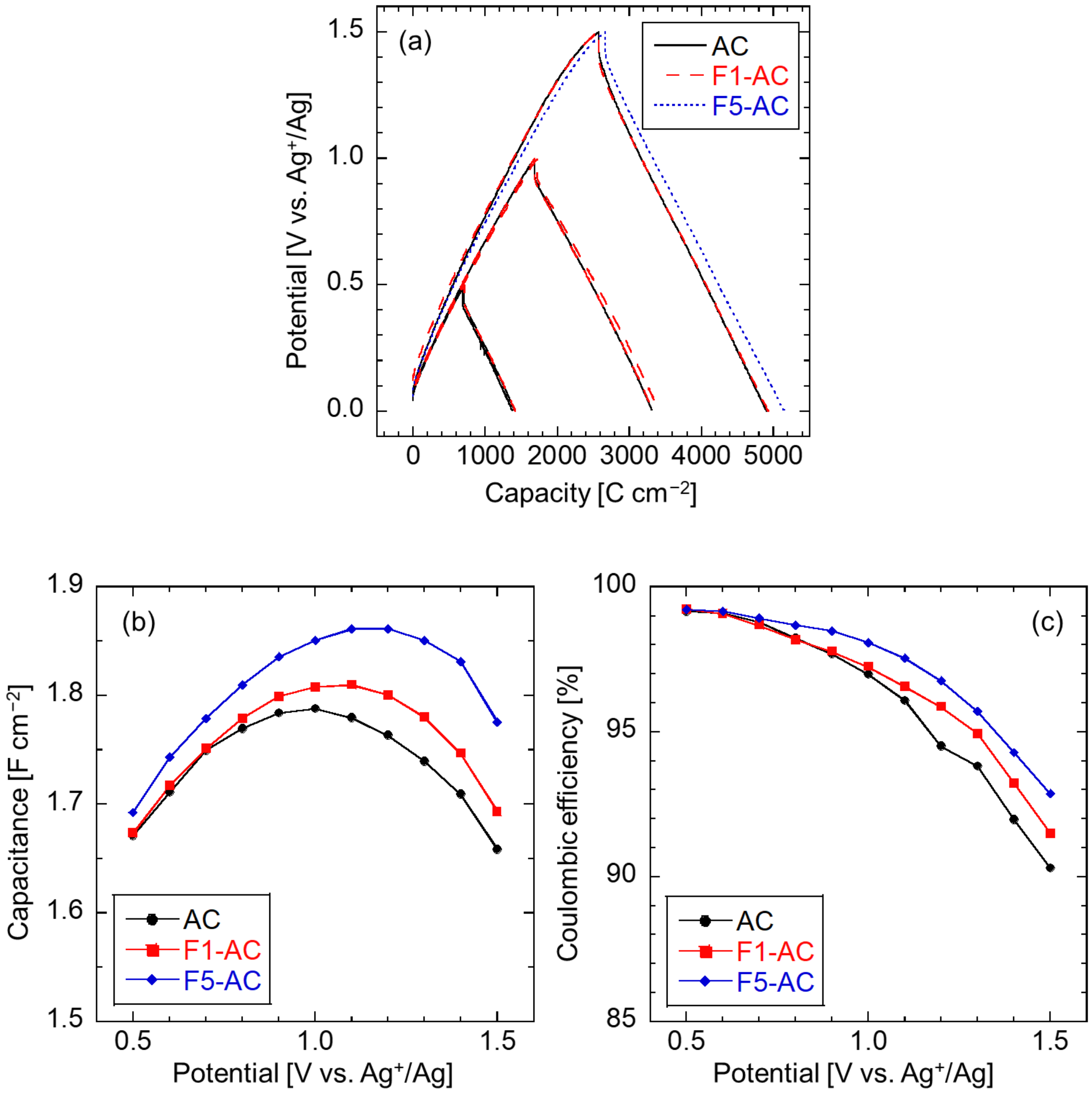

Figure 5-2 (a) Charge-discharge curves and potential dependence of (b) capacitance and (c) coulombic efficiencies for AC, F1-AC, and F5-AC at the 10th cycle in the cutoff range of 0.0-0.5 V, 0.0-1.0 V, and 0.0-1.5 V vs. Ag$^+$/Ag.

References

[1] A. Burke, *J. Power Sources*, **91** (2000) 37.

[2] R. Kötz, M. Carlen, *Electrochim. Acta*, **45** (2000) 2483.

[3] B. E. Conway, *Electrochemical Supercapacitors: Scientific Fundamentals and Technological Applications*, Kluwer Academic/Plenum Publishers, New York (1999).

[4] W. Sugimoto, H. Iwata, Y. Murakami, Y. Takasu, *J. Electrochem. Soc.*, **151** (2004) A1181.

[5] Y. Zhai, Y. Dou, D. Zhao, P. F. Fulvio, R. T. Mayes, S. Dai, *Adv. Mater.*, **23** (2011) 4828.

[6] B. Liu, H. Shioyama, T. Akita, Q. Xu, *J. Am. Chem. Soc.*, **130** (2008) 5390.

[7] F. Zhang, T. Zhang, X. Yang, L. Zhang, K. Leng, Y. Huang, Y. Chen, *Energy Environ. Sci.*, **6** (2013) 1623.

[8] D. Mochizuki, R. Tanaka, S. Makino, Y. Ayato, W. Sugimoto, *ACS Appl. Energy Mater.*, **2** (2019) 1033.

[9] L. Wei, M. Sevilla, A. B. Fuertes, R. Mokaya, G. Yushin, *Adv. Funct. Mater.*, **22** (2012) 827.

[10] O. Ioannidou, A. Zabaniotou, *Renew. Sust. Energ. Rev.*, **11** (2007) 1966.

[11] D. Cazorla-Amorós, D. Lozano-Castelló, E. Morallón, M. J. Bleda-Martínez, A. Linares-Solano, S. Shiraishi, *Carbon*, **48** (2010) 1451.

[12] D. Hulicova-Jurcakova, E. Fiset, G. Q. M. Lu, T. J. Bandosz, *ChemSusChem*, **5** (2012) 2188.

[13] D. Hulicova-Jurcakova, M. Kodama, S. Shiraishi, H. Hatori, Z. H. Zhu, G. Q. Lu, *Adv. Funct. Mater.*, **19** (2009) 1800.

[14] D. Salinas-Torres, S. Shiraishi, E. Morallón, D. Cazorla-Amorós, *Carbon*, **82** (2015) 205.

[15] M. J. Bleda-Martínez, J. A. Maciá-Agulló, D. Lozano-Castelló, E. Morallón, D. Cazorla-Amorós, A. Linares-Solano, *Carbon*, **43** (2005) 2677.

[16] O. Ornelas, J. M. Sieben, R. Ruiz-Rosas, E. Morallón, D. Cazorla-Amorós, J. Geng, N. Soin, E. Siores, B. F. G. Johnson, *Chem. Commun.*, **50** (2014) 11343.

[17] T. Kwon, H. Nishihara, H. Itoi, Q.-H. Yang, T. Kyotani, *Langmuir*, **25** (2009) 11961.

[18] M.-J. Jung, E. Jeong, S. Kim, S. I. Lee, J.-S. Yoo, Y.-S. Lee, *J. Fluorine Chem.*, **132** (2011) 1127.

[19] M.-H. Kim, J.-H. Yang, Y.-M. Kang, S.-M. Park, J. T. Han, K.-B. Kim, K. C. Roh, *Colloids Surf. A Physicochem. Eng. Asp.*, **443** (2014) 535.

[20] E. Jeong, M.-J. Jung, S. H. Cho, S. I. Lee, Y.-S. Lee, *Colloids Surf. A Physicochem. Eng. Asp.*, **377** (2011) 243.

[21] M.-J. Jung, E. Jeong, S. Cho, S. Y. Yeo, Y.-S. Lee, *J. Colloid Interface Sci.*, **381** (2012) 152.

[22] E. Jeong, M.-J. Jung, Y.-S. Lee, *J. Fluorine Chem.*, **150** (2013) 98.

[23] W. C. Smith, *Angew. Chem. Int. Ed.*, **1** (1962) 467.

[24] H. L. Poh, Z. Sofer, K. Klímová, M. Pumera, *J. Mater. Chem. C,* **2** (2014) 5198.

[25] D. T. Cronce, A. N. Mansour, R. P. Brown, B. C. Beard, *Carbon*, **35** (1997) 483.

[26] R. Winter, P. W. Cook, *J. Fluorine Chem.*, **131** (2010) 780.

Chapter 6

Binary System of Potassium Single Cation Ionic Liquid Electrolyte for Potassium-ion Batteries

6.1 Introduction

Alkali-metal ion batteries, in which alkali metal ions migrate between positive and negative electrodes, have been extensively studied due to their high voltage and capacity. Especially, lithium-ion batteries (LIBs) have been widely used and are predominant in the small electronic devices and even electronic vehicles [1, 2]. However, LIBs are expensive, and the scarcity and uneven distribution of lithium resources could limit their continuously expanding production and prevent their use in large-scale or stationary applications [3].

Demand for post-LIBs, i.e., more sustainable energy storage systems that utilize abundant elements to achieve cost-effectiveness, is increasing. Recently, potassium-ion batteries (PIBs) have attracted tremendous attention as a post-LIB due to the low cost of the widespread potassium resources (2.1 wt % in the Earth's crust) [4-8]. In addition, PIBs are expected to achieve higher voltage than LIBs as the redox potential of potassium is lower than that of lithium [9]. However, the safety issues associated with potassium metal that occur during the rapid charging or overcharging of PIBs are more profound, as potassium metal is much more reactive with oxygen and moisture than lithium metal. Thus, exploring safe battery materials with good electrochemical performance is vital for the development of PIBs.

PIBs were first studied in 2004 with a Prussian blue cathode and an organic solvent-based electrolyte composed of an organic solvent and KBF_4 [10]. In most previous studies, the design of the electrolyte for PIBs has been similar to that for LIBs. For example, potassium salts, which shuttle between electrodes, typically contain perfluoroanions such as KPF_6 and KBF_4 due to their high oxidative resistance. Electrolytes based on organic solvents [11], room-temperature ionic liquid (RTIL) containing organic cations [12, 13], and polymers have also been reported [14].

Highly concentrated electrolytes with organic solvents have attracted interest for use in alkali metal ion batteries due to their unique properties, including high oxidation resistance attributed to the more reduced solvent molecules that have no direct coulombic interactions with ions and low oxidation stability [14-23]. It is interesting to investigate how these properties change if the concentration of alkali metal ions in electrolytes are increased even further. However, according to previous works, potassium salts are less soluble in the abovementioned solvents than lithium salts, which makes investigation at high K^+ concentrations difficult [15-19].

Under this background, an IL electrolyte composed of only potassium cation as cationic species combined with counter-anions, which is referred to as “potassium-single cation ionic liquid (K-SCIL)” electrolytes, has been investigated in this chapter. A similar concept for LIBs was proposed in previous studies, targeting the improvement of lithium cation transport [24-27]. Unlike typical RTIL electrolytes or traditional high-temperature molten salts, K-SCIL electrolytes do not contain extra cationic species. Thus, the K-SCIL electrolytes can be regarded as the extreme of the highly concentrated electrolytes in terms of molar concentration of potassium salt. Moreover, similar to RTIL electrolytes, K-SCIL electrolytes have low vapor pressure and low flammability as they contain no organic solvent and thus they are attractive in practical battery applications. This chapter aims to develop PIBs using low-melting K-SCIL electrolytes, and their fundamental thermal, physicochemical properties, and electrochemical stability were investigated. Reversible charge-discharge was performed for a graphite electrode immersed in the electrolyte, confirming the feasibility of this new class of electrolyte for PIBs.

6.2 Experimental

Potassium bis(fluorosulfonyl)amide (K[FSA]; Tokyo Chemical Industry, purity > 95 %), potassium (fluorosulfonyl)(trifluorosulfonyl)amide (K[FTA]; Tokyo Chemical Industry, purity > 95%), and *N*-methyl-*N*-propylpyrrolidinium bis(fluorosulfonyl)amide ([C_3C_1pyrr][FSA]; Kanto Chemical, purity > 99.9%) were dried at 80 °C under vacuum prior to use. Mixtures of K[FSA] and K[FTA] were then prepared in a dry chamber (Daikin Industries, Ltd., HRG-50AR, dew point < −50 °C) by grinding the two powders. The $K_{0.2}[C_3C_1pyrr]_{0.8}[FSA]$ RTIL was prepared by mixing K[FSA] and [C_3C_1pyrr][FSA] in a molar ratio of 20 and 80 [12]. Electrochemical measurements were conducted using a stainless-steel cell (Hohsen Corp., HS-2) in a two-electrode configuration with the potassium metal counter (Figure 2-8). A glass separator (Nippon Sheet Glass, TGP010, thickness of 100 μm) impregnated with the K-SCIL electrolyte was used, and the cells were assembled in the glove box. Electrochemical window of the $K[FSA]_{0.55}[FTA]_{0.45}$ SCIL was determined by the cyclic voltammetry at 90 °C using an Al and a Pt plate working electrodes. Limiting current density of the $K[FSA]_{0.55}[FTA]_{0.45}$ SCIL and $K_{0.2}[C_3C_1pyrr]_{0.8}[FSA]$ RTIL was determined on an Al plate working electrode by galvanostatic polarization at 80 mA cm^{-2} at 90 ºC. Charge-discharge tests were conducted at 80 °C on a graphite electrode composed of natural graphite powder (SNO-10, SEC Carbon Ltd., mean diameter of 10 μm) and polyvinylidene fluoride (PVDF) (KUREHA) binder (graphite:PVDF = 80:20 in the weight ratio) on a Cu current collector. The graphite electrodes for XRD analyses were charged by a constant current/constant voltage mode (0.5 C (cutoff: 0.1 V) / 0.1 V (cutoff: 0.1 C) and then discharged by constant current of 0.5 C (cutoff: 2.5 V).

6.3 Results and discussion

In order to use the K-SCIL electrolytes for PIBs, lowering of melting point is preferred for handling and material availability, and mixing of two K^+ salts was examined here. Table 6-1 shows the results of the preliminary screening for the binary mixture of nine K salts (50:50 in mol). The K[FSA]-K[FTA] binary system provided the lowest melting point, owing to the property of FSA^- and FTA^- anions to give low melting points [27, 28]. Thus this system was selected for further investigation of K-SCIL for PIBs in the present study.

Figure 6-1 shows a phase diagram of the K[FSA]-K[FTA] system at intervals of 10 or 5 mol% within the low-melting range of interest (melting points of neat K[FSA] and K[FTA] are 102 and 101 °C, respectively). The solidus line was determined from the onset of the endothermic peak in the DSC continuous curve at a rate of 10 °C min^{-1} as shown in Figure 6-2 (a), and the liquidus line was determined from the smallest endothermic peak in the DSC step curve at a step of 2 °C as shown in Figure 6-2 (b). Even so it was difficult to determine the melting point precisely in this system, as the liquid phase of the mixtures was not crystallized rapidly and exhibited glass transition instead, which is similar to that often observed for some organic RTILs [29]. In addition, this system exhibited multiple thermal transitions depending on the heating and cooling cycles. The occurrence of these phenomena is attributed to the presence of some meta-stable solid phases based on the polymorphism of the perfluorosulfonylamides [30, 31]. The highest melting point, which corresponds to the melting of the most stable solid phase measured during the first heating in the DSC measurement of the prepared powder sample (Figure 6-3), is taken as the melting point and plotted in Figure 6-1. This system is a simple eutectic system, where the melting points of single salts directly reduce to the lowest melting point of 67 °C at a K[FSA]:K[FTA] molar ratio of 55:45 ($K[FSA]_{0.55}[FTA]_{0.45}$). This composition was identified as the eutectic point in this system within an experimental error of 5 mol% and regarded to be the most suitable as the K-SCIL for

PIBs that can be used near room temperature without any additional organic solvent, RTIL, and other alkali metal salt. The $K[FSA]_{0.55}[FTA]_{0.45}$ has as large a molar concentration of K^+ as 8.5 mol dm^{-3} at 90 °C owing to its characteristic of containing only K^+ as a cationic species as shown in Table 6-2.

The viscosity (η) of the $K[FSA]_{0.55}[FTA]_{0.45}$ SCIL is shown in Figure 6-4 together with those of other K-SCIL (so-called high-temperature molten salts with K^+ are also included as K-SCIL) and RTIL. Owing to the reduction of the melting point, the $K[FSA]_{0.55}[FTA]_{0.45}$ SCIL was a fluid liquid in a wider range near room temperature, which is in contrast to its constituent individual salts. Its temperature dependence follows the VTF (Vogel−Tammann−Fulcher) equation as follows, which is not similar to traditional high-temperature molten salts, but closer to RTIL electrolytes containing K[FSA] [12]:

$$\eta = A_\eta T^{1/2}\exp(B_\eta/(T\text{-}T_{0\eta})) \tag{6-1}$$

where η is the viscosity, T is the absolute temperature, A_η is a constant related to the viscosity at infinite temperature, B_η is a constant related to the activation energy, and $T_{0\eta}$ is the ideal glass-transition temperature (see Table 6-3 for the fitting parameters), which is typically lower than the glass-transition temperature (T_g), as determined by the DSC measurements.

Potassium salts, such as halides, nitrates [32], and bis(trifluoromethylsulfonyl)amide ($TFSA^-$) [9], exhibit a reasonably low viscosity of about 10^0 mPa s above 250 ºC. The K[FSA] and K[FTA] salts have a viscosity of 10^1-10^2 mPa s in the range of 110-150 ºC, and the $K[FSA]_{0.55}[FTA]_{0.45}$ SCIL exhibits a viscosity between them. The $K[FSA]_{0.55}[FTA]_{0.45}$ SCIL is more viscous when it is used near its eutectic temperature (10^3 mPa s), similar to highly concentrated organic electrolytes [23]. The higher viscosity of the $K[FSA]_{0.55}[FTA]_{0.45}$ SCIL is observed compared to that of the $K_{0.2}[C_3C_1pyrr]_{0.8}[FSA]$ RTIL, which results from the increased cation-anion Coulombic interaction based on the small K^+. Among these anions, salts with larger anions exhibit higher viscosity within the same temperature range, as the long fluoroalkyl chains lead to van der Waals interactions as well as coulombic interactions between cations and anions. The viscous nature of the $K[FSA]_{0.55}[FTA]_{0.45}$ SCIL could affect its impregnation behavior for the separator and composite electrode.

Ionic conductivity (σ), or more precisely speaking, molar ionic conductivity, is inversely related to viscosity. The ionic conductivity of the $K[FSA]_{0.55}[FTA]_{0.45}$ SCIL was fitted by the VTF equation as follows:

$$\sigma = A_\sigma T^{-1/2}\exp(-B_\sigma/(T-T_{0\sigma})) \qquad (6\text{-}2)$$

where A_σ is a constant related to the ionic conductivity at infinite temperature, B_σ is a constant related to the activation energy, and $T_{0\sigma}$ is the ideal glass-transition temperature (see Table 6-3 for the fitting parameters). In general, organic electrolytes used in current batteries have ionic conductivities of 10^1-10^2 mS cm^{-1}. As shown in Figure 6-5, the high-temperature molten potassium salts have higher ionic conductivities than those of perfluorosulfonylamide ILs, which mainly results from the difference in temperature range. The $K[FSA]_{0.55}[FTA]_{0.45}$ SCIL exhibited ionic conductivities less than 10^2 mS cm^{-1} which are lower than those of typical RTIL electrolytes including $K_{0.2}[C_3C_1pyrr]_{0.8}[FSA]$ [12]. On the other hand, a unique transport property of K-SCIL can be found according to the following Walden (or fractional Walden) rule [33-37]:

$$\eta\,\lambda = \text{const. (or } \eta\,\lambda^{\alpha} = \text{const.)} \qquad (6\text{-}3)$$

where λ is molar ionic conductivity and α is the decoupling constant. The λ is calculated by the following equation,

$$\lambda = \sigma\,(\mathrm{MW})/\rho \tag{6-4}$$

where MW is the molar weight and ρ is the density of the electrolyte. Figure 6-6 shows the Walden plots of the K[FSA]$_{0.55}$[FTA]$_{0.45}$ SCIL together with other electrolytes showing the relation of the logarithmic reciprocal molar conductivities against their logarithmic viscosities. A highly dissociated state is proposed for most of the K-SCILs as their conductivities are close to the ideal value predicted by their viscosity (dashed line in Figure 6-6). Especially, those for the K[FSA]$_{0.55}$[FTA]$_{0.45}$ SCIL are above the dashed line. However, K$_{0.2}$[C$_3$C$_1$pyrr]$_{0.8}$[FSA] RTIL exhibits a relatively low conductivity in spite of its low viscosity. It indicates that the K[FSA]$_{0.55}$[FTA]$_{0.45}$ SCIL possesses high conductivity despite its viscous nature, which differs from the properties of previously explored RTILs. The high viscosity is attributed to the electrostatic interaction caused by highly concentrated K^+.

The ionic conductivity described above is generated by all ions in the K[FSA]$_{0.55}$[FTA]$_{0.45}$ SCIL, i.e., K^+, FSA^- and FTA^-. As electrolytes for PIBs, the partial conductivity of K^+ in the K-SCIL is the most important parameter because it restricts the rate capability of the target battery. The current limited by the K^+ partial conductivity (limiting current) in PIBs is defined by the parameters of the electrolyte and electrochemical cell based on the following equation [8, 36]:

$$I_L^C = 4FDc/Ad \tag{6-5}$$

where I_L^C is the calculated limiting current density (C denotes value), F is the Faraday constant, D is the diffusion coefficient of K^+, c is the concentration of K^+, A is the area of the working electrode, and d is the distance between the working and counter electrodes. In this study, D is not measured directly; however, its maximum value (D^{C}) can be estimated from the viscosity using the Stokes-Einstein equation:

$$D^{\mathrm{C}} = kT/\pi ar\eta \tag{6-6}$$

where k is the Boltzmann constant, r is the hydrodynamic radius of an ion-dominating viscosity, and a is a theoretical constant that was empirically obtained between 4 to 6 for the slip and stick boundary conditions, respectively. Table 6-2 summarizes these parameters for the K-SCIL and RTIL electrolytes in our electrochemical cell. The parameters, r and a, were assumed to be the smallest values for obtaining D^{C}, and therefore, the maximum $I_{\mathrm{L}}^{\mathrm{C}}$ (r = 0.165 nm as the ionic radius of K^+ and a = 4 as the slip condition) [38]. The $I_{\mathrm{L}}^{\mathrm{C}}$ of the $\mathrm{K[FSA]_{0.55}[FTA]_{0.45}}$ SCIL electrolyte is lower than that of the $\mathrm{K_{0.2}[C_3C_1pyrr]_{0.8}[FSA]}$ RTIL electrolyte, which is mainly due to the higher viscosity. However, as shown in Figure 6-7, the cell voltage for the $\mathrm{K_{0.2}[C_3C_1pyrr]_{0.8}[FSA]}$ RTIL electrolyte declined rapidly when applying excess current beyond $I_{\mathrm{L}}^{\mathrm{C}}$. This indicates that the diffusion of K^+ reached its limit due to the concentration gradient; therefore, there was no K^+ near the working electrode, and the current was then consumed by the decomposition of the organic cation of the RTIL, rather than deposition of potassium metal. However, the $\mathrm{K[FSA]_{0.55}[FTA]_{0.45}}$ SCIL achieved a steady cell voltage under the same conditions, despite its larger overpotential than the RTIL electrolyte. This indicates that a concentration gradient did not occur in the $\mathrm{K[FSA]_{0.55}[FTA]_{0.45}}$ SCIL system, and the concentration of K^+ should be maintained throughout the electrolyte due to the electroneutrality. Although the measurement of the K^+ ion transference number provides important information on the present transport phenomenon, the large interfacial resistance leads to the difficulty its estimation by potentiostatic polarization or very low frequency impedance techniques. Further improvement in analytical techniques is required on this matter.

The electrochemical window, which is defined by the limit potentials of the cathode and anode, is one of the main features determining the compatibility of electrode materials. As shown in Figure 6-8, the cathode and anode limits of the $K[FSA]_{0.55}[FTA]_{0.45}$ SCIL were measured by cyclic voltammetry in the two-electrode cell with an aluminum or a platinum working electrode, respectively. The cathode limit was 0 V vs. K/K^+, which corresponds to the reversible deposition and dissolution of potassium metal. The coulombic efficiency was 60 %, which could be attributed to the decomposition of the anions or the elimination of the deposited potassium metal from the working electrode at 90 ºC above the melting point of potassium metal (63.5 ºC). The anode limit, which was determined when the current density exceeded 0.4 mA cm^{-2}, was 5.6 V vs. K/K^+. This reaction is the oxidative decomposition of FSA^- and/or FTA^- anions.

Figure 6-9 shows the charge-discharge curves of the graphite electrode in the $K[FSA]_{0.55}[FTA]_{0.45}$ SCIL electrolyte at 80 °C. The infrequent spikes are likely due to the insufficient contact of the liquid potassium counter electrode to the current collector. The electrode was charged at a constant current (CC) of 0.3 C below the cut-off voltage of 2.5-0.1 V and constant voltage (CV) at 0.1 V for cycles, and was discharged at a constant current of 0.3 C. The first charge capacity was 640 mAh g^{-1}, while the theoretical capacity was 279 mAh g^{-1} corresponding to the formation of KC_8. This high capacity was derived from the decomposition of FSA^- or FTA^- to form a solid electrolyte interphase (SEI) film. From the second cycle, the charge capacity decreased as the number of cycles increased, and reached 254 mAh g^{-1} at the 50th cycle (Figure 6-10). However, the discharge capacity of the first cycle was 273 mAh g^{-1}, which was mostly consistent with the theoretical capacity (over 97%). The discharge capacity also gradually decreased as the number of cycles increased, and reached

230 mAh g^{-1} at the 50th cycle. This gradual decrease is due to the degradation of the graphite composite electrode, which may be caused by the thermal brittleness of the PVDF binder. The coulombic efficiency of K^+ intercalation/deintercalation is approximately 90 % after the 50th cycle. The 10 % irreversibility indicates that the FSA^- or FTA^- were continuously decomposed on the electrode at 80 °C. Instability of SEI can cause this irreversibility, and further study on constituent ion or effective additive is required to improve it.

Figure 6-11 shows the *ex-situ* XRD patterns of the graphite electrodes before charging, and after the first charge and discharge. After charging, the peak at 26.62° corresponding to the 002 diffraction of the pristine graphite disappeared, and new peaks appeared at 16.57° and 33.55°, corresponding to d = 5.35 and 2.67 Å, respectively. These peaks can be indexed as 001 and 002 respectively, which provides the interlayer distance of 5.35 Å and the formation of stage-1 potassium-graphite intercalation compounds (K-GICs), although the peaks may be indexed as 004 and 008, respectively, by considering the interlayer arrangements of K^+ as discussed in previous works [39, 40]. The formation of stage-1 K-GIC (≈ KC_8) was also consistent with its brown-colored appearance after the first charge [15, 41]. The intercalation of K^+ proceeded fully along with the disappearance of the peak ascribed to stage-2 K-GIC (around 20.5° and 30.1°) [15, 42]. The weak peak intensity of the charged sample was due to the electrolyte remaining on the electrode without rinsing. The electrode rinsing process, which is typically executed before *ex-situ* measurements to remove the electrolyte, may affect the GIC electrode chemistry [43, 44]. After discharge, these peaks disappeared and the 002 diffraction peak of graphite recovered at 26.49° which is almost the same angle as that before charging. This indicates that the intercalation and deintercalation of K^+ to graphite proceeded reversibly.

6.4 Conclusions

In this chapter, the binary system of K-SCIL composed of K[FSA] and K[FTA] was investigated for PIBs. The melting point of the K[FSA] and K[FTA] mixture was reduced to 67 ºC at the composition of $K[FSA]_{0.55}[FTA]_{0.45}$. The transport properties of this electrolyte were poor when compared to those of room temperature electrolytes containing an organic solvent or RTIL; however, it achieved superionic conductance at elevated temperature under the current larger than the diffusion-limited current density due to the absence of a concentration gradient for K^+. The large electrochemical window of over 5 V for this system is beneficial for application in PIBs. The graphite negative electrode exhibited stable charge and discharge behavior in this K-SCIL, with a discharge capacity near the theoretical value for the formation of the stage-1 K-GIC. The K^+ intercalation/deintercalation into/from graphite were confirmed by *ex-situ* XRD measurements. The thermal and transport properties of the K-SCIL could be improved by the addition of a third potassium salt.

Table 6-1 Melting points (T_m) of various mixtures of two different K salts in a molar ratio of 50 : 50 determined by DSC measurements.

Salt 1	Salt 2	Salt 1 T_m [°C]	Salt 2 T_m [°C]	Mixture T_m [°C]
K[FSA]	K[FTA]	102	101	67
	K[TfO]		238	80
	K[CF_3BF_3]		312*	85
	K[TFSA]		198	95
K[FTA]	K[TfO]	101	238	78
	K[TFSA]		198	90
K[TFSA]	K[TfO]	198	238	150
	K[CF_3BF_3]		312*	170
K[TfO]	K[CF_3BF_3]	238	312*	180

* Decomposition temperature

※ No effects to reduce melting point was observed by addition of KF, KBF_4, KSCN, and $KN(CN)_2$ to K[FSA] or K[FTA].

Table 6-2 Concentration of shuttle ions, viscosity, and calculated diffusion coefficient and limiting current density for $K_{0.2}[C_3C_1pyrr]_{0.8}[FSA]$ and $K[FSA]_{0.55}[FTA]_{0.45}$ ILs at 90 ºC.

Electrolyte	C [mol dm^{-3}]	η [mPa s]	$D^{C\ b}$ [10^{-10} m^2 s^{-1}]	$I_L^{C\ b}$ [mA cm^{-2}]
$K_{0.2}[C_3C_1pyrr]_{0.8}[FSA]$	0.94[a]	12.5[a]	1.93	29.1
$K[FSA]_{0.55}[FTA]_{0.45}$	8.5	334	0.0724	8.9

[a] These values were obtained from a previous work [12].

[b] I_L^C and D^C were calculated by Eqs. (6-5) and (6-6) assuming A = 0.126 cm^2 and d = 0.2 cm.

Table 6-3 Parameters of VTF fitting for viscosity and ionic conductivity of K[FSA]$_{0.55}$[FTA]$_{0.45}$.

Viscosity			Ionic conductivity		
A_η [mPa s K$^{-0.5}$]	B_η [K]	$T_{0\eta}$ [K]	A_σ [mS cm^{-1} K$^{0.5}$]	B_σ [K]	$T_{0\sigma}$ [K]
4.04×10^{-3}	1.09×10^{3}	2.35×10^{2}	3.80×10^{4}	6.82×10^{2}	2.53×10^{2}
Coefficient of determination: $R^2 = 0.9995$			Coefficient of determination: $R^2 = 0.99997$		

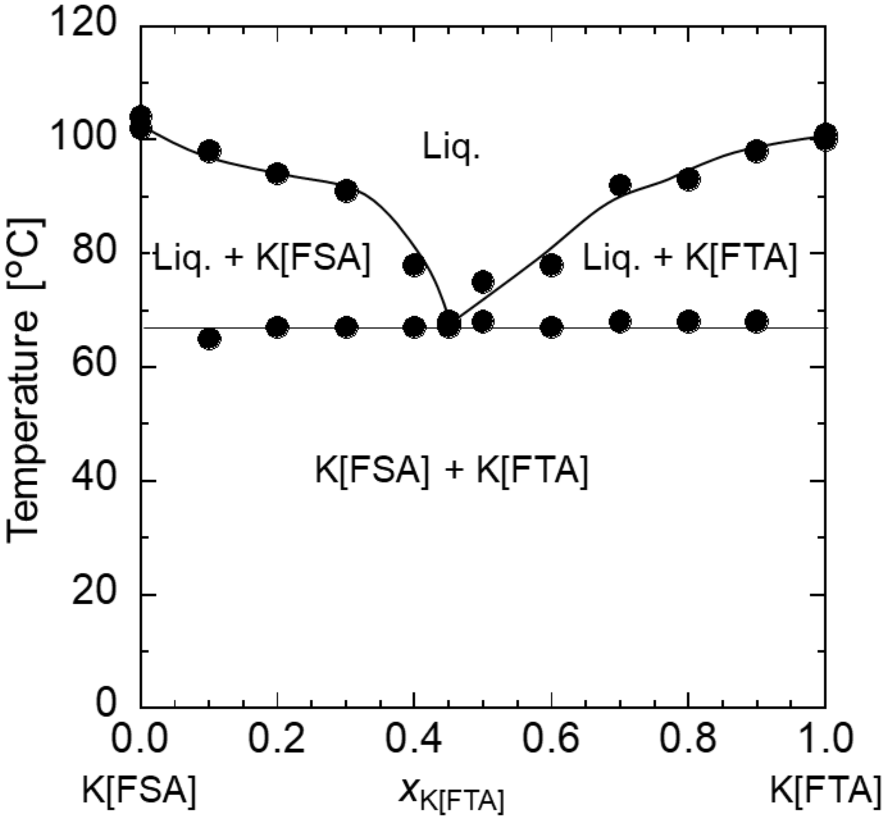

Figure 6-1 Phase diagram of the K[FSA]-K[FTA] binary system determined by DSC analysis. The abbreviations Liq. and $X_{K[FTA]}$ denote the liquid phase and molar ratio of K[FTA] in this system.

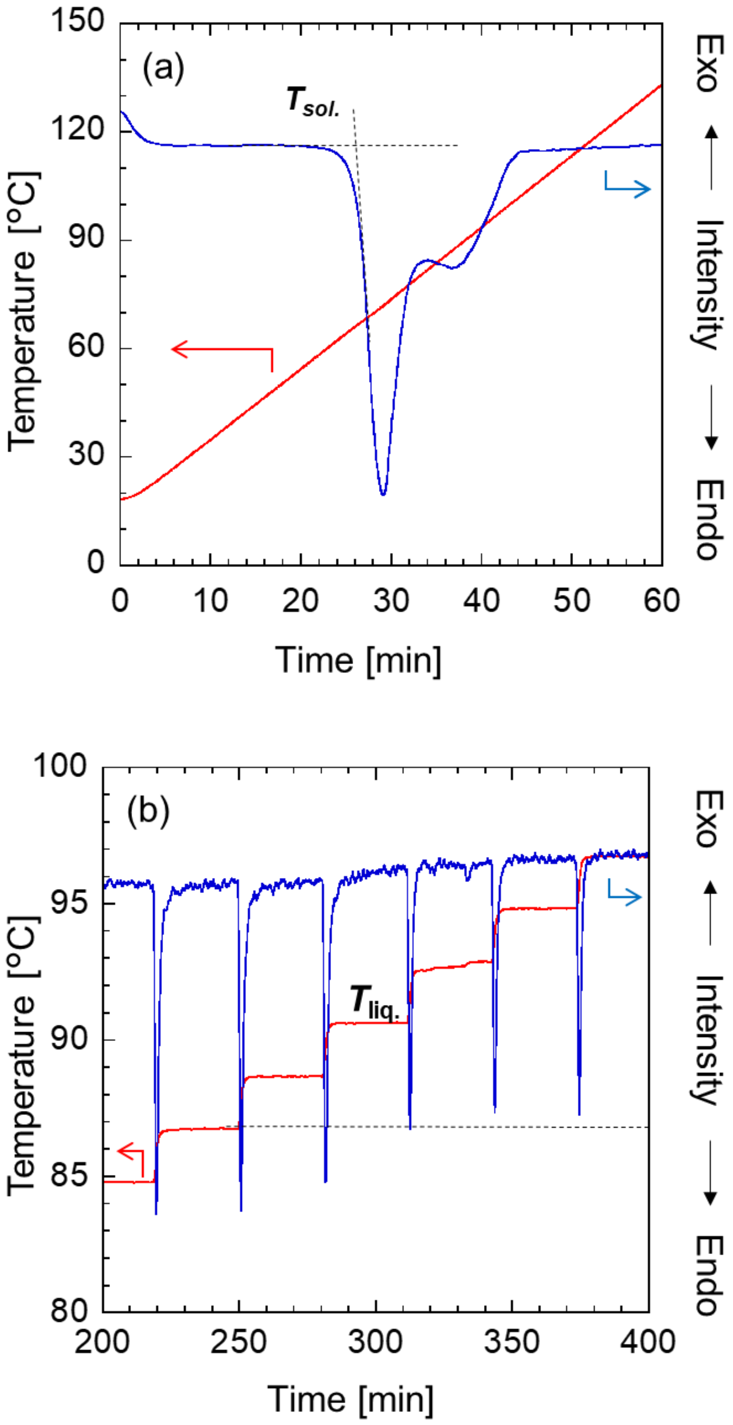

Figure 6-2 DSC curves for $K[FSA]_{0.7}[FTA]_{0.3}$ by (a) continuous heating at the rate of 10 ºC min^{-1} to determine solidus temperature ($T_{sol.}$) and (b) step heating at the interval of 2 ºC for 30 minutes to determine liquidus temperature ($T_{liq.}$).

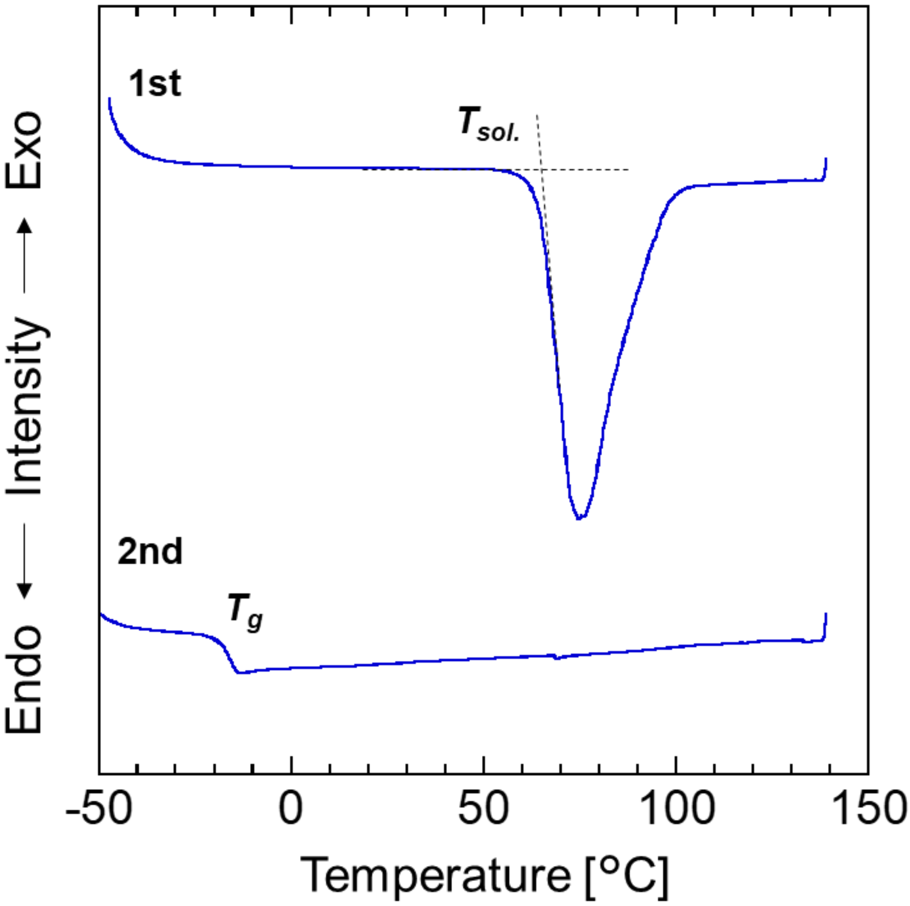

Figure 6-3 DSC curves of K[FSA]$_{0.55}$[FTA]$_{0.45}$ by continuous heating at the rate of 10 °C min^{-1} in the first heating of powder sample and second heating of melted sample to determine solidus temperature ($T_{sol.}$) and glass transition temperature (T_g).

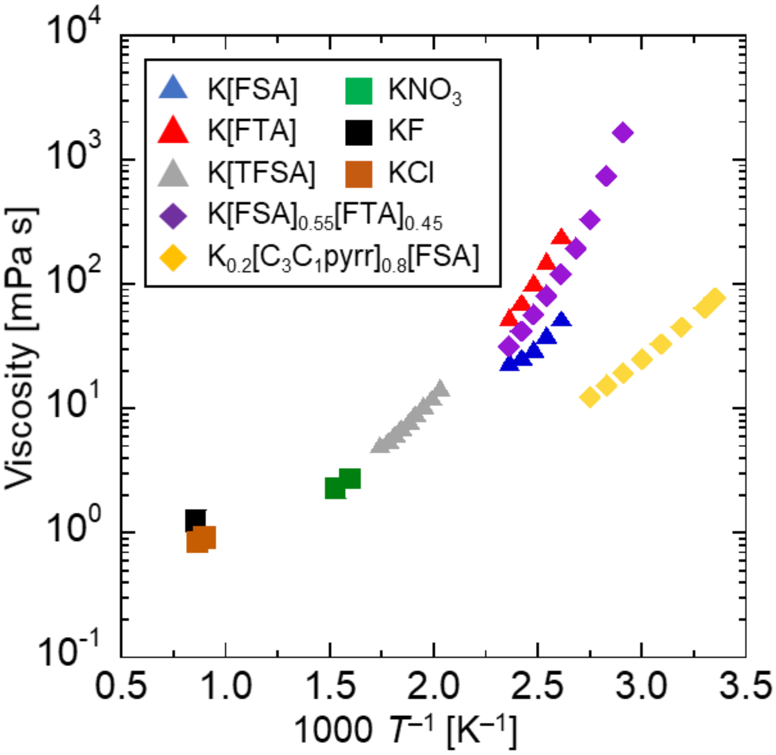

Figure 6-4 Temperature dependence of viscosity for some K-SCILs and RTIL (see references for KNO_3, KF, KCl, and $K_{0.2}[C_3C_1pyrr]_{0.8}[FSA]$) [12, 32].

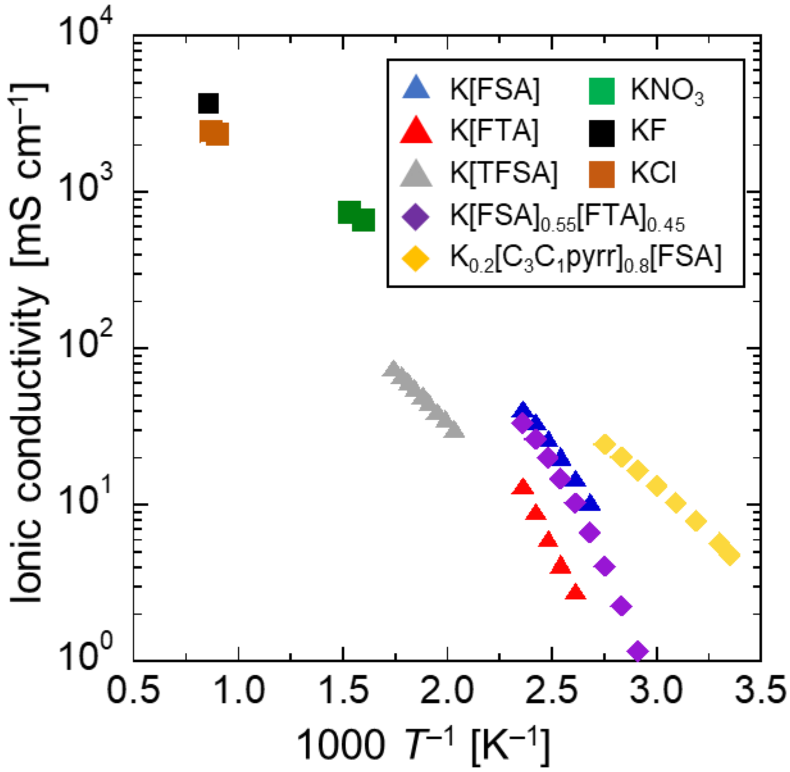

Figure 6-5 Temperature dependence of ionic conductivity for some K-SCILs and RTIL (see references for KNO_3, KF, KCl, and $K_{0.2}[C_3C_1pyrr]_{0.8}[FSA]$) [12, 32].

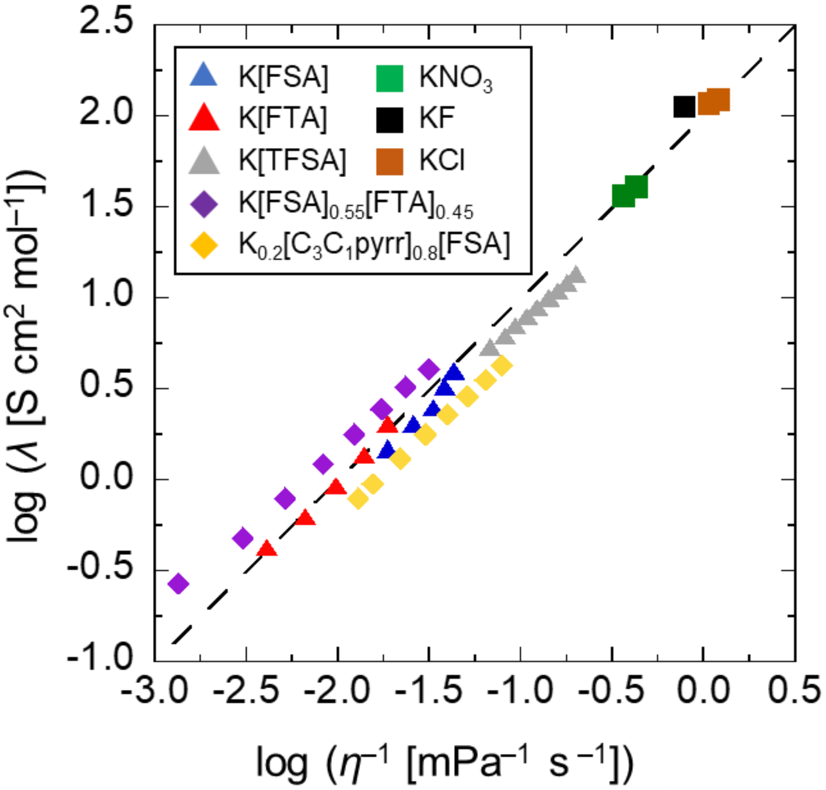

Figure 6-6 Walden plot for some K-SCILs and RTIL (see references for KNO_3, KF, KCl, and $K_{0.2}[C_3C_1pyrr]_{0.8}[FSA]$) [12, 32].

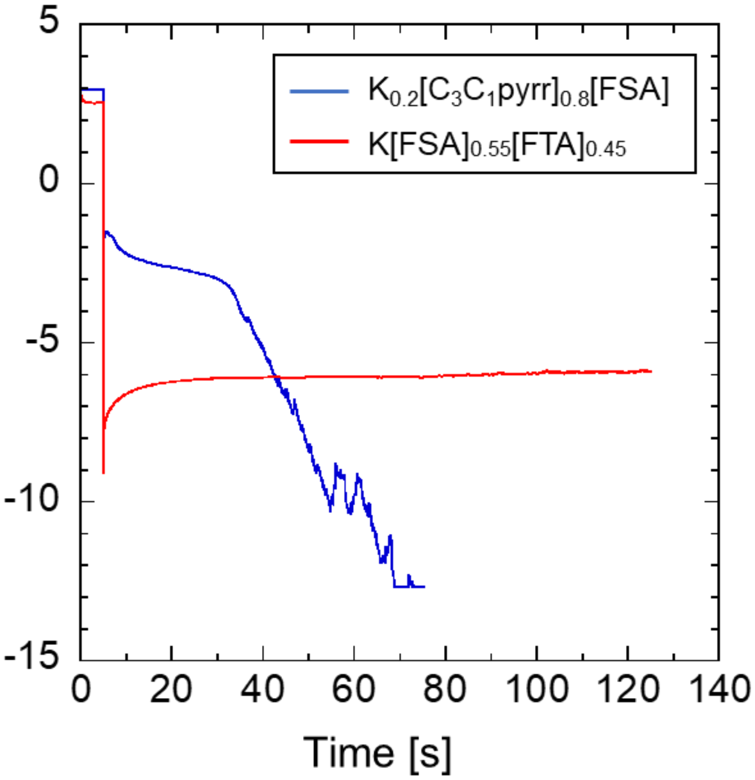

Figure 6-7 Time-voltage profile of the K||Al cell during galvanostatic K metal deposition on the Al substrate at a constant current of 80 mA cm^{-2} at 90 ºC.

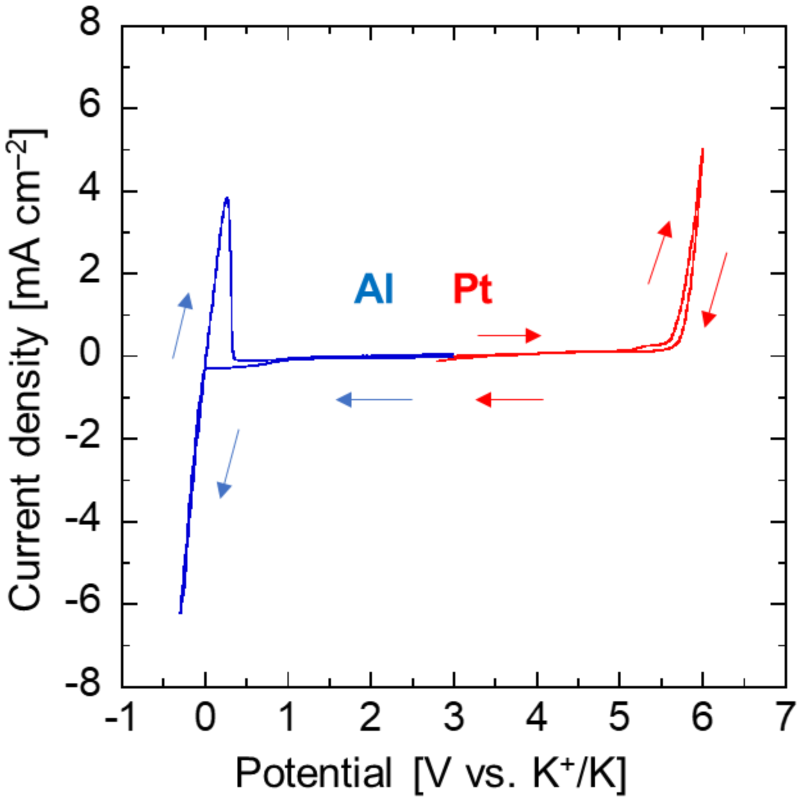

Figure 6-8 Combined cyclic voltammogram of the K[FSA]$_{0.55}$[FTA]$_{0.45}$ SCIL at a scan rate of 10 mV s^{-1} and 90 ºC.

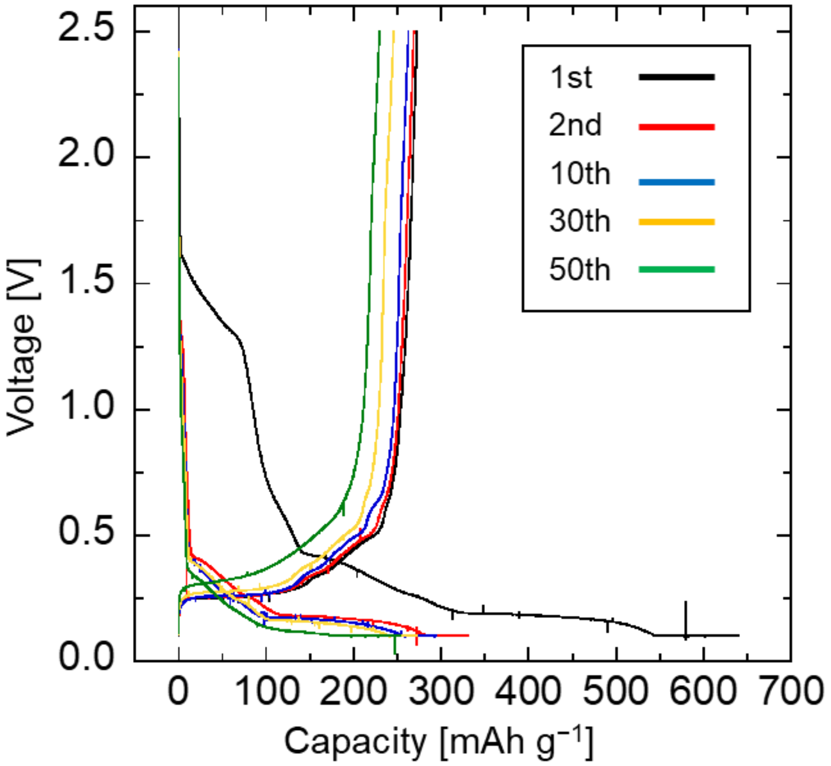

Figure 6-9 Charge-discharge curves of the K||graphite cell using the K[FSA]$_{0.55}$[FTA]$_{0.45}$ SCIL at a charge/discharge rate of 0.3 C and 80 ºC.

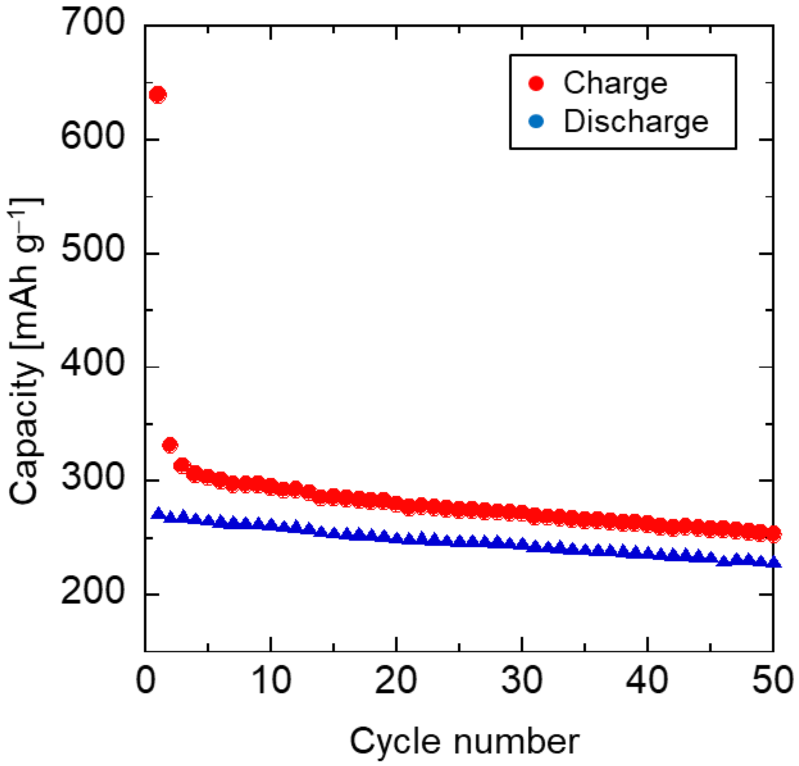

Figure 6-10 Charge and discharge capacities of the K||graphite cell using the K[FSA]$_{0.55}$[FTA]$_{0.45}$ SCIL at the rate of 0.3 C at 80 ºC.

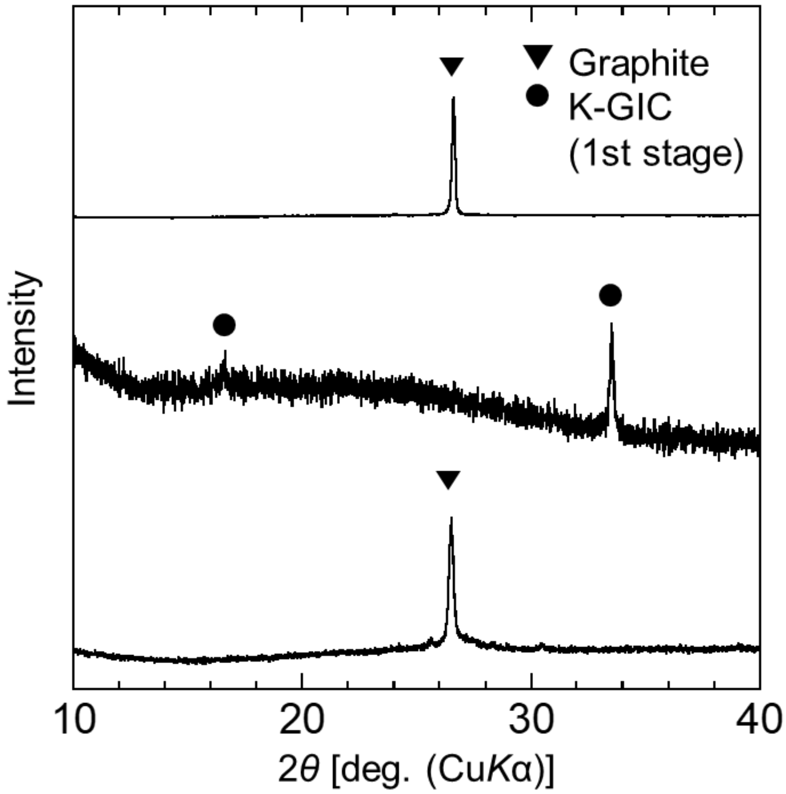

Figure 6-11 XRD patterns of the graphite electrodes. (a) Before charging, (b) after charge, and (c) after discharge in the K[FSA]$_{0.55}$[FTA]$_{0.45}$ SCIL. Charge condition: constant current/constant voltage mode (0.5 C (cutoff: 0.1 V) / 0.1 V (cutoff: 0.1 C). Discharge condition: constant current of 0.5 C (cutoff: 2.5 V).

References

[1] J.-M. Tarascon, M. Armand, *Materials for Sustainable Energy*, (2010) 171.

[2] P. V. Braun, J. Cho, J. H. Pikul, W. P. King, H. Zhang, *Curr. Opin. Solid State Mater. Sci.*, **16** (2012) 186.

[3] J.-M. Tarascon, *Nat. Chem.*, **2** (2010) 510.

[4] J.-Y. Hwang, S.-T. Myung, Y.-K. Sun, *Adv. Funct. Mater.*, **28** (2018) 1802938.

[5] L. Xue, S. V. Savilov, V. V. Lunin, H. Xia, *Adv. Funct. Mater.*, **28** (2018) 1705836.

[6] Z. Yao, X. Xia, D. Xie, Y. Wang, C.-a. Zhou, S. Liu, S. Deng, X. Wang, J. Tu, *Adv. Funct. Mater.*, **28** (2018) 1802756.

[7] G. Zeng, Y. An, H. Fei, T. Yuan, S. Qing, L. Ci, S. Xiong, J. Feng, *Funct. Mater. Lett.*, **11** (2018) 1840003.

[8] P. G. Bruce, C. A. Vincent, *J. Electroanal.l Chem. Interf. Electrochem.*, **225** (1987) 1.

[9] K. Kubota, K. Tamaki, T. Nohira, T. Goto, R. Hagiwara, *Electrochim. Acta*, **55** (2010) 1113.

[10] A. Eftekhari, *J. Power Sources*, **126** (2004) 221.

[11] G. Zeng, S. Xiong, Y. Qian, L. Ci, J. Feng, *J. Electrochem. Soc.*, **166** (2019) A1217.

[12] T. Yamamoto, K. Matsumoto, R. Hagiwara, T. Nohira, *J. Phys. Chem. C*, **121** (2017) 18450.

[13] T. Masese, K. Yoshii, Y. Yamaguchi, T. Okumura, Z.-D. Huang, M. Kato, K. Kubota, J. Furutani, Y. Orikasa, H. Senoh, H. Sakaebe, M. Shikano, *Nat. Commun.*, **9** (2018) 3823.

[14] H. Fei, Y. Liu, Y. An, X. Xu, G. Zeng, Y. Tian, L. Ci, B. Xi, S. Xiong, J. Feng, *J. Power Sources*, **399** (2018) 294.

[15] S. Komaba, T. Hasegawa, M. Dahbi, K. Kubota, *Electrochem. Commun.*, **60** (2015) 172.

[16] M. Okoshi, Y. Yamada, S. Komaba, A. Yamada, H. Nakai, *J. Electrochem. Soc.*, **164**

(2016) A54.

[17] K. Kubota, M. Dahbi, T. Hosaka, S. Kumakura, S. Komaba, *Chem. Rec.*, **18** (2018) 459.

[18] M. Morita, T. Shibata, N. Yoshimoto, M. Ishikawa, *Electrochim. Acta*, **47** (2002) 2787.

[19] X. Bie, K. Kubota, T. Hosaka, K. Chihara, S. Komaba, *J. Mater. Chem. A*, **5** (2017) 4325.

[20] K. Yoshida, M. Nakamura, Y. Kazue, N. Tachikawa, S. Tsuzuki, S. Seki, K. Dokko, M. Watanabe, *J. Am. Chem. Soc.*, **133** (2011) 13121.

[21] L. Suo, O. Borodin, T. Gao, M. Olguin, J. Ho, X. Fan, C. Luo, C. Wang, K. Xu, *Science*, **350** (2015) 938.

[22] K. Matsumoto, K. Inoue, K. Nakahara, R. Yuge, T. Noguchi, K. Utsugi, *J. Power Sources*, **231** (2013) 234.

[23] T. Hosaka, K. Kubota, H. Kojima, S. Komaba, *Chem. Commun.*, **54** (2018) 8387.

[24] H. Shobukawa, H. Tokuda, S.-I. Tabata, M. Watanabe, *Electrochim. Acta*, **50** (2004) 305.

[25] R. Tao, D. Miyamoto, T. Aoki, T. Fujinami, *J. Power Sources*, **135** (2004) 267.

[26] K. Kubota, H. Matsumoto, *J. Phys. Chem. C*, **117** (2013) 18829.

[27] M. Beran, J. Příhoda, Z. Žák, M. Černík, *Polyhedron*, **25** (2006) 1292.

[28] K. Kubota, T. Nohira, R. Hagiwara, M. Hajime, *Chem. Lett.*, **39** (2010) 1303.

[29] T. Mukai, K. Nishikawa, *Solid State Sci.*, **12** (2010) 783.

[30] K. Matsumoto, T. Oka, T. Nohira, R. Hagiwara, *Inorg. Chem.*, **52** (2013) 568.

[31] K. Kubota, H. Matsumoto, *Chem. Lett.*, **40** (2011) 1105.

[32] G. J. Janz, *Thermodynamic and transport properties for molten salts : correlation equations for critically evaluated density, surface tension, electrical conductance, and viscosity data*, the American Chemical Society and the American Institute of Physics for the National Bureau of Standards, New York (1988).

[33] W. Xu, E. I. Cooper, C. A. Angell, *J. Phys. Chem. B*, **107** (2003) 6170.

[34] H. U. P. Walden, G. Busch, *Z. Phys. Chem.*, **123** (1926) 429.

[35] M. Yoshizawa, W. Xu, C. A. Angell, *J. Am. Chem. Soc.*, **125** (2003) 15411.

[36] J.-W. Park, K. Yoshida, N. Tachikawa, K. Dokko, M. Watanabe, *J. Power Sources*, **196** (2011) 2264.

[37] K. R. Harris, *J. Phys. Chem. B*, **114** (2010) 9572.

[38] C. T. P. R. D. Shannon, *Acta Crystallogr.*, **B25** (1969) 925.

[39] W. Rüdorff, E. Schulze, *Z. Anorg. Allg. Chem.*, **277** (1954) 156.

[40] Z. Wang, S. M. Selbach, T. Grande, *RSC Adv.*, **4** (2014) 4069.

[41] J. Zhao, X. Zou, Y. Zhu, Y. Xu, C. Wang, *Adv. Funct. Mater.*, **26** (2016) 8103.

[42] W. Luo, J. Wan, B. Ozdemir, W. Bao, Y. Chen, J. Dai, H. Lin, Y. Xu, F. Gu, V. Barone, L. Hu, *Nano Lett.*, **15** (2015) 7671.

[43] J. Jegoudez, C. Mazieres, R. Setton, *Synth. Met.*, **7** (1983) 85.

[44] G. A. Elia, I. Hasa, G. Greco, T. Diemant, K. Marquardt, K. Hoeppner, R. J. Behm, A. Hoell, S. Passerini, R. Hahn, *J. Mater. Chem. A*, **5** (2017) 9682.

Chapter 7

Ternary System of Potassium Single Cation Ionic Liquid Electrolyte for Potassium-ion Batteries

7.1 Introduction

As described in Chapter 6, ionic liquids (ILs) are promising candidates for PIB electrolytes because of their low flammability, volatility, high thermal stability and wide electrochemical window [1-6]. Several studies have confirmed highly reversible K^+ insertion/desertion in ionic liquid electrolytes [7-9]. For instance, hard carbon with 0.5 mol dm^{-3} K[TFSA]-[C_4C_1pyrr][TFSA] ($C_4C_1pyrr^+$ = *N*-butyl-*N*-methylpyrrolidinium and $TFSA^-$ = bis(trifluoromethanesulfonyl)amide) showed stable capacity behavior for 100 cycles [10]. In another report, Sn powder demonstrated high cycleability (~93% capacity retention after 100 cycles) in 1 mol dm^{-3} K[FSA]-[C_3C_1pyrr][FSA] ($C_3C_1pyrr^+$ = *N*-propyl-*N*-methylpyrrolidinium and FSA^- = bis(fluoromethanesulfonyl)amide) [11]. These studies employed moderate concentrations of K^+ ions in the electrolyte but higher concentration may lead to high rate capability. Ionic liquids electrolytes with high K^+ concentration can be achieved by preparing electrolytes consisting of only K^+ as cationic species. In Chapter 6, potassium single cation ionic liquid (K-SCIL) of the binary system of K[FSA]-K[FTA] (FTA^- = (fluorosulfonyl)(trifluorosulfonyl)amide) was investigated as an electrolyte with an extremely high concentration of K^+ (8.5 mol dm^{-3} at 90 °C) for PIBs. The eutectic point at 55 : 45 in a molar ratio of K[FSA] : K[FTA] showed a comparatively low melting point of 67 °C compared with single K[FSA] and K[FTA] (102 and 101 °C). One of the most remarkable characteristics of the binary K-SCIL of $K[FSA]_{0.55}[FTA]_{0.45}$ is the behavior under a huge current over the diffusion-limited current density calculated based on physicochemical properties of the electrolyte, where stable K metal deposition was demonstrated owing to its characteristic of containing only K^+ as a cationic species without K^+ concentration gradient in contrast that electrolyte decomposition occurred for $K_{0.2}[C_3C_1pyrr]_{0.8}[FSA]$ RTIL (RTIL: room temperature ionic liquid). In addition, the $K[FSA]_{0.55}[FTA]_{0.45}$ SCIL showed a high ionic conductivity at elevated temperature, a wide electrochemical window of 5 V, and a reversible potassium intercalation/deintercalation into/from graphite. However, the melting point of 67 °C is still high for conventional applications and is also over the melting point of K metal (63.5 °C) which is problematic for safety concerns and difficulty in handling. Pursuing this concept, addition of the third potassium salt is expected to further lower the melting point. In a previous report, the electrochemical and physicochemical properties of single anion inorganic ionic liquids were investigated; the eutectic mixture of Li[FSA]-K[FSA]-Cs[FSA] in a 30 : 35: 45 molar ratio exhibited a wide electrochemical window of 5.4 V and a melting point of 50 °C [12]. However, there are no reports for the ternary mixture of SCIL so far for any battery system. Therefore, the ternary mixture of K-SCIL is an interesting case to investigate and expected to provide a low melting point and a high transference number of K^+ ion.

In this chapter, K-SCIL by the ternary system of K[FSA]-K[FTA]-K[TfO] (TfO^- = trifluoromethylsulfonate) was investigated. Out of various K salts, K[TfO] is considered to be the most promising according to the preliminary screening for the binary mixture of nine K salts (50:50 in mol) (Table 6-1). The fundamental thermal, electrochemical, and physicochemical properties are described, and a graphite negative electrode was employed for its application for PIBs.

7.2 Experimental

The reagents of K[FSA] (Tokyo Chemical Industry, purity > 95.0 %), K[FTA] (Tokyo

Chemical Industry, purity > 95.0 %), and K[TfO] (Tokyo Chemical Industry, purity > 98.0 %) were dried at 80 °C under vacuum for 1 day prior to use. Propylene carbonate (PC, Kishida Chemical Co., Ltd., purity > 99.5 %) was used as purchased. The mixture of K[FSA], K[FTA], and K[TfO] was prepared by mixing and grinding them. The organic electrolyte of 1 M $K[FSA]_{0.33}[FTA]_{0.33}[TfO]_{0.33}$ in PC was prepared by dissolving the designated amount of the salt in PC by stirring for a few hours.

Electrochemical performances of the electrolytes were measured using the 2032-type coin cells at 55 °C shown in Figure 2-9. Electrochemical window of the electrolytes was determined by cyclic voltammetry at the scan rate of 10 mV s^{-1} using Al and Pt foil electrodes. Limiting current density of the electrolytes was measured by galvanostatic polarization at various constant current densities. Dissolution-deposition behavior of K metal were investigated on an Al foil electrode in the electrolytes. Initially, some electrolytes were decomposed to decrease the involvement of the electrolyte decomposition to dissolution-deposition tests by applying the current of −0.1 mA cm^{-2} for 1000 s (for electrolyte decomposition and some K metal deposition) and the current of +0.1 mA cm^{-2} until the cell voltage reached 1.0 V (for consuming the deposited K metal). After this treatment, K metal was deposited by the current of −0.1 mA cm^{-2} for 1000 s and K metal dissolution-deposition was repeated by the current of +0.1 mA cm^{-2} for 200 s and the current of −0.1 mA cm^{-2} for 200 s until the cell voltage reached 1.0 V.

Charge-discharge tests and cyclic voltammetry were performed for a graphite electrode using a stainless-steel cell in a two-electrode configuration (Figure 2-8). The electrode was composed of natural graphite powder (SNO-10, SEC Carbon Ltd., mean diameter of 10 μm), acetylene black (AB, Wako Pure Chemical Industries) as conducting materials, carboxymethyl cellulose (CMC) and styrene butadiene rubber (SBR) as binders in a weight ratio of graphite : AB: CMC: SBR = 80 : 10 : 5 : 5 on an Al current collector. Glass fiber (Nippon Sheet Glass, TGP010, thickness of 100 μm) impregnated in the electrolytes was used as a separator, and K metal disk was used for a counter electrode. The electrode was charged at a constant current (CC) of 1 C under the voltage range of 2.5-0.05 V and constant voltage (CV) at 0.05 V under the cutoff of 0.05 C, and was discharged at a constant current of 1 C under the cutoff voltage of 2.5 V.

7.3 Results and discussion

Thermal behavior of the ternary mixtures of K[FSA], K[FTA], and K[TfO] was investigated by DSC at a scan rate of 10 °C min^{-1} in order to determine a composition with the lowest melting point (the ratio of A : B : C represents a molar ratio of K[FSA], K[FTA], and K[TfO] in the following discussion). The compositions were explored among the composition area around the straight line shown in Figure 7-1 where the molar ratio of K[FSA]:K[FTA] is 55:45. Figure 7-2 shows DSC curves of the ternary mixture of K[FSA], K[FTA], and K[TfO]. The onset temperature of the exothermic peak is successfully decreased to 50 °C for almost all compositions with or over 33 mol% of K[TfO]. Too much K[TfO] (such as 40:20:40 and 30:20:50) does not change the onset temperature further and brings the shoulder peak at the higher temperature side owing to some unmelt compounds at the lower temperature side. By comparison of the intensities of the shoulder peaks, the molar ratio of 33:33:33 is determined to be used for further physicochemical and electrochemical investigations. The molar concentration of K^+ for the $K[FSA]_{0.33}[FTA]_{0.33}[TfO]_{0.33}$ SCIL is 9.3 mol dm^{-3} at 55 °C and 9.2 mol dm^{-3} at 90 °C as shown in Table 7-1, which are further larger than that for $K[FSA]_{0.55}[FTA]_{0.45}$ (8.5 mol dm^{-3} at 90 °C).

Temperature dependence of viscosity (η) of the $K[FSA]_{0.33}[FTA]_{0.33}[TfO]_{0.33}$ SCIL is shown in Figure 7-3 together with those of $K[FSA]_{0.55}[FTA]_{0.45}$, K[FSA], and K[FTA]. Viscosity of K[TfO] was not measured owing to its high melting point of 238 °C, which is over the limitation of the viscometer. The viscosity follows the VTF (Vogel−Tammann−Fulcher) equation shown in Eq. 6-1 with the fitting parameters given in Table 7-2. The $K[FSA]_{0.33}[FTA]_{0.33}[TfO]_{0.33}$ SCIL is in the liquid state in the wider temperature range near room temperature than the others due to the reduced melting point by the addition of the third salt of K[TfO]. On the other hand, the viscosity of $K[FSA]_{0.33}[FTA]_{0.33}[TfO]_{0.33}$ SCIL is increased compared with that of $K[FSA]_{0.55}[FTA]_{0.45}$ SCIL by the addition of K[TfO] as well as the decreased quantity of K[FSA]. It can be said that the viscosity of K[TfO] is higher than that of K[FTA] from the results that the viscosity of the $K[FSA]_{0.33}[FTA]_{0.33}[TfO]_{0.33}$ SCIL is almost the same as that of K[FTA] in the range between 101 °C and 150 °C and that of K[FSA] is lower than that of K[FTA]. The low viscosities of K[FSA] and K[FTA] would arise from the flexible amide anions (FSA^- and FTA^-) with high degrees of conformational freedoms, including C_1 (cis) and C_2 (trans) conformations [13, 14].

Figure 7-4 shows temperature dependence of ionic conductivity (σ) of the $K[FSA]_{0.33}[FTA]_{0.33}[TfO]_{0.33}$ SCIL together with those of $K[FSA]_{0.55}[FTA]_{0.45}$, K[FSA], and K[FTA]. The ionic conductivity of the $K[FSA]_{0.33}[FTA]_{0.33}[TfO]_{0.33}$ SCIL is fitted by the VTF equation shown Eq. 6-2 with the fitting parameters given in Table 7-2. The $K[FSA]_{0.33}[FTA]_{0.33}[TfO]_{0.33}$ SCIL have the lower ionic conductivity than the $K[FSA]_{0.55}[FTA]_{0.45}$ SCIL due to the additions of K[TfO] as well as the decreased quantity of K[FSA]. However, it is higher than that of K[FTA] nevertheless of their almost the same viscosity. This result can be also discussed by using the Walden rule (or fractional Walden rule) shown in Eq. 6-3 [15-19]. Figure 7-5 shows the Walden plots of the $K[FSA]_{0.33}[FTA]_{0.33}[TfO]_{0.33}$ SCIL together with those of the $K[FSA]_{0.55}[FTA]_{0.45}$, K[FSA], and K[FTA] SCILs, where the values above the dotted ideal line mean the great dissociation property of K^+ for the electrolytes. The $K[FSA]_{0.33}[FTA]_{0.33}[TfO]_{0.33}$ SCIL is plotted above the dashed ideal line, indicating that it has comparatively high ionic conductivity against the viscosity and an enhanced dissociation property.

The ionic conductivity described above is generated by all the ions in the $K[FSA]_{0.33}[FTA]_{0.33}[TfO]_{0.33}$ SCIL, i.e., K^+, FSA^-, FTA^-, and TfO^-. For the use as an electrolyte for PIBs, the important parameter is the partial conductivity of K^+ as it is related to the rate capability. The current limited by the K^+ partial conductivity (limiting current I_L^C) in PIBs is defined by the parameters of the electrolyte and electrochemical cell based on the Eqs. 6-5 and 6-6 with the similar assumptions described in Chapter 6. Table 7-1 shows these parameters for the $K[FSA]_{0.33}[FTA]_{0.33}[TfO]_{0.33}$ SCIL and an organic electrolyte of 1 M $K[FSA]_{0.33}[FTA]_{0.33}[TfO]_{0.33}$ dissolved in PC in the coin cell (Figure 2-9). The $K[FSA]_{0.33}[FTA]_{0.33}[TfO]_{0.33}$ SCIL has 0.19 mA cm^{-2} of I_L^C at 55 °C, which is significantly lower than 98.9 mA cm^{-2} of I_L^C at 55 °C for the organic electrolyte owing to its high viscosity. Figure 7-6 shows the time-voltage profile of the K||Al cell during galvanostatic K metal deposition on the Al substrate at various constant currents at 55 ºC in the two electrolytes. As shown in Figure 7-6 (a), the cell voltage for the $K[FSA]_{0.33}[FTA]_{0.33}[TfO]_{0.33}$ SCIL reaches steady values in spite of the current density of 10 mA cm^{-2} which is much higher than I_L^C although overpotential is large due to its high viscosity. However as shown in Figure 7-6 (b), the cell voltage for the organic electrolyte is stable at 10 and 50 mA cm^{-2}, but drops rapidly at 80 and 100 mA cm^{-2} which are near or over the calculated I_L^C. This is caused by deficiency of K^+ on the electrode surface and the decomposition of PC. These results indicate that there is no concentration gradient of K^+ in the $K[FSA]_{0.33}[FTA]_{0.33}[TfO]_{0.33}$ SCIL system, and the concentration of K^+ is maintained evenly throughout the electrolyte.

The lowered melting point allows the ternary system to keep K metal in the solid state unlike the case in Chapter 6. Therefore dissolution-deposition behaviors of K metal on Al substrate in the two electrolytes are also investigated here (see the section 7.2 for the detailed conditions of the dissolution-deposition tests). The dissolution-deposition efficiency (ε) of K metal is defined as shown below:

$$\varepsilon = 100 \times \{(N \times Q_{cycle}) / (Q_{ex} + N \times Q_{cycle})\} \tag{7-1}$$

where N is the cycle number before reaching the upper voltage limit of 1.0 V, Q_{cycle} is the quantity of charge during the cycle test, and Q_{ex} is the quantity of initial charge consumed for deposition of K metal before the cycle test. As shown in Figure 7-7 (a), the cycle test for the K[FSA]$_{0.33}$[FTA]$_{0.33}$[TfO]$_{0.33}$ SCIL finished at 17th cycle, which corresponds to ε = 81.3 %. However, as shown in Figure 7-7 (b), that for the organic electrolyte finishes only at 6th cycle, which corresponds to ε = 61.7 %. These results show that the K[FSA]$_{0.33}$[FTA]$_{0.33}$[TfO]$_{0.33}$ SCIL provides the better dissolution-deposition behavior of K metal than that in the organic electrolyte. One of the reasons for this difference is the stability of electrolytes against decomposition. Dissolution duration after the initial 1000-second charge for K deposition and electrolyte decomposition is 580 s for the K[FSA]$_{0.33}$[FTA]$_{0.33}$[TfO]$_{0.33}$ SCIL and 522 s for the organic electrolyte. This indicates more electrolytes are decomposed for the organic electrolyte than that for the K[FSA]$_{0.33}$[FTA]$_{0.33}$[TfO]$_{0.33}$ SCIL, and organic electrolyte is less stable against reduction. Therefore, such an electrolyte decomposition could also occur during the dissolution-deposition tests, and it could be more significant for the organic electrolyte. In addition, suppression of dendrite formation, which is reported for Li metal deposition in an ionic liquid electrolyte, could also be a possible reason [20].

Figure 7-8 shows the electrochemical window of the K[FSA]$_{0.33}$[FTA]$_{0.33}$[TfO]$_{0.33}$ SCIL at 10 mV s^{-1} at 55 °C investigated by cyclic voltammetry in the two-electrode cell with an Al or a Pt working electrode. The cathode limit is −0.1 V vs. K$^+$/K, which corresponds to the reversible dissolution and deposition of K metal. The coulombic efficiency is determined to be 55 %, which could be attributed to the decomposition of the anions or the elimination of the deposited K metal from the working electrode. The anode limit, which is determined at the current density of 0.4 mA·cm^{-2}, is 6.2 V vs. K$^+$/K corresponding to the oxidative decomposition of the anions. The electrochemical window for the ternary K[FSA]$_{0.33}$[FTA]$_{0.33}$[TfO]$_{0.33}$ SCIL is wider than that for the binary K[FSA]$_{0.55}$[FTA]$_{0.45}$ SCIL by the lowered temperature.

Figure 7-9 shows the cyclic voltammogram of the graphite electrode in the K[FSA]$_{0.33}$[FTA]$_{0.33}$[TfO]$_{0.33}$ SCIL at a scan rate of 0.2 mV s^{-1} at 55 °C. There is a cathodic peak around 1.4 V during the first cathodic scan, which corresponds to decomposition of the electrolyte. Intercalation of K$^+$ into graphite occurs below 0.4 V as shown by the next cathodic peak. During the first anodic scan, there are several anodic peaks corresponding to K$^+$ deintercalation from the GIC. The overall coulombic efficiency in the CV for 1st scan is 58.4 %.

Figure 7-10 shows the charge-discharge curves and the resulting capacity of the graphite electrode in the K[FSA]$_{0.33}$[FTA]$_{0.33}$[TfO]$_{0.33}$ SCIL at 55 °C (see section 7.2 for detailed charge-discharge condition). The first charge capacity was 361 mAh g^{-1}, which exceeds the theoretical capacity of 279 mAh g^{-1} based on the formation of KC_8 due to the decomposition of anions to form a solid electrolyte interphase (SEI) film. This irreversible capacity (361-279 = 82 mAh g^{-1}) is much lower than that for K[FSA]$_{0.55}$[FTA]$_{0.45}$ SCIL described in Chapter 6 (640-279 = 361 mAh g^{-1}) due to the lower operation temperature. The charge capacity significantly decreases to be 305 mAh g^{-1} at the second cycle, and reached 282 mAh g^{-1} at the 40th cycle after gradual decrease from around 20th cycle. On the other hand, the first discharge capacity is 284 mAh g^{-1}, which slightly exceeds the theoretical capacity due to the additional capacity from acetylene black. The discharge capacity reached 271 mAh g^{-1} at the 40th cycle after gradual decrease from around 20th cycle. The average coulombic efficiency of 95.8 % from the 2nd to 40th cycles for the electrode cycled in the ternary K[FSA]$_{0.33}$[FTA]$_{0.33}$[TfO]$_{0.33}$ SCIL is better than that of 89.5 % for the cycle in the binary

$K[FSA]_{0.55}[FTA]_{0.45}$ SCIL described in Chapter 6.

Figure 7-11 shows the *ex-situ* XRD patterns of the graphite electrodes before and after the first charge and discharge. The low peak intensity is due to the electrolyte left on the electrode which is not rinsed to avoid possible reaction of the solvent with the electrode [21, 22]. After charge, the peak at 26.54° corresponding to the 002 diffraction of the pristine graphite disappears, and new peaks at 16.60° and 33.53° appear, corresponding to $d = 5.34$ and 2.67 Å, respectively. These peaks are indexed as 001 and 002 of a GIC, which leads to the interlayer distance of 5.34 Å, suggesting the formation of stage-1 potassium-graphite intercalation compounds (K-GICs). The peaks might be indexed as 004 and 008, respectively, by taking a superlattice formed by alternating in-plane arrangements of K^+ in the graphite gallery as discussed in previous works [23, 24]. The color of the sample is brown, indicative of the formation of stage-1 K-GIC ($\approx KC_8$) [25, 26]. Sufficient intercalation of K^+ is suggested by the absence of any other peaks attributed to stage-2 K-GIC (around 20.5° and 30.1°) [25, 27]. After discharge, these peaks disappear and the 002 diffraction peak of graphite recovers at 26.54°, indicating the intercalation/deintercalation of K^+ into/from graphite proceeds reversibly in this ternary system.

7.4 Conclusions

In this chapter, the ternary system of K-SCIL composed of K[FSA], K[FTA], and K[TfO] was investigated for PIBs. The melting point of the mixture of K[FSA], K[FTA], and K[TfO] had a melting point of 50 ºC at the composition of $K[FSA]_{0.33}[FTA]_{0.33}[TfO]_{0.33}$, which is lower than that of 67 °C for the $K[FSA]_{0.55}[FTA]_{0.45}$ binary K-SCIL by the addition of the third salt of K[TfO]. Although the ionic conductivities of the ternary K-SCIL were slightly lower than those of the binary K-SCIL, a K^+ transport was realized exceeding the calculated limiting current due to the absence of a concentration gradient for K^+. The dissolution-deposition tests of solid K metal at 55 °C, which was enabled by the decreased melting point below that of K metal (63.5 °C), showed that the ternary K-SCIL had the coulombic efficiency of 81.3 % higher than that for the organic electrolyte of 1 M $K[FSA]_{0.33}[FTA]_{0.33}[TfO]_{0.33}$ dissolved in PC (61.7 %). The ternary K-SCIL possesses a wide electrochemical window over 5 V at 55 °C, enabling the use of a high voltage positive electrode material. Cyclic voltammetry of a graphite electrode suggested that intercalation of K^+ into graphite occurs around 0.4 V vs. K^+/K as well as intercalation/deintercalation process of K^+ into/from graphite could be different. The graphite negative electrode effectively worked during the 40-cycle of charge-discharge in the ternary K-SCIL at 55 °C, providing a discharge capacity around the theoretical value based on the formation of stage-1 K-GIC. The reversible intercalation/deintercalation of K^+ into/from graphite were confirmed by *ex-situ* XRD measurements. Interesting characteristics and potentials as a PIB electrolyte of the ternary K-SCIL are demonstrated in this study.

Table 7-1 Concentration of shuttle ions, viscosity, and calculated diffusion coefficient and limiting current density for 1 M K$[FSA]_{0.33}[FTA]_{0.33}[TfO]_{0.33}$ in PC and K$[FSA]_{0.33}[FTA]_{0.33}[TfO]_{0.33}$ SCIL at 55 ºC.

Electrolyte	C [mol dm^{-3}]	η [mPa s]	$D^{\mathrm{C}\,a}$ [10^{-10} m^2 s^{-1}]	$I_{\mathrm{L}}^{\mathrm{C}\,a}$ [mA cm^{-2}]
1 M K$[FSA]_{0.33}[FTA]_{0.33}[TfO]_{0.33}$ in PC	1.0	2.99	7.3	98.9
K$[FSA]_{0.33}[FTA]_{0.33}[TfO]_{0.33}$ SCIL	9.3	14600	1.5×10^{-3}	0.19

$^{a}D^{\mathrm{C}}$ and $I_{\mathrm{L}}^{\mathrm{C}}$ are calculated by Eqs. (6-5) and (6-6) assuming A = 0.785 cm^2 and d = 0.285 mm.

Table 7-2 Parameters of VTF fitting for viscosity and ionic conductivity of $K[FSA]_{0.33}[FTA]_{0.33}[TfO]_{0.33}$.

Viscosity			Ionic conductivity		
A_η [mPa s $K^{-0.5}$]	B_η [K]	$T_{0\eta}$ [K]	A_σ [mS cm^{-1} $K^{0.5}$]	B_σ [K]	$T_{0\sigma}$ [K]
4.63×10^{-3}	1.22×10^{3}	2.27×10^{2}	7.34×10^{4}	9.09×10^{2}	2.39×10^{2}
Coefficient of determination: $R^2 = 0.999994$			Coefficient of determination: $R^2 = 0.99997$		

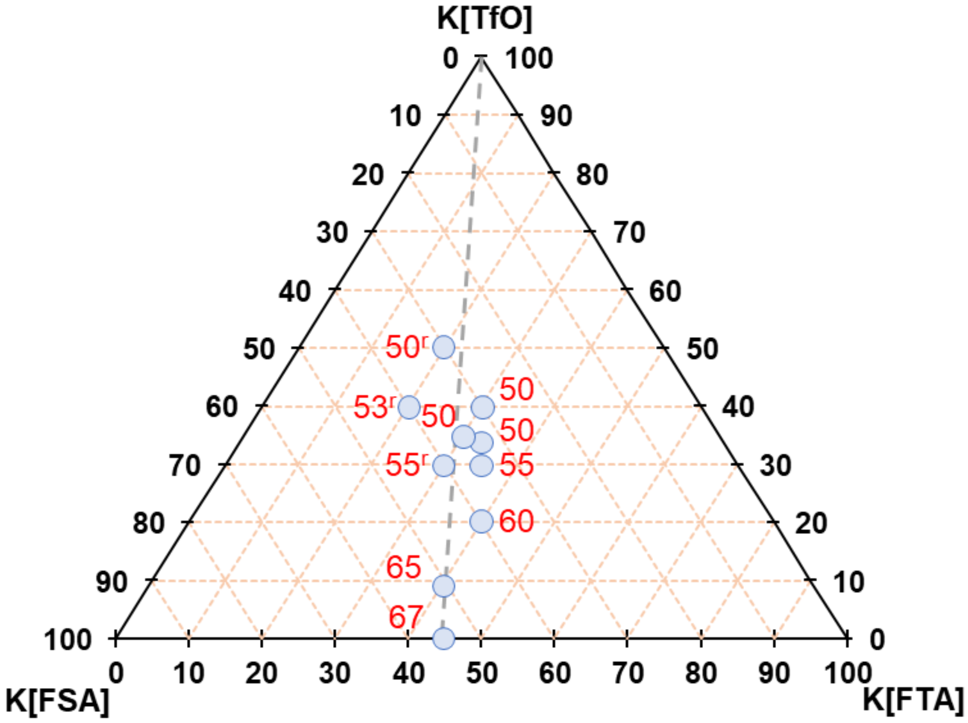

Figure 7-1 Ternary phase diagram of K[FSA], K[FTA], and K[TfO]. The numbers are melting points at the specific points. The letter of *r* on the right upper part of the numbers indicates that there is a shoulder along the main peak at the higher temperature side in DSC corresponding to some residual salts.

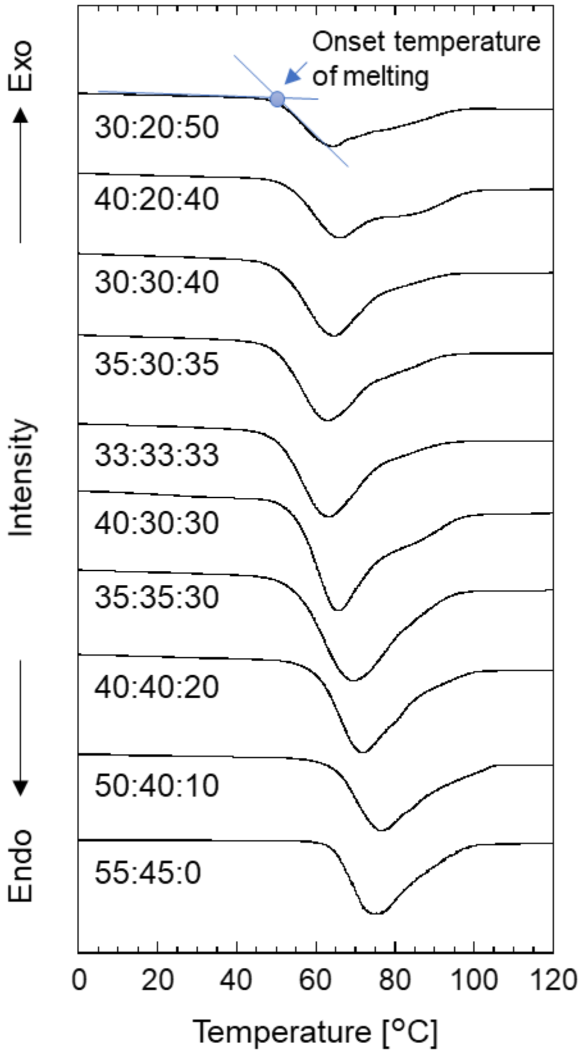

Figure 7-2 DSC curves for the mixtures of K[FSA], K[FTA], and K[TfO] by continuous heating at the rate of 10 °C·min^{-1} to determine solidus temperature.

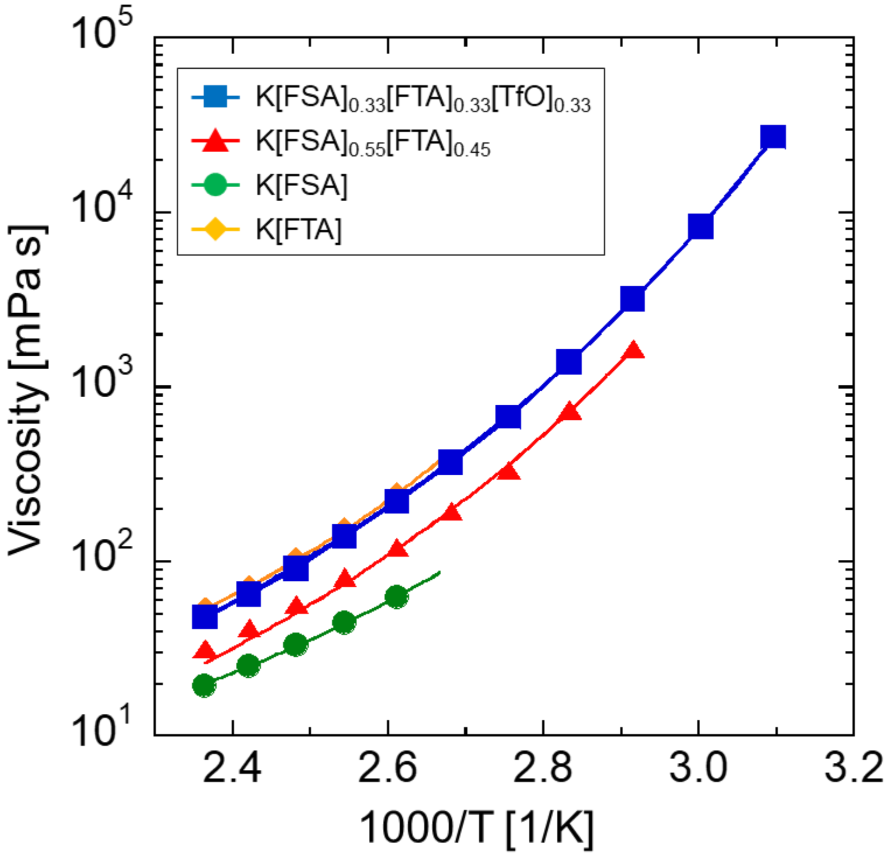

Figure 7-3 Temperature dependence of viscosity for the K[FSA]$_{0.33}$[FTA]$_{0.33}$[TfO]$_{0.33}$, K[FSA]$_{0.55}$[FTA]$_{0.45}$, K[FSA], and K[FTA] SCILs.

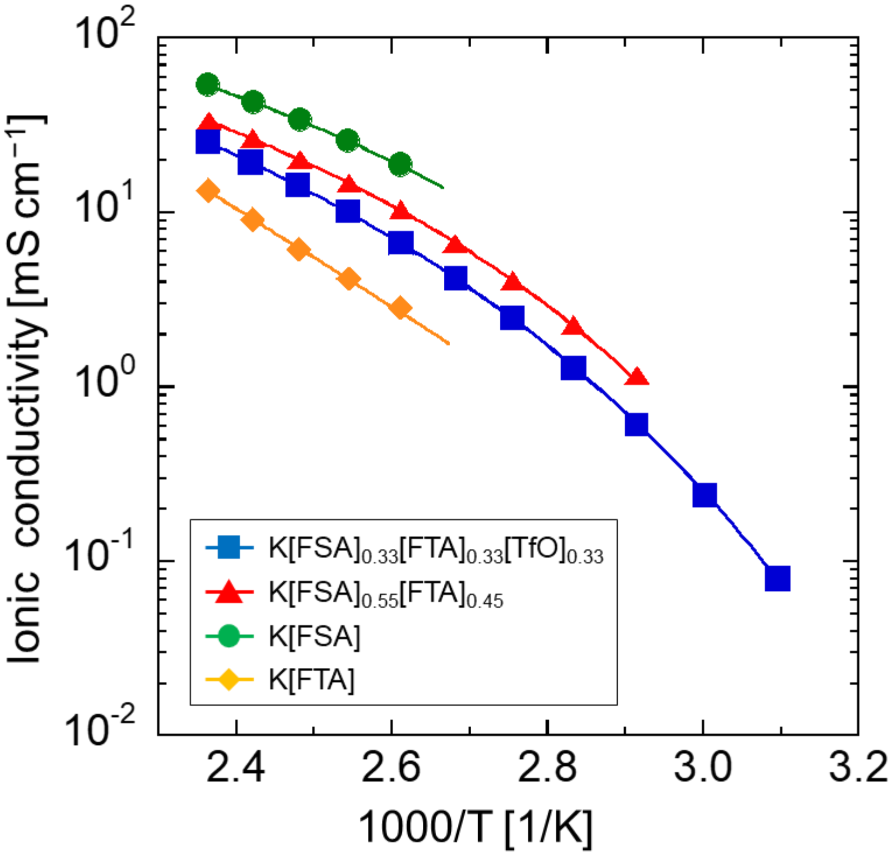

Figure 7-4 Temperature dependence of ionic conductivity for the K[FSA]$_{0.33}$[FTA]$_{0.33}$[TfO]$_{0.33}$, K[FSA]$_{0.55}$[FTA]$_{0.45}$, K[FSA], and K[FTA] SCILs.

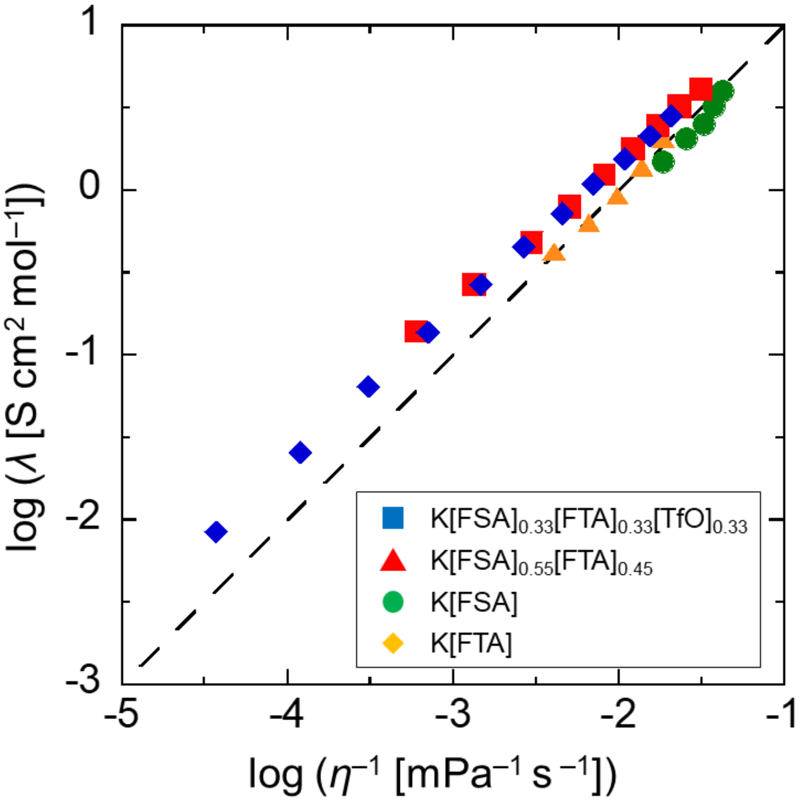

Figure 7-5 Walden plot of the K[FSA]$_{0.33}$[FTA]$_{0.33}$[TfO]$_{0.33}$, K[FSA]$_{0.55}$[FTA]$_{0.45}$, K[FSA], and K[FTA] SCILs.

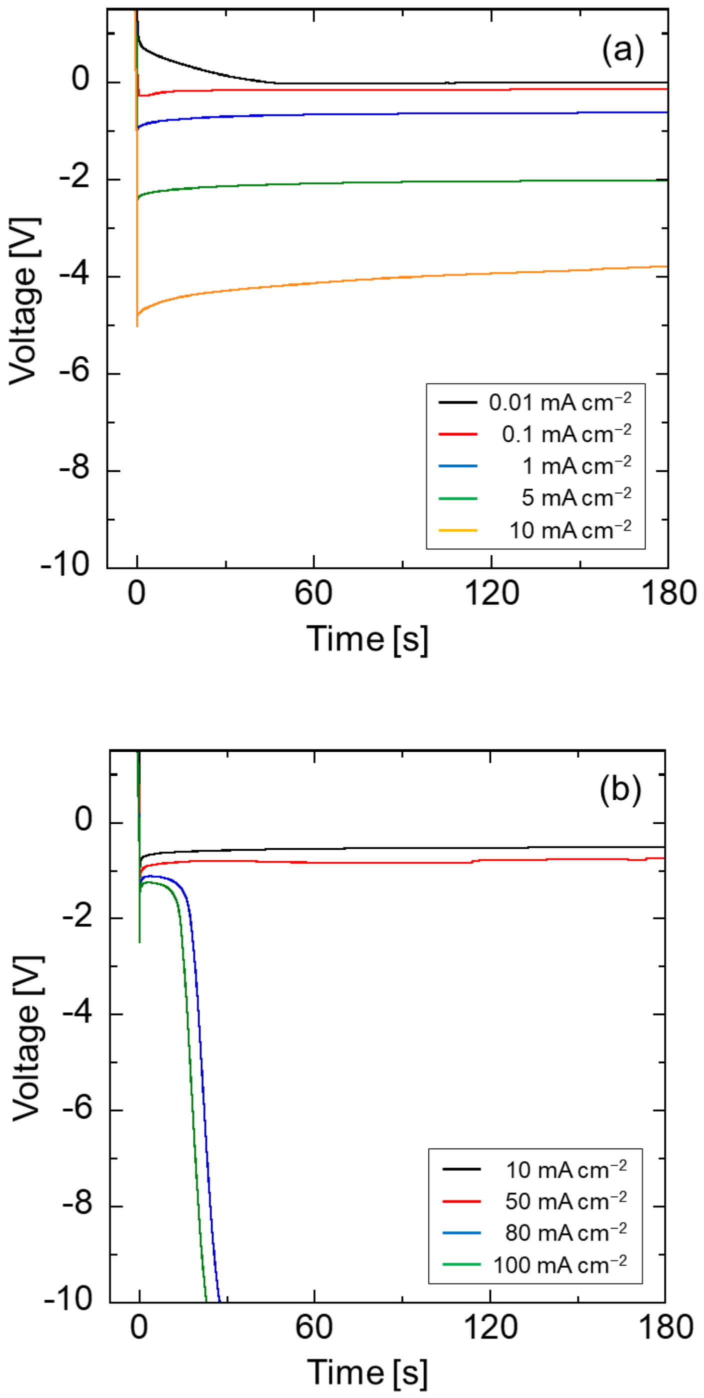

Figure 7-6 Time-voltage profile of the K||Al cell during galvanostatic K metal deposition at a various constant currents at 55 ºC for (a) $K[FSA]_{0.33}[FTA]_{0.33}[TfO]_{0.33}$ SCIL and (b) 1 M $K[FSA]_{0.33}[FTA]_{0.33}[TfO]_{0.33}$ in PC.

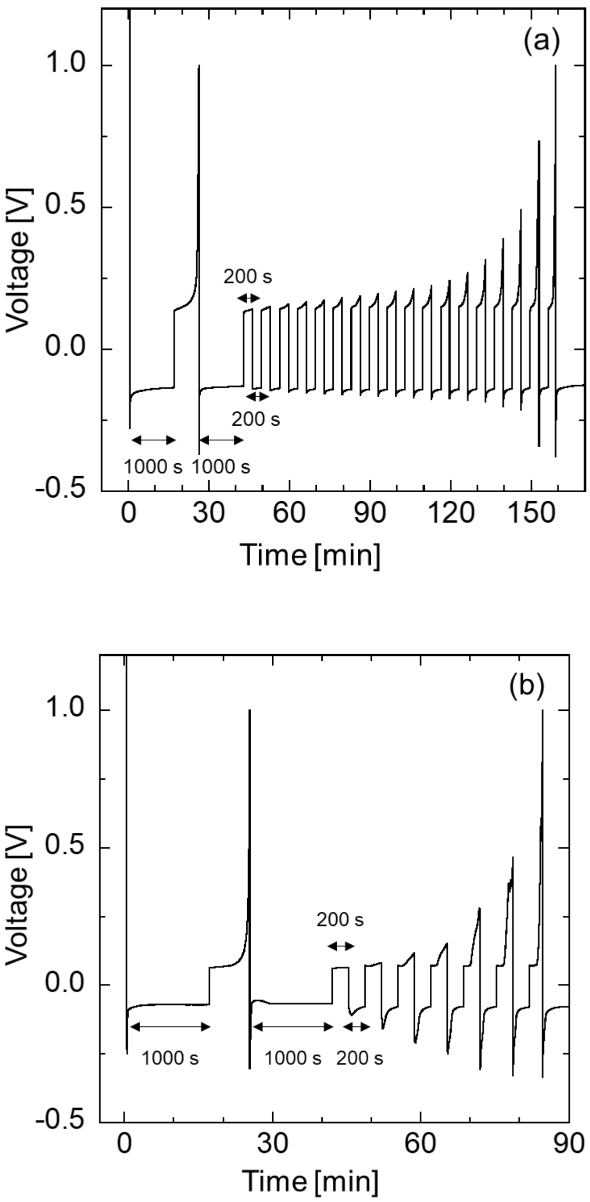

Figure 7-7 Voltage profile during the K metal dissolution-deposition tests on an Al foil at 0.1 mA cm^{-2} at 55 °C in (a) K[FSA]$_{0.33}$[FTA]$_{0.33}$[TfO]$_{0.33}$ SCIL and (b) 1 M K[FSA]$_{0.33}$[FTA]$_{0.33}$[TfO]$_{0.33}$ in PC (see section 7.2 for the detailed condition).

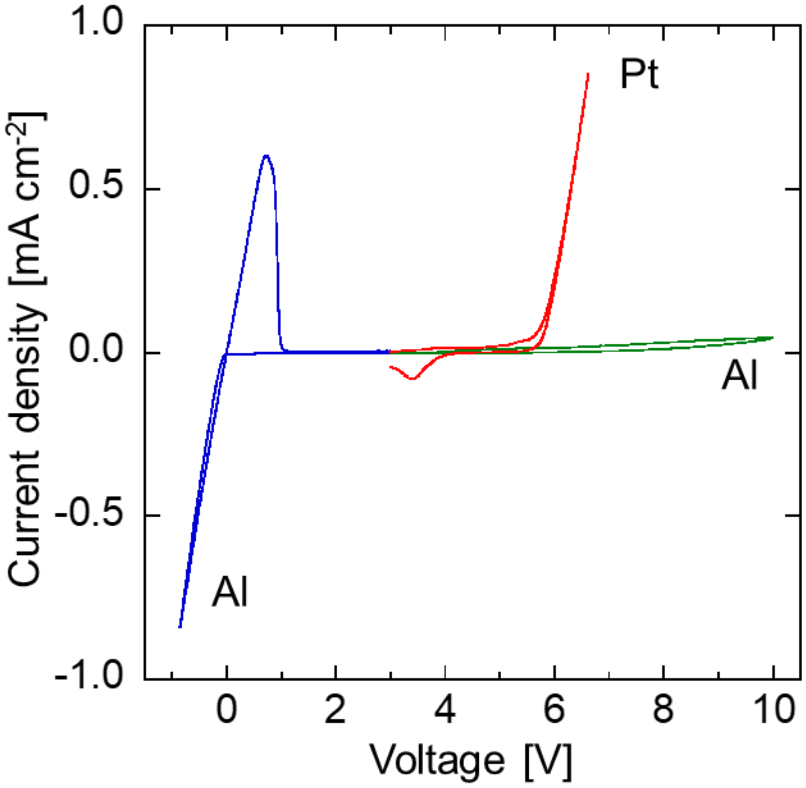

Figure 7-8 Combined cyclic voltammogram of Al and Pt electrodes in the K[FSA]$_{0.33}$[FTA]$_{0.33}$[TfO]$_{0.33}$ SCIL at a scan rate of 10 mV s^{-1} and 55 ºC.

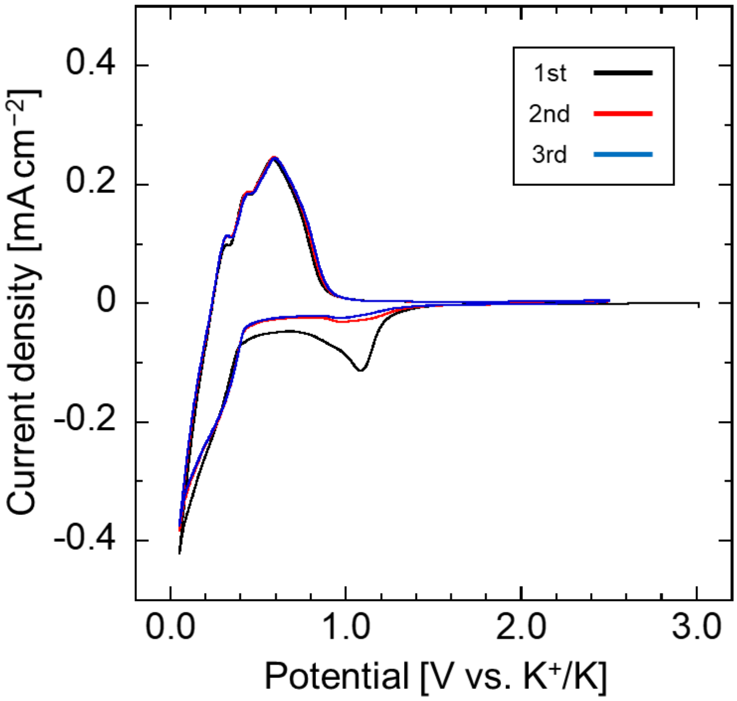

Figure 7-9 Cyclic voltammogram of a graphite electrode in the K[FSA]$_{0.33}$[FTA]$_{0.33}$[TfO]$_{0.33}$ SCIL at the scan rate of 0.2 mV s^{-1} at 55 °C in the 1st, 2nd, and 3rd scans (coulombic efficiencies for 1st, 2nd, and 3rd scans are 58.4, 78.9, and 83.3 %, respectively).

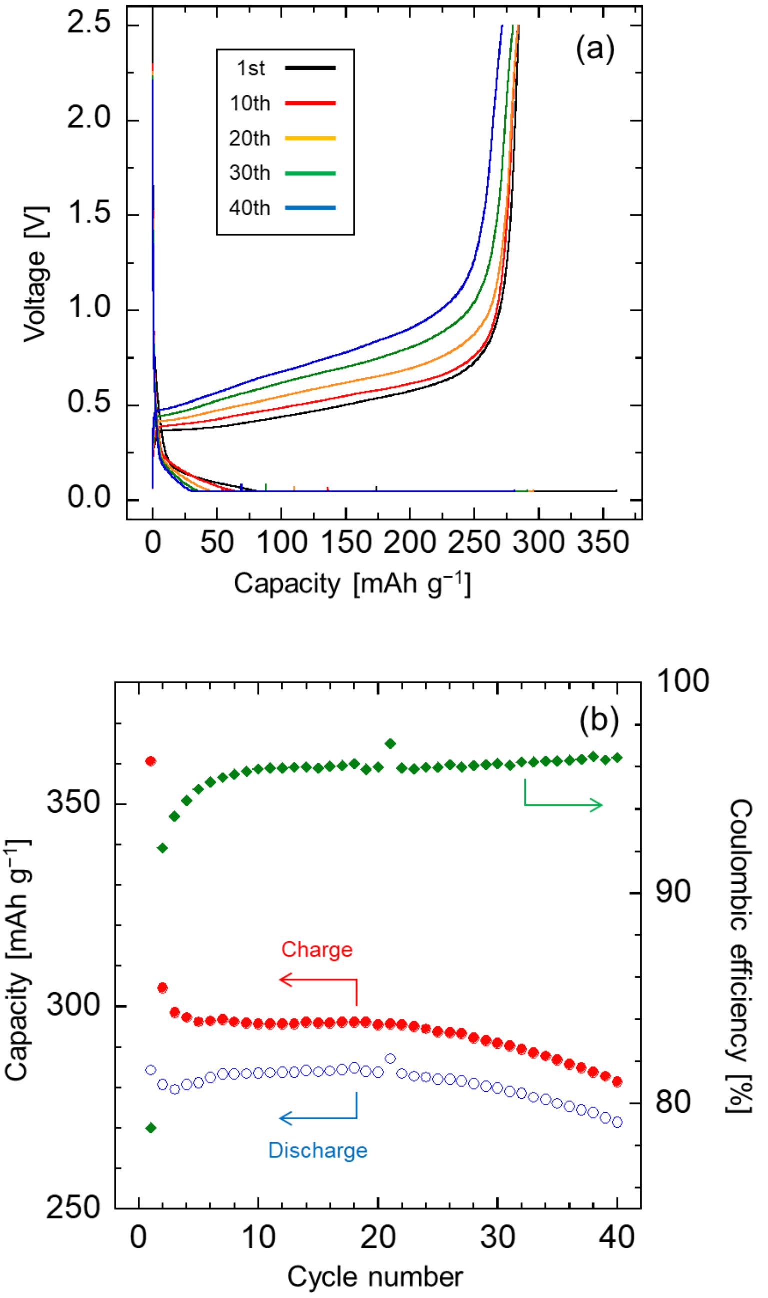

Figure 7-10 (a) Charge-discharge curves and (b) charge-discharge capacities and coulombic efficiency at each cycle of the K||graphite cell in the K[FSA]$_{0.33}$[FTA]$_{0.33}$[TfO]$_{0.33}$ SCIL at a charge/discharge rate of 1 C at 55 ºC.

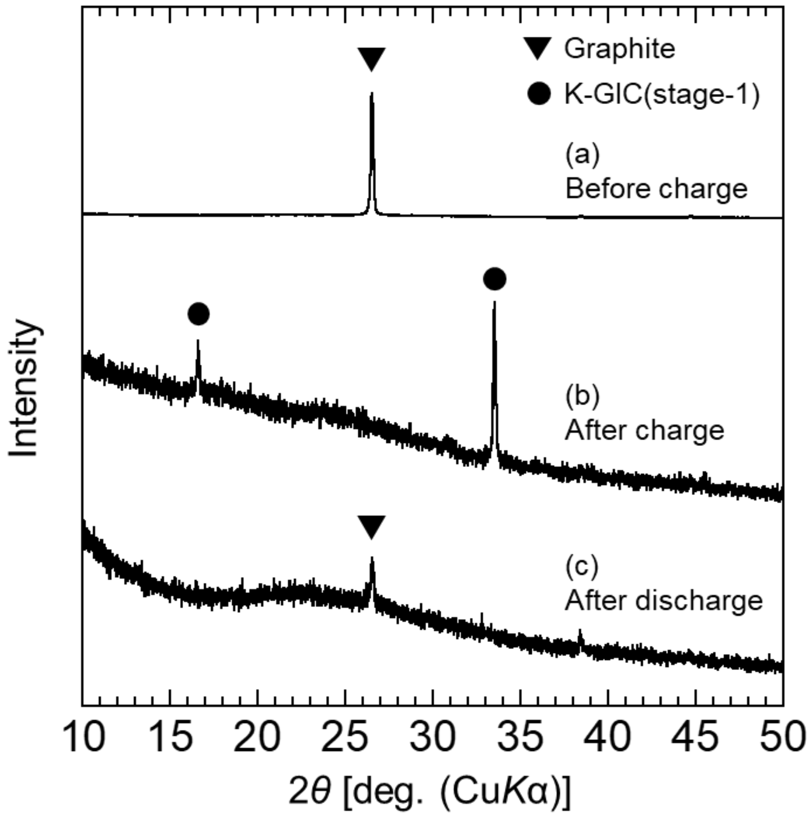

Figure 7-11 XRD patterns of the graphite electrodes. (a) Before charge, (b) after charge, and (c) after discharge in the K[FSA]$_{0.33}$[FTA]$_{0.33}$[TfO]$_{0.33}$ SCIL. Charge condition: constant current/constant voltage mode (1 C (cutoff: 0.05 V) / 0.05 V (cutoff: 0.05 C)). Discharge condition: constant current of 1 C (cutoff: 2.5 V).

References

[1] K. Matsumoto, Y. Okamoto, T. Nohira, R. Hagiwara, *J. Phys. Chem. C*, **119** (2015) 7648.

[2] M. Galiński, A. Lewandowski, I. Stępniak, *Electrochim. Acta*, **51** (2006) 5567.

[3] I. Osada, H. de Vries, B. Scrosati, S. Passerini, *Angew. Chem. Int. Ed.*, **55** (2016) 500.

[4] A. Fernicola, F. Croce, B. Scrosati, T. Watanabe, H. Ohno, *J. Power Sources*, **174** (2007) 342.

[5] D. Monti, E. Jónsson, M. R. Palacín, P. Johansson, *J. Power Sources*, **245** (2014) 630.

[6] D. R. MacFarlane, N. Tachikawa, M. Forsyth, J. M. Pringle, P. C. Howlett, G. D. Elliott, J. H. Davis, M. Watanabe, P. Simon, C. A. Angell, *Energy Environ. Sci.*, **7** (2014) 232.

[7] M. Fiore, S. Wheeler, K. Hurlbutt, I. Capone, J. Fawdon, R. Ruffo, M. Pasta, *Chem. Mater.*, **32** (2020) 7653.

[8] R. M. de Souza, L. J. A. de Siqueira, M. Karttunen, L. G. Dias, *J. Chem. Inf. Model.*, **60** (2020) 485.

[9] H. Onuma, K. Kubota, S. Muratsubaki, T. Hosaka, R. Tatara, T. Yamamoto, K. Matsumoto, T. Nohira, R. Hagiwara, H. Oji, S. Yasuno, S. Komaba, *ACS Energy Lett.*, **5** (2020) 2849.

[10] M. Arnaiz, A. Bothe, S. Dsoke, A. Balducci, J. Ajuria, *J. Electrochem. Soc.*, **166** (2019) A3504.

[11] T. Yamamoto, T. Nohira, *Chem. Commun.*, **56** (2020) 2538.

[12] K. Kubota, T. Nohira, R. Hagiwara, *Electrochim. Acta*, **66** (2012) 320.

[13] K. Fujii, T. Fujimori, T. Takamuku, R. Kanzaki, Y. Umebayashi, S.-i. Ishiguro, *J. Phys. Chem. B*, **110** (2006) 8179.

[14] K. Fujii, S. Seki, S. Fukuda, R. Kanzaki, T. Takamuku, Y. Umebayashi, S.-i. Ishiguro, *J. Phys. Chem. B*, **111** (2007) 12829.

[15] W. Xu, E. I. Cooper, C. A. Angell, *J. Phys. Chem. B*, **107** (2003) 6170.

[16] D. R. MacFarlane, M. Forsyth, E. I. Izgorodina, A. P. Abbott, G. Annat, K. Fraser, *Phys. Chem. Chem. Phys.*, **11** (2009) 4962.

[17] M. Yoshizawa, W. Xu, C. A. Angell, *J. Am. Chem. Soc.*, **125** (2003) 15411.

[18] K. R. Harris, *J. Phys. Chem. B*, **114** (2010) 9572.

[19] J.-W. Park, K. Yoshida, N. Tachikawa, K. Dokko, M. Watanabe, *J. Power Sources*, **196** (2011) 2264.

[20] J. Hwang, H. Okada, R. Haraguchi, S. Tawa, K. Matsumoto, R. Hagiwara, *J. Power Sources*, **453** (2020) 227911.

[21] G. A. Elia, I. Hasa, G. Greco, T. Diemant, K. Marquardt, K. Hoeppner, R. J. Behm, A. Hoell, S. Passerini, R. Hahn, *J. Mater. Chem. A*, **5** (2017) 9682.

[22] J. Jegoudez, C. Mazieres, R. Setton, *Synth. Met.*, **7** (1983) 85.

[23] Z. Wang, S. M. Selbach, T. Grande, *RSC Adv.*, **4** (2014) 4069.

[24] W. Rüdorff, E. Schulze, *Z. Anorg. Allg. Chem.*, **277** (1954) 156.

[25] S. Komaba, T. Hasegawa, M. Dahbi, K. Kubota, *Electrochem. Commun.*, **60** (2015) 172.

[26] J. Zhao, X. Zou, Y. Zhu, Y. Xu, C. Wang, *Adv. Funct. Mater.*, **26** (2016) 8103.

[27] W. Luo, J. Wan, B. Ozdemir, W. Bao, Y. Chen, J. Dai, H. Lin, Y. Xu, F. Gu, V. Barone, L. Hu, *Nano Lett.*, **15** (2015) 7671.

Chapter 8

General Conclusions

Fluorine provides a variety of attractive functionalities to materials owing to its distinct properties such as small atomic size, low polarizability, and the highest electronegativity. Fluorine is extensively utilized for materials in various fields including organic, polymer, and inorganic chemistries, playing industrially and scientifically important roles. Out of a variety of fluorine-containing materials, fluorine-containing carbon materials and ionic liquids have been widely studied, providing unique synthetic, structural, and electrochemical applications. In this study, new materials, fluorinating methods, and electrochemical applications involving fluorine-containing carbon materials are investigated in Chapters 3, 4, and 5. Developments and applications of new ionic liquid electrolytes consisting of fluorine-containing anions are explored for high-performance and safe potassium-ion batteries in Chapters 6 and 7. The summary of each chapter is described below.

In Chapter 3, novel GICs with hexafluorosilicate (SiF_6^{2-}) were synthesized targeting the intercalation of doubly charged ions, and the stage-number dependence of chemical states of intercalated species (SiF_6^{2-} or SiF_5^-) was discussed. Fluorosilicate GICs (SiF_y-GICs) with four different stage numbers (from stage-5 to -2, where different stage numbers were mixed) were synthesized, and larger gallery height in SiF_y-GICs at lower stage numbers than those at higher stage numbers suggested the intercalation of different chemical species depending on the stage numbers. Their reactions with PF_5 brought decreases of stage numbers and large weight increases which could not be explained by simple substitution of SiF_4 with PF_5 to intercalate PF_6^-. A model that SiF_6^{2-} is at stage-n ($n \geq 3$) and SiF_5^- is at stage-2 explained the gravimetrical and structural results well. Intercalation of SiF_6^{2-} into graphite and dependence of intercalated species on the stage numbers were identified for the first time.

In Chapter 4, graphite oxide (GO) was deoxofluorinated with sulfur tetrafluoride (SF_4) to explore a new synthetic method of fluorinated carbon materials. Their reactions in different conditions clarified that their reactions proceeded only at high pressures of SF_4 (≥ 8 atm at 25 °C), but HF catalyzed the reactions to proceed at 1 atm of SF_4 at 25 °C. The highest degree of fluorination was obtained in the reaction conditions at 5 atm of SF_4 at 150 °C for 24 h in the presence of HF catalyst. In the reactions, hydroxy and carbonyl groups were deoxofluoriated almost fully and partially, respectively, but epoxy groups did not react. In addition to the deoxofluorination, intercalation of SF_4 and SOF_2 occurred as a side reaction, which were removed by water-washing. Decrease in hydrophilicity was observed, which was due to elimination of oxygen-containing functional groups and introduction of fluorine. Moreover, interlayer distance increased after deoxofluorination in spite of the smaller size of fluorine than that of oxygen-containing functional groups, which could be explained by disappearance of hydrogen bonds present in GO.

In Chapter 5, activated carbon electrode was deoxofluorinated with SF_4 to improve electrochemical performance for electric double layer capacitors (EDLCs), especially targeting improvement of oxidation stability at high potentials. It was clarified that more fluorine atoms were introduced on the surface than the bulk due to the presence of oxygen-containing functional groups on the surface, which suggested that the deoxofluorination proceeded only on the oxygen-containing functional groups without destructing carbon skeleton. It was also confirmed that the higher pressure of SF_4 led to the higher degree of fluorination. Introduction of more fluorine atoms resulted in higher capacitance and coulombic efficiency as an electrode for EDLCs, especially when charging up to high potentials. The performance deterioration was not observed because weak oxidation power of SF_4 did not introduce too much fluorine unlike other fluorinating agents with higher oxidation power such as F_2.

In Chapter 6, the binary system of potassium single cation ionic liquid (K-SCIL) electrolytes were developed by mixing K[FSA] and K[FTA] ($FSA^–$: bis(fluorosulfonyl)amide and $FTA^–$: (fluorosulfonyl)(trifluoromethylsulfonyl)amide). Thermal analyses of the binary salts with different ratios clarified that they had a eutectic composition at 55:45 for K[FSA]:K[FTA] with a melting point of 67 °C. The $K[FSA]_{0.55}[FTA]_{0.45}$ SCIL reached a high K^+ concentration of 8.5 mol $dm^{–3}$ at 90 °C, whereas the viscosity and ionic conductivity of the $K[FSA]_{0.55}[FTA]_{0.45}$ SCIL were higher and lower, respectively, than those of $K_{0.2}[C_3C_1pyrr]_{0.8}[FSA]$ RTIL (RTIL: room temperature ionic liquid). However, applying current over the calculated limiting current density based on the diffusion control model on an Al electrode in the $K[FSA]_{0.55}[FTA]_{0.45}$ SCIL showed stable K metal deposition due to the absence of concentration gradient in contrast that in the RTIL where electrolyte decomposition occurred. The $K[FSA]_{0.55}[FTA]_{0.45}$ SCIL had a wide electrochemical window over 5 V at 90 °C, and reversible intercalation/deintercalation of K^+ into/from graphite at 80 °C was confirmed for PIBs.

In Chapter 7, the K-SCIL was further explored through the ternary K-SCIL system comprising of K[FSA], K[FTA], and K[TfO] to lower the melting point. Thermal analyses of the ternary salts with different compositions near the 55:45 molar ratio for K[FSA]:K[FTA] clarified that it had the lowest melting point at 50 °C in the molar ratio of 33:33:33 for K[FSA]:K[FTA]:K[TfO]. The melting point was lower than the melting point of K metal, 63.5 °C, which enabled K metal to be handled in the solid state. The $K[FSA]_{0.33}[FTA]_{0.33}[TfO]_{0.33}$ SCIL had extremely high concentration (9.3 mol $dm^{–3}$ at 55 °C and 9.2 mol $dm^{–3}$ at 90 °C) whereas the viscosity and ionic conductivity of the $K[FSA]_{0.33}[FTA]_{0.33}[TfO]_{0.33}$ SCIL were slightly higher and lower, respectively, than those of the $K[FSA]_{0.55}[FTA]_{0.45}$ SCIL. The dissolution and deposition tests of solid K metal in the $K[FSA]_{0.33}[FTA]_{0.33}[TfO]_{0.33}$ SCIL at 55 °C showed the 81.3 % efficiency, whereas that in an organic electrolyte (1 M $K[FSA]_{0.33}[FTA]_{0.33}[TfO]_{0.33}$ dissolved in PC (PC: propylene carbonate)) was 61.7 %. The stable deposition of K metal under a large current over the calculated limiting current density based on the diffusion control model at 55 °C was also confirmed for the ternary system of the $K[FSA]_{0.33}[FTA]_{0.33}[TfO]_{0.33}$ SCIL in contrast to that for the organic electrolyte. Cyclic voltammetry with a graphite electrode at 55 °C confirmed intercalation of K^+ into graphite below 0.4 V vs. K^+/K. The charge-discharge tests of a graphite negative electrode in the $K[FSA]_{0.33}[FTA]_{0.33}[TfO]_{0.33}$ SCIL at 55 °C provided a discharge capacity around the theoretical value based on the formation of stage-1 K-GIC, retaining over 90 % of the theoretical capacity after 40 cycles.

Both the fluorine-containing materials of carbon and ionic liquids in this study are of interest for researchers in various fields and subjects of material, structural, and computational chemistries. Further studies of these topics are expected to extend the realm of fluorine chemistry to the direction which has been untouched by researchers.

List of Publications

Chapter 3

Hiroki Yamamoto, Kazuhiko Matsumoto, Rika Hagiwara

Journal of Fluorine Chemistry, **242** (2021) 109714.

‘‘Stage-number dependence of intercalated species for fluorosilicate graphite intercalation compounds: pentafluorosilicate vs. hexafluorosilicate’’

Chapter 4

Hiroki Yamamoto, Kazuhiko Matsumoto, Yoshiaki Matsuo, Yuta Sato, Rika Hagiwara

Dalton Transactions, **49** (2019) 47-56.

‘‘Deoxofluorination of graphite oxide with sulfur tetrafluoride’’

Chapter 5

Hiroki Yamamoto, Kenji Iwamoto, Kazuhiko Matsumoto, Rika Hagiwara

Electrochemistry, in press (DOI: 10.5796/electrochemistry.20-65148).

‘‘Deoxofluorination of activated carbon electrode with sulfur tetrafluoride for electric double layer capacitor’’

Chapter 6

Hiroki Yamamoto, Chih-Yao Chen, Keigo Kubota, Kazuhiko Matsumoto, Rika Hagiwara

The Journal of Physical Chemistry B, **124** (2020) 6341-6347.

‘‘Potassium single cation ionic liquid electrolytes for potassium-ion batteries’’

Chapter 7

Hiroki Yamamoto, Keigo Kubota, Kazuhiko Matsumoto, Rika Hagiwara

Journal of the Electrochemical Society, to be submitted.

‘‘Electrochemical behaviors of solid-potassium-metal and graphite anodes in potassium single cation ionic liquid electrolytes for potassium secondary batteries near room temperature’’

Related works not described in this thesis

Yoshiaki Matsuo, Junichi Inamoto, Hiroki Yamamoto, Kazuhiko Matsumoto, Rika Hagiwara

Electrochemistry, **88** (2020) 437-440.

‘‘Discharge characteristic of fluorinated graphene-like graphite as a cathode of lithium primary battery’’

Jinkwang Hwang, Ashvini Nair Sivasengaran, Huan Yang, Hiroki Yamamoto, Takashi Takeuchi, Kazuhiko Matsumoto, Rika Hagiwara

ACS Applied Materials and Interfaces, in press (DOI: 10.1021/acsami.0c17807).

‘‘Improvement of electrochemical stability using the eutectic composition of a ternary molten salt system for highly concentrated electrolytes for Na-ion batteries’’,

Acknowledgements

I would like to express my deepest gratitude to Professor Rika Hagiwara to allow me to study under his supervision. His extensive and deep knowledge and constructive advices led my research to success. My heartfelt appreciations go to Associate Professor Kazuhiko Matsumoto for his comprehensive supports for me. Without his insightful comments, warm encouragements, and invaluable instructions, I would not complete this study as well as acquire a lot of knowledge, experiences, and skills. I am truly grateful to Associate Professor Kouji Yasuda for his educational instructions and kind assistances. I am sincerely thankful to Assistant Professor Jinkwang Hwang for his technical and moral supports and sincere encouragements. I wish to appreciate Dr. Keigo Kubota's helpful advices and constructive discussions. Special thanks are given to Professor Toshiyuki Nohira and Professor Hiroshi Sakaguchi for their fruitful discussions and suggestions. I would like to thank Assistant Professor Takayuki Yamamoto for his technical instructions and kind helps. I am sincerely thankful to Professor Yoshiaki Matsuo and Dr. Yuta Sato for helping me with sample preparations and characterizations. I would like to thank Dr. Chih-Yao Chen for providing me constructive advices and beneficial discussions.

I thank all the members in Energy Chemistry Laboratory. In particular, my sincere thanks go to Dr. Kaushik Shubham, Dr. Hung Yang, Ms. Yayun Zheng, and Mr. Di Wang. My special thanks are given to Ms. Naoko Sakamoto, Ms. Hisami Okuda, and Ms. Masayo Kawada for their kind and warm supports.

I must owe my deepest gratitude to my father Masahiro Yamamoto, my mother Mika Yamamoto, and my younger sister Saki Yamamoto for their comprehensive supports. It would be impossible to complete this study without their supports.

Not all acknowledgements are described here. I am sincerely thankful to all those who are related to this study.

Hiroki Yamamoto

February 2021